Electrochemical SPM Study of 2D and 3D Phase Formation of Zn at the Ionic Liquid / Au(111) Interface

Zur Erlangung des akademischen Grades eines
DOKTORS DER NATURWISSENSCHAFTEN
(Dr. rer. nat.)
der Fakultät für Chemie und Biowissenschaften der
Universität Karlsruhe (TH)
angenommene

DISSERTATION
von
M. Sc. Jana Dogel
aus Troizk, Russland

Dekan: Prof. Dr. M. Kappes
Referent: Prof. Dr. W. Freyland
Korreferent: Prof. Dr. M. Olzmann
Tag der mündlichen Prüfung: 03.05.2004

Contents

Abstract / Zusammenfassung 1

1. Introduction 5

2. Basic concepts of the experimental techniques 11

- **2.1 Scanning tunneling microscopy** 11
- **2.2 Scanning tunneling spectroscopy** 16
- **2.3 Electrochemical methods** 18
  - **2.3.1** Cyclic voltammetry 18
  - **2.3.2** Chronoamperometry 22

3. Experimental part 27

- **3.1 General problems and requirements** 27
- **3.2 Experimental setup** 31
  - **3.2.1** Electrochemical Variable Temperature Scanning Tunneling Microscope 31
  - **3.2.2** Preparation and initial assembling of the electrochemical cell 34
  - **3.2.3** Au substrate 37
  - **3.2.4** Molten salt 37
  - **3.2.5** Preparation of STM tips 40
- **3.3 Experimental procedure** 42
  - **3.3.1** Assembling of the VT-EC-STM 42
  - **3.3.2** STM measurements 43
  - **3.3.3** Electrochemical measurements 44
  - **3.3.4** STS measurements 45
- **3.4 Data evaluation and errors** 45

4. Results 49

- **4.1 Cyclic voltammetry** 50

4.2 Chronoamperometric study of Zn electrodeposition 54

4.3 STM study of electrochemical phase formation of Zn 58

4.3.1 Underpotential deposition of Zn.. 58

4.3.2 Overpotential deposition of Zn.. 65

4.3.3 Dissolution of Zn.. 67

4.4 STM study of Zn UPD at 50 °C 72

4.5 STS measurements 74

5. Discussion 79

5.1 Layer-by-layer mechanism of Zn deposition 79

5.2 Zn-Au surface alloying 85

5.3 Nucleation and growth of Zn 88

5.4 Spinodal decomposition and 2D phase formation 95

5.4.1 Spinodal decomposition 95

5.4.2 2D phase formation of zinc 96

5.4.3 Experimental observations of spinodal decomposition in some other systems 99

5.4.4 Theoretical model for Zn 2D phase formation...................................... 102

Manufacturer list 109

References 111

Curriculum Vitae 119

Acknowledgment 121

Zusammenfassung

Schwerpunkt der vorliegenden Arbeit sind Untersuchungen zur elektrochemischen Phasenbildung in 2 and 3 Dimensionen mit Nanometer Auflösung. Hierzu wurde am Beispiel von Zn die Elektrodeposition im Unter- (UPD) und Überpotential (OPD) *in-situ* mit Hilfe von Rastertunnelmikroskopie (STM) aufgeklärt. Der überwiegende Teil der Messungen erfolgte bei Raumtemperatur, erste Experimente bei erhöhten Temperaturen wurden durchgeführt. Dies erforderte eine Neukonstruktion der elektrochemischen Messzelle und des STM-Aufbaus, die beschrieben werden. Um die in wässrigen Elektrolyten unvermeidliche H_2-Entwicklung und deren negativen Einfluss auf die Morphologie des abgeschiedenen Zn auszuschliessen, wurden hier erstmals elektrochemische SPM Experimente mit einen ionischen Elektrolyt, der Lewis-sauren Ionenflüssigkeit Aluminiumchlorid – 1-butyl-3-methylimidazoliumchlorid, an der Grenzfläche zu einer Au(111) Elektrode durchgeführt. Die SPM Messungen wurden durch *in-situ* Zyklovoltammetrie und Chronoamperometrie ergänzt.

Die wichtigsten Ergebnisse lassen sich wie folgt zusammenfassen.

Die Unterpotentialdeposition von Zink folgt einem Schicht-auf-Schicht Wachstum. Erstmals in dieser Arbeit wurde die Bildung von drei aufeinanderfolgenden Zn Monoschichten im UPD Bereich beobachtet. Die Dicke einer Zn Schicht im UPD und OPD Bereich liegt bei 2.4±0.2 Å, wobei für die erste Schicht dieser Wert 2.2±0.2 Å beträgt. Es wurde gezeigt, dass die Unterpotentialeabscheidung von Zink aufgrund einer Zn-Au Oberflächenlegierung komplex ist. Die Oberflächerlegierung manifestiert sich in den STM-Bildern nach der Zinkauflösung, wobei die Schichtdicke der Legierung von der Anzahl der abgeschiedenem Zinkmonoschichten abhängig ist. Die gleiche Art des Wachstums setzt sich in den Überpotentialbereich fort bis hin zur Bulkdeposition des Aluminiums. Die Unterpotentialabscheidung von Al ist bei -100 mV vs. Zn/Zn(II) mit der Bildung einer Überstruktur gekennzeichnet. Die Überstruktur hat eine hexagonale Ordnung mit einem Abstand nächster Nachbarn von 22.5±2 Å und einer Modulationsamplitude von ~0.9 Å. Die Kinetik der elektochemischen Abscheidung von Zink kann durch zwei Beiträge beschrieben werden – Adsorption und hemispherische Diffusion.

Die effektive Tunnelbarriere ϕ wurde erstmals in dieser Arbeit mit STS gemessen. Die bestimmten Tunnelbarrieren sind deutlich kleiner als die entsprechenden Werte an der Metall/Vakuum-Grenzfläche. Für den Tunnelprozess in Flüssigkeiten, vor allem in dieser Schmelze, war dies zu erwarten.

Eine erste Übersicht über die 2D Phasenbildung von abgeschiedenem Zink an der Elektrolyt / Elektrode – Grenzfläche wurde mit Hilfe der STM-Bilder bei verschiedenen Zeiten und Spannungen gewonnen. Während einer Schichtbildung wurde die Erscheinung einer Labyrintstruktur beobachtet, die für eine spinodale Entmischung charakteristisch ist. Dies weist einen Phasenübergang erster Ordnung auf, der erstmals in dieser Arbeit im Falle der 2D Elektrodeposition beobachtet wurde. Die typische Wellenlänge, die aus dem Strukturfaktor bestimmt wurde, liegt bei ~5 nm. Die Ergebnisse wurden mit Modellrechnungen der spinodalen Entmischung an der Elektrolyt / Elektrode – Grenzfläche unter den entsprechenden Bedingungen verglichen.

Abstract

The aim of this work is study of electrochemical phase formation in 2 and 3 dimensions with nanometer resolution. For this propose, Zn electrodeposition in the under- (UPD) and overpotential (OPD) ranges by means of *in-situ* Scanning Tunneling Microscopy (STM) was examined. The major part of this work was performed at room temperature. First measurements at elevated temperature were conducted. This required an improvement in the construction of the electrochemical cell and modification of the STM-setup, which will described. To avoid the H_2-evolution, which takes place in aqueous electrolytes and has a negative influence on the morphology of the deposited Zn, the electrochemical SPM measurements were performed for the first time in a ionic liquid, Lewis acidic aluminum chloride – 1-methyl-3-butylimidazoliumchlorid, on Au(111) interface. The SPM measurements were supported by *in-situ* cyclic voltammetry and chronoamperometrie.

The essential results of the present study can be summarized as follows.

The underpotential deposition of Zn follows a *layer-by-layer* growth. For the first time the formation of three successive Zn monolayers has been observed in the UPD range. The thickness of the Zn layers in the UPD and OPD range has a value of 2.4±0.2 Å, whereas for the first monolayer it is 2.2±0.2 Å. It has been shown, that the UPD of Zn is complicated due to surface alloying. The STM study on the Zn dissolution gives evidence of Zn-Au surface alloying, where the penetration depth of Zn into Au is strongly affected by the number of the deposited Zn monolayers. The same growth mechanism extends from the UPD into OPD range until Al bulk deposition sets in. The UPD of Al at -100 mV *vs*. Zn/Zn(II) is marked by Moiré pattern formation. The Moiré pattern has a hexagonal long-range order with a lattice constant of 22.5±2 Å and modulation amplitude of ~0.9 Å. The kinetics of Zn electrodeposition is described by the sum of two contributions – adsorption and hemispherical diffusion. For the first time in this system the effective tunneling barrier ϕ has been measured by STS. The obtained values are clearly smaller in comparison to the absolute vacuum values of the work function, which is expected in the case of tunneling in a fluid, particularly in the molten salt.

A first insight into the 2D phase formation of electrodeposited Zn at the electrolyte / electrode interface was obtained from STM images at various times and potentials. Before a coherent layer is formed wormlike structures are observed characteristic of spinodal decomposition. This implies a first order phase transition, which has been resolved here for the first time for

2D electrodeposition. From the structure factor of these wormlike patterns a typical length scale of ~5 nm has been determined. These results are compared with model calculations for spinodal decomposition at the electrolyte / electrode interface for the corresponding electrodeposition conditions.

1. Introduction

Metal electrodeposition for a long time has attracted special attention in research and developments mostly due to its great technological importance. Particularly, the zinc electroplating is commonly used in the steel industry for the protection of steel products in corrosive environments [Pletcher 1990]. Although this method is well established nowadays, the initial stages of the zinc electrochemical phase formation are poorly understood. Above all this can be explained by the lack of appropriate methods. Traditionally, such processes as deposition and dissolution of metals are studied with conventional electrochemical techniques, e.g. cyclic voltammetry, chronoamperometry, impedance spectroscopy etc. These methods were applied as well in early studies of the electrodeposition of zinc and its alloys, see e.g. [Chu 1981], [Despic 1982], [Aramata 1994]. Mostly the authors of these studies concentrated on an improvement of the morphology quality by varying different parameters (zinc salts, organic additives, etc). In such a way, only *macroscopic* information about the system of interest was collected.

Investigation of an electrode surface on the *microscopic* level in general can be performed with the following techniques: Low Energy Electron Diffraction (LEED), Auger Electron Spectroscopy (AES), Scanning Electron Microscopy (SEM) or Transmission Electron Microscopy (TEM), etc. However, these methods (and some others) are related to ultrahigh vacuum conditions and consequently can be used only for *ex-situ* measurements. Several research groups found the ellipsometric measurements appropriate for the *in-situ* study of metal electrodeposition. For example, Ohtsuka et al. reported on the *in-situ* ellimpsometric study of the initial layer formation of Zn-Ni alloy [Ohtsuka 1995, 1998]. However, due to the beam size limitations (the minimum radius is at least of the order of ten micrometer), the obtained information had an integral character. This is true for the majority of optical methods (e.g., infrared and surface-enhanced Raman spectroscopy). Hence, the real spatial changes of an electrode on an atomic level remain still beyond the resolution.

With the appearance of Scanning Tunneling Microscopy, one of the Scanning Probe Microscopy (SPM) tools, the situation has been changed and a broad field of research was finally open for investigations. Although this method is relatively young [Binnig 1982, 1983], it has already gained worldwide acceptance by the science community. Not less effective and popular technique, which can provide essentially the same information as the STM, is the Atomic Force Microscopy (AFM).

Basically, in the STM the tunneling current, which flows between a conductive substrate and metal tip, is measured. Because the tunneling current exponentially depends on the distance (decrease of 0.1 nm results in a current increase by factor of ~3) a high vertical resolution can be achieved. The tip is scanned over the substrate surface and the variation in the tunneling current (or of the height) is measured. In this way information is obtained with atomic resolution of the specific surface features.

The STM has found an application for a wide range of investigations. The interest in this tool has significantly increased, when it was shown that the STM can be also used for the study of surfaces immersed in a fluid, see e.g. [Bard 1986]. This initiated the appearance of the Electrochemical Scanning Tunneling Microscopy (EC-STM), where the STM-setup is combined with an electrochemical environment. Thus, new possibilities for the *in-situ* study of electrochemical phase formation have been opened. Above all, to this subject belongs: the study of anion adsorption, underpotential and overpotential deposition (UPD and OPD) of metals, surface alloying etc. The presence of the latter, for instance, can be unambiguously proved by cyclic voltammetry, linear sweep voltammetry, potentiostatic transient technique measurements. However, the atomic structure of such a process remains unknown. At the same time, only with the help of the SPM an answer on such kind of questions could be provided.

The same concerns the UPD of metals. Initially, this processes was interpreted in terms of a continuous adsorption, see e.g. [Pangarov 1983]. Only later with the invention of the EC-STM this phenomenon was treated as first order phase transition, which results in a condensation of metal phase [Staikov 1998]. The UPD mechanism is very complex and can be affected by a number of additional processes – anion adsorption, surface reconstruction etc. So, only proper correlation of electrochemical and STM measurements allows a reasonable interpretation of observed changes on an electrode surface on the atomic or nanometer scale

Apart from the nucleation and growth during metal deposition, recently another type of structure evolution at the surface has been found – two-dimensional (2D) spinodal decomposition [Schuster 2003]. The knowledge of spinodal decomposition processes at the surface is of particular importance for its potential applications (stability of thin films, selforganization of nanocrystals etc). The 2D spinodal decomposition is characterized by the appearance of *wormlike* or *labyrinth* interconnected structures on the nanoscale.

The metal electrodeposition from an aqueous electrolyte solution, in general, is complicated by hydrogen evolution. Thus, the electrochemical window is limited by the water reduction. In the case of the zinc electrodeposition the hydrogen evolution can strongly influence the morphology, [Despic 1982], [Aramata 1992]. A solution to this problem is applying of molten salts or ionic liquids. At the moment the classical molten salts, which require high temperature operation, are replaced by much easier to handle *low* or *room temperature molten salts* [Hussey 1994], [Carlin 1994], [Welton 1999]. The molten salts posses several advantageous and outstanding properties, which make them favorable in comparison with aqueous solutions. Their large electrochemical windows allow performing the deposition of light metals and semiconductors, which are not accessible in aqueous electrolyte solutions. Moreover, these melts exhibit essentially no vapor pressure [Welton 1999].

Low melting point molten salts, which are liquid below 100 °C, can be, for example, obtained by the combination of 1-ethyl-3methylimidazolium chloride (EMIC) and metal halides. The $ZnCl_2$/EMIC molten salt is frequently applied to obtain Zn-Me alloys [Chen 2000, 2001], [Lin 2001]. Since by combination of $AlCl_3$ and EMIC a new class of room temperature molten salt was developed [Wilkes 1982], the chloroaluminate molten salts have become most frequently used ionic electrolytes nowadays. Besides properties common to all molten salts, a mixture of $AlCl_3$ and organic salt allows electrodeposition of Al-Me alloys without additional co-solvents.

This kind of melt has been also used for the Zn electrodeposition. Hussey and Pitner reported about an electrochemical phase formation of Zn on platinum, tungsten, gold polycrystalline and glassy carbon electrodes from $AlCl_3$/EMIC molten salt [Pitner 1997]. With the help of the conventional electrochemical techniques – cyclic voltammetry and chronoamperometry – the UPD of Zn on all these electrodes, with exception of carbon, was observed.

A special subclass of chloroaluminate molten salts has been obtained by the mixing of $AlCl_3$ and 1-butyl-3-methylimidazolium chloride (BMIC). Although, $AlCl_3$/BMIC with respect to its physical properties is very similar to the $AlCl_3$/EMIC molten salt, the former has special advantages improvements over the latter one. Particularly, it is liquid at room temperature already. As a disadvantageous one has to mention extreme hygroscopicity of the $AlCl_3$/BMIC molten salt, what concerns all chloroaluminate based systems, though. Thus all experimental preparations and measurements have to be conducted under inert atmosphere or vacuum.

The major part of this work is dedicated to the *in-situ* SPM study of Zn electrodeposition on Au(111) from the $AlCl_3$/BMIC room temperature molten salt. The system is very close to that studied by Hussey and Pitner [Pitner 1997]. However, there are still a number of open questions, above all it concerns the UPD range, which could not be clarified completely in their work. In this sense, the EC-STM is unique, since it offers a complete understanding of the processes on a nanometer scale.

The STM measurements of this work at elevated temperature required the improvement of some parts of the existing Electrochemical Variable Temperature Scanning Tunneling Microscope (EC-VT-STM) [Shkurankov 2002], namely, the construction of the electrochemical cell. Thus in the course of this work, several modifications have been performed. For the measurements at elevated temperature a new STM tip coating by glass capillaries has been developed, since the usually employed epoxy-paint lost its insulating properties with increasing temperature. The new coating consists of melting a small glass capillary on the Pt/Ir tip, leaving only a tiny tip apex free.

In the light of the problems given above the objectives of this thesis can be summarized as follows. A major part deals with aspects of Zn underpotential deposition. This includes several interesting topics, which are:

- clarification of 2D layer formation by *in-situ* STM,
- development of 2D structure and its relation with spinodal decomposition,
- morphology of UPD deposition and its growth mechanism,
- quantification of electronic structure of the UPD films by STS.

Besides, the whole deposition process of Zn on Au(111) from the Lewis acidic $AlCl_3$/BMIC room temperature molten salt both in the UPD and OPD ranges is characterized with respect to:

- structural changes at interface of electrodeposit / Au(111) substrate with the aim to get direct insight, in real space, on surface alloying,
- comparison of STM results with information from conventional electrochemical measurements on the growth mechanism and kinetics.

10

2. Basic concepts of the experimental techniques

In this chapter a short overview of the theoretical aspects of the techniques used in this work is given. The *scanning tunneling microscopy* (STM) is based on the exponential dependence of the tunneling current, flowing from one electrode onto another one, on the distance between electrodes. Combination of the STM with an electrochemical cell allows *in-situ* study of metal electrochemical phase formation. With the help of *scanning tunneling spectroscopy* (STS) additional quantitative information about the surface local electronic structure can be obtained. The tunneling spectroscopy is directly related to the STM and, from measurement of the tunneling current *vs*. tunneling voltage, effective tunneling barrier can be evaluated. C*hronoamperometry* is very powerful method for the quantitative analysis of a nucleation process. Integrated together, all mentioned above techniques allow to obtain a detailed picture of the studied system and above all *in-situ*.

2.1 Scanning Tunneling Microscopy

Principle of STM. Scanning tunneling microscopy is based on the quantum mechanical effect of electron tunneling. Two electrodes (in the case of STM one of two electrodes is a metal tip and the second one is a conducting surface under study) are brought very close to each other and by applying a bias voltage (approx. several volts) between them, the tunneling current, typically on the order of a few nA, will flow and can be precisely measured. The arising current depends exponentially on the tip-surface distance. This property of the tunneling current plays the crucial role in STM and allows to control the sample-tip separation with high vertical resolution. An STM image is obtained while the tip scans over the surface and corresponds quite closely to topography of the surface electronic states. Schematically, the principle of the STM is shown in Fig. 2.1.

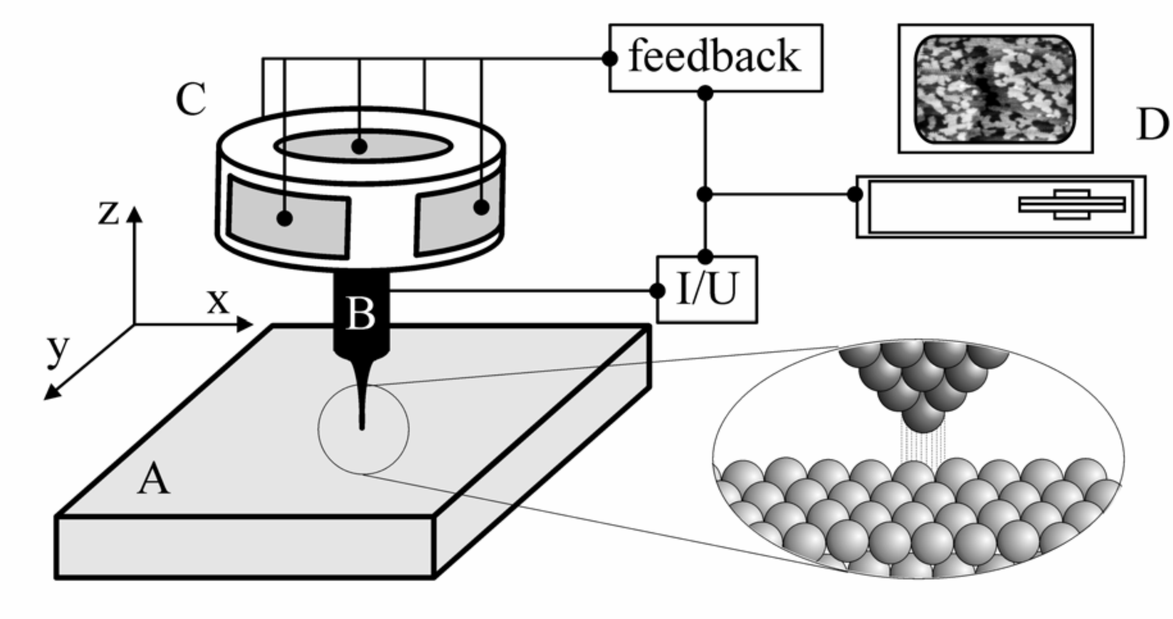

Fig. 2.1 *The principle setup of STM. The STM tip,* ***B****, scans over the substrate,* ***A****. The tip is connected to the piezo,* ***C****, which is controlled by feedback. The STM image can be obtained by holding the current, I, or bias, U, constant. The controller,* ***D****, governs the whole system and transforms the tunneling signal in a gray scale image.*

Tunneling current. Quantum mechanics states that a particle can go through a potential barrier with height V and certain thickness z [Atkins 2000]. In Fig. 2.2 the trace of the particle with wave function $\psi(x)$ through the tunneling barrier is shown. The wave function oscillates on both sides of the barrier, but the amplitude of oscillations is smaller after passing the barrier. Inside the barrier $\psi(x)$ falls exponential. So, there is some probability $T(E)$ that the particle can be found on the other side of the barrier, in spite of the fact, that it has not enough energy to overcome it according to the classical approach. With the help of the Schrödinger equation the tunneling transmission probability (which is, in principle, the tunneling current I) for a particle with mass m and kinetic energy E can be written in form of Eq. 2.1. The main feature of this equation is the, already mentioned, exponential dependence of the tunneling probability on the thickness of the barrier, what is in our case the distance between two electrodes. This equation is simplified and can be used in the first approximation only.

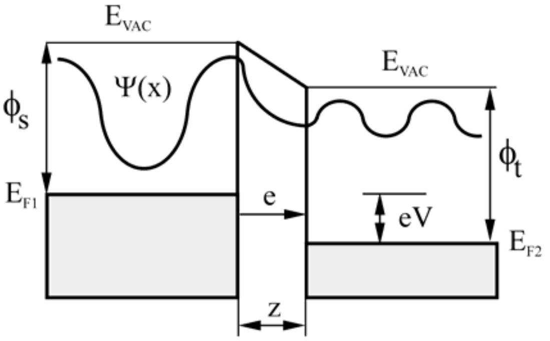

$$I \approx \exp(-2\kappa z) \tag{2.1}$$

$$\text{with } \kappa = \frac{\sqrt{2m(V-E)}}{\hbar} \tag{2.2}$$

Fig.2.2 *Schematic representation of the electron tunneling between two electrodes. At the equilibrium the Fermi levels, E_F, of the tip and sample are equal, by applying bias voltage, eV, the Fermi level of the tip (or of the sample) will be shifted and electrons will tunnel from one side to another one. The tunneling current arising in such a case is given by Eq. 2.1, where V is the height of tunneling barrier.*

To approach experimental conditions a mathematical description of the tunneling current requires a careful consideration of the effect of the real surface structure (both of the sample and tip). Several theoretical treatments of STM exist at the moment in literature, see e.g. [Drakova 2001], [Corbel 1999]. Most popular of them are based on the perturbation approach within Bardeen's tunneling current formalism [Bardeen 1961]. Additional approximations are done normally by different descriptions of the tip and sample eigenstates, influence of the temperature and bias [Bai 1992]. Tersoff and Hamann were first, who suggested presenting the tip as hemisphere of free-electron metal [Tersoff 1983, 1985]. Their idea of a tip model is shown in Fig. 2.3. The wave function of the tip was replaced by an s-type function and the sample local density of states was evaluated in the center of curvature r_0 of the tip. According to this model the tunneling current is proportional to the sample density of the tip and sample, Eq. 2.3-4, where ϕ is the work function of both the tip and sample (for simplicity they were assumed to be equal), ρ_s and ρ_t are the density of states of the tip and sample.

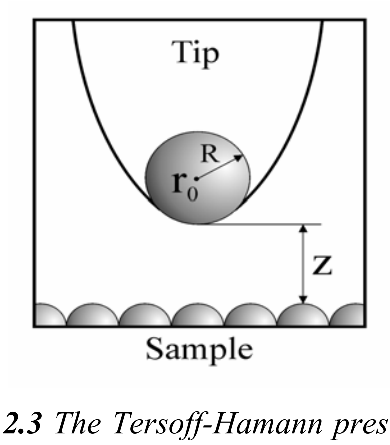

$$I = \frac{32\pi^3 e^2}{\hbar} V \frac{\phi^2}{\kappa^4} R^2 \rho_t(E_F) e^{2\kappa R} \rho_s(r_0, E_F) \tag{2.3}$$

$$\text{where } \rho_s(r_0, E_F) \propto e^{-2\kappa(R+z)} \tag{2.4}$$

Fig. 2.3 *The Tersoff-Hamann presentation of tunneling geometry [Tersoff 1983]. The tip has spherical shape of the apex, where R is radius of curvature.. The tunneling current on the distance z is given by Eq. 2.3-4, for k see Eq. 2.2.*

The tunneling current of Tersoff and Hamann has, as in the simple case – see Eq. 2.1-2, the exponential dependence on the distance and the main advantage of this model is its relative simplicity. Besides that, only in a special class of surfaces the deviations from the behaviour expected for s-wave tip will be significant [Tersoff 2001].

Tunneling in electrolytes. It is clear, that the mechanism of tunneling in the presence of electrolytes should differ from that in vacuum, but at the moment very little is known about this problem. Several experimental works were performed in this direction and they all agreed that the tunneling current retains the exponential dependence on the tip-sample distance, see e.g. [Moffat 1999]. It was also discovered that the tunneling barrier is diminished by the solvent and various explanations of that can be found. Moreover, experimentally measured tunneling barriers are usually difficult to reproduce and different scientific groups obtained differing results, see e.g. [Halbritter 1995]. In principle it is not surprising, because of a variety of all possible impurities, which are usually present between the tip and the sample, might play a significant role here. Furthermore, the tip by itself from measurement to measurements has slightly different geometries, what in turn can reveal diverse electronic structures.

In discussion of the tunneling through a fluid medium, in general two influences in comparison with vacuum have to be considered. The first one is attributed to the reduction of work function, and thus the height of tunneling barrier, due to adsorption of the fluid molecules on the tip and electrode, respectively. This effect is more or less quantitatively understood and can be described in two ways: classically by dipolar layer and quantum chemically by DFT calculations of surface states in frames of the jellium model [Venables 2000]. The second aspect, which has an impact on the tunneling through the fluids, is the presence of so-called resonant and unresonant states [Halbritter 1995, 1998], [Repphun 1995]. The surface covered by a liquid results in a complex tunneling barrier, what allows the electrons to occupy some specific intermediate states, e.g. dipole resonances [Repphun 1995]. According to such a model, the tunneling occurs via these intermediate states. In an aqua solution water dipoles, which are located in the electrochemical double layer, cover the tip and substrate. On the small distance (<1 nm) the double layers of the tip and substrate overlap, what leads to the appearance of resonant states and to reduction of the tunneling barrier height [Halbritter 1995].

Unfortunately, the model which would properly describe the tunneling in the molten salts does not exist at the moment. However, on the basis of the small introduction to this problem given above, it is reasonable to expect the lowering of the tunneling barrier height in ionic liquids in comparison to vacuum.

Operating modes of STM. The tunneling current, as it can be seen from Eq. 2.3, depends not only on the tip-sample separation but also on the electronic structure of the sample and of the tip. For many materials of the tip (metals) such contribution can be assumed to be minimal and the final STM image can be usually attributed to electronic properties of the sample only. As far as the size of the studied area is in the nanometer range, the corresponding STM image can be understood as the topography of the surface.

To produce an image, the STM can be operated in the *constant current* or *constant height* modes, which are schematically presented in Fig. 2.4.

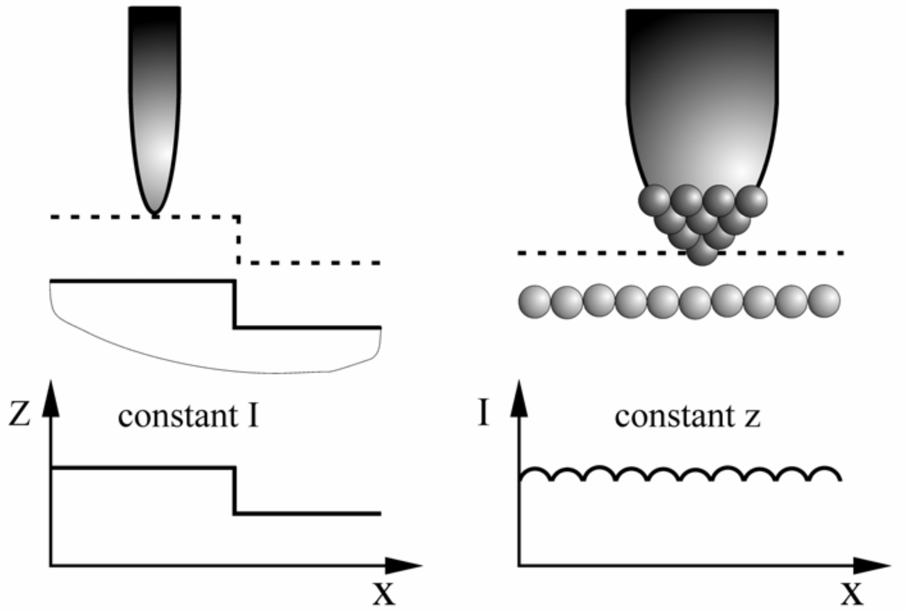

Fig. 2.4 *Two operating modes of STM,* ***a)*** *constant current, where variations of height are measured and* ***b)*** constant *height, where changes of current are recorded.*

In the first case the current is held constant while the tip scans in the (*x*,*y*) plane. The control over the tip movement in the vertical direction is performed with the help of the feedback mechanism, while a constant bias is applied between the tip and sample, Fig. 2.4a. The final STM image represents a 2D array of heights at some specific surface features. Due to the limitations of the feedback electronic and mechanical vibrations of the piezo, this operation mode is commonly performed at relatively small scan rates: 1 - 5 Hz.

In the constant height operating mode the height and bias are simultaneously maintained constant, whereas a variation of tunneling current is measured. These variations arise during scanning over different surface structures, Fig. 2.4b. The image in this case reveals changes of the current. The advantage of this mode is a faster scan rate, which is not limited now by the time response in *z*-direction. However, this is useful only for very flat surface, such as HOPG[1], for example, or very small area. Otherwise, there is a certain danger to destroy the tip apex. The atomic resolution is obtained in this mode.

For imaging of structures, with sizes of order of several μm to several hundreds nm (steps, clusters, etc.) the constant current mode is normally preferred.

2.2 Scanning Tunneling Spectroscopy

The sensitivity of scanning tunneling microscopy to a bias voltage and correspondingly to the density of the states of the sample and the tip has two main implications. First, the tunneling microscopy does not reveal the positions of atoms themselves, but the energy density of states, and second with the help of STM it is possible to obtain spectroscopic information (STS) with atomic spatial resolution.

Principle of STS. The technique is directly related to the STM and its principle is schematically shown in Fig. 2.5. STS curves for fixed separation are obtained by measuring the variation of the tunneling current *I* at constant tip-sample separation as a function of the bias voltage U. At a particular place of interest on the surface the position of tip is held constant. During this time the bias voltage (*U*) is linearly ramped between two given values (U_{max} and U_{min}), Fig. 2.5a, and the corresponding current is recorded, Fig. 2.5b.

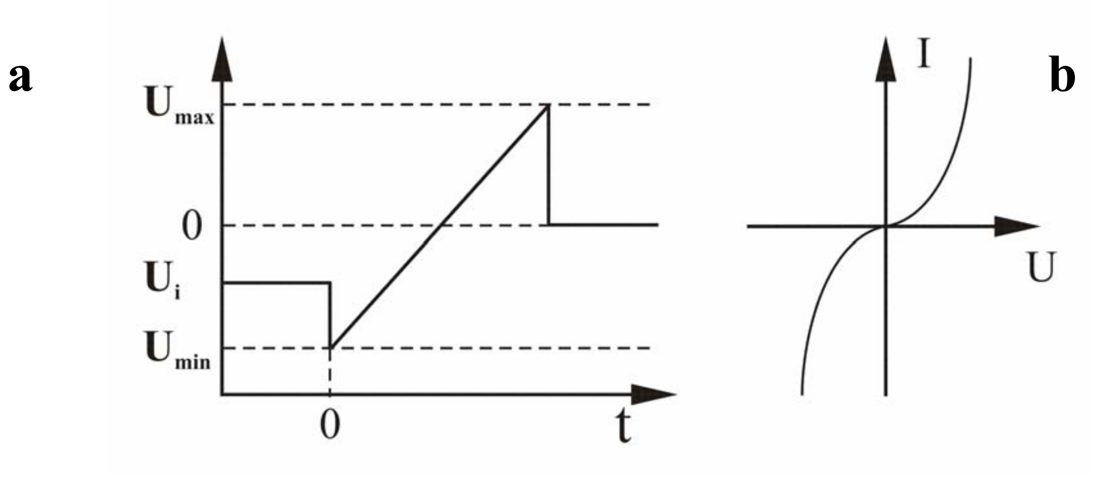

Fig. 2.5 *The principle of STS measurement.* ***a)*** *Changes of the tunneling voltage during performance of spectroscopic measurements;* U_i *is initial bias,* U_{max} *and* U_{min} *are two limits, which are equal in absolute value.* ***b)*** *The corresponding current-voltage curve.*

---

[1] Highly Oriented Pyrolytic Graphite.

Let's consider what happens with energy levels involved in the tunneling during the sweeping of the potential from U_{min} to U_{max}. In Fig. 2.6 the schematic presentation of that process is shown, where at the beginning the simplest case is considered – zero bias voltage (U=eV=0), Fig. 2.6a.

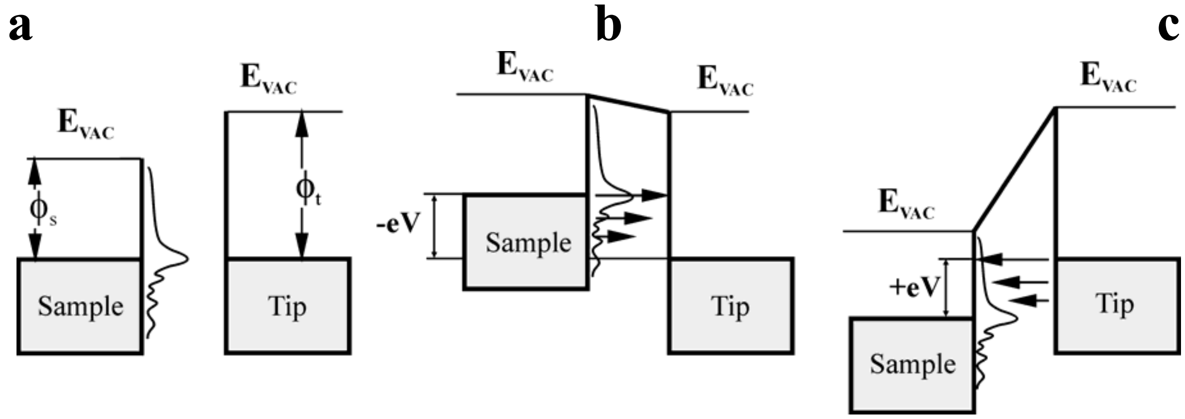

Fig. 2.6 The energetic scheme of tunneling under STS experiment. ***a)*** *Zero bias voltage, the tip and substrate are in equilibrium, no tunneling.* ***b)*** *Negative bias is applied to the sample, the electrons from occupied sates of the sample tunnel into unoccupied states of the tip.* ***c)*** *Positive bias is applied to the sample, the situation is reverse to b).*

By applying negative bias voltage to the sample the Fermi level (upper border of the gray field in Fig. 2.6) is shifted and electrons are forced to travel into another side – into unoccupied sates of the tip, Fig. 2.6b. By applying the positive sample bias, the situation will be reversed and electrons from the tip will tunnel into the sample unoccupied states, Fig. 2.6c. Thus the tunneling will be each time initiated by the states lying between the E_F and E_F + eV. These states have a broad range and exert an influence on the resolution of the tunneling spectroscopy. Hamers and Padowitz considered the tunneling transmission probability, T, as a function of energy for two cases – with and without thermal effect on electrons [Hamers 2001]. It was shown, that for both cases $T(E)$ has asymmetric form with the sharp increase at E_F. This fact helps to obtain higher resolution when the tip probes empty states of the sample, than occupied states (in other words, when positive sample bias is applied to the sample, see Fig. 2.6c).

Theoretical aspects of STS. By measuring the dependence of tunneling current on the bias voltage it is possible to receive the spectra containing information about a work function or density of states of the surface in the case of tunneling in vacuum. In order to evaluate the spectroscopic information quantitatively it is necessary to consider more precise description of the tunneling, than it is given by Eq. 2.3-4. Namely, the tunneling current, which is proportional to the tip and sample density of states and tunneling transmission probability, has to be integrated over the applied tunneling bias voltage. For metals one can assume that density of states for sample and tip are constant and it can be shown that tunneling current can be approximated as, see e.g. [Hamers 2001]:

$$I = C\int_0^V \exp(-Az\sqrt{\phi - V})dV, \tag{2.5}$$

where $\phi = (\phi_s + \phi_t)/2$ is the average work function, $A = 2\hbar^{-1}\cdot(2m)^{1/2} = 1.025\ \mathrm{eV}^{-1/2}\text{Å}^{-1}$ and C is some constant, containing the tip and sample density of states. Analyzing this equation, it can be noticed, that for material with high work function an increase of the applied voltage gives only small contribution in the argument of Eq. 2.5 and the integral tends to be linear. For material with low ϕ the applied voltage makes the exponential factor greater and integral rapidly increases as an exponential function. Simple integration of (2.5) yields:

$$I=C\cdot((1+Az(\phi-V)^{1/2}exp\{-Az(\phi-V)^{1/2}\}-(1+Az\phi^{1/2}exp\{-AZ\phi^{1/2}\}). \tag{2.6}$$

This equation is used for theoretical description of experimental I-U curves of this work in order to obtain average work function of the tip and sample (Chapter 4.5).

It is important to stress, that for tunneling in a fluid medium ϕ plays the role of an effective tunneling barrier, i.e. strong reduction of vacuum work function by adsorption is taken into account (see above). So only the relative change of ϕ as a function of the system parameters (like potential, temperature etc) gives information on the variation of the effective structure assuming that adsorption is constant.

2.3. Electrochemical methods

2.3.1. Cyclic voltammetry

To receive the preliminary information about a new system the cyclic voltammetry (CV) is nearly always the technique of first choice. The cyclic voltammetry can be applied for a study of all electrochemical reactions without limitations. With the help of this method, it is possible to get information about the type of reactions observed in the system and the potentials at which they occur. CV is also frequently used for measurements of the diffusion coefficients. At the same time this technique is unfortunately not the best one to obtain quantitative data about electrochemical nucleation processes.

Principle of CV. Briefly, this method can be introduced as a reversal technique, which involves sweeping the electrode potential between two limits at a known sweep rate. At the beginning the working electrode is held at some potential, E_i, where no electrode reactions occur. During measurement the potential is swept linearly at a rate v between two limiting potentials E_1 and E_2, Fig. 2.7a. So, at any time t the potential is:

$$\begin{aligned} 0 < t < \tau \qquad & E(t) = E_i - vt \\ t > \tau \qquad & E(t) = E_i - 2v\tau + vt, \end{aligned} \tag{2.7}$$

where τ is the time required for scan in one direction. The same sweep rate is normally chosen for the forward and reverse sweep. Its typical value lies in the range from several mVs^{-1} to several Vs^{-1}. The corresponding current is recorded as a function of the varying potential. A theoretical cyclic voltammogram for a reversible system is shown in Fig. 2.7b.

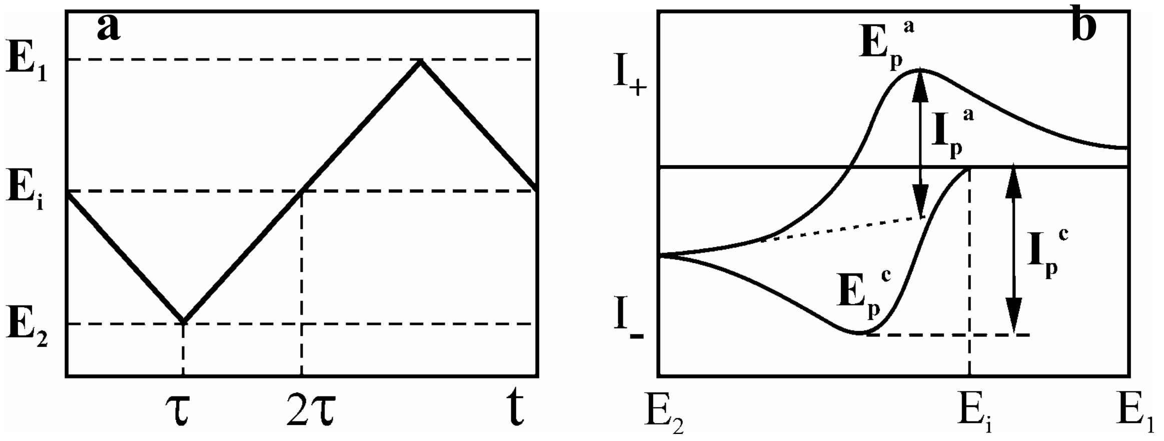

Fig. 2.7 Cyclic potential sweep voltammetry. ***a)*** *Potential sweep during cyclic voltammetric measurement;* E_i *is initial value,* E_1 *and* E_2 *are two limiting values.* ***b)*** *A typical cyclic voltammogram of a reversible reaction; letters "a" and "c" are referred to anodic and cathodic process,* E_p *and* I_p *are potential and current peak.*

For the cathodic scan (applied potential is decreasing) the current has a negative sign, for the anodic scan (applied potential is increasing) the current has a positive sign.

Reversible reaction. To obtain the exact form of the cyclic voltammogram it is necessary to solve the Fick's second Law for **O** and **R** with the appropriate boundary conditions. Let's consider a reversible reduction of a species O

$$\mathbf{O} + \mathbf{n}e^- \leftrightarrow \mathbf{R}, \tag{2.8}$$

which takes place at a planar electrode and assume that a solution initially contains only O species. According to the Fick's first Law the current density is proportional to the concentration gradient of O at the electrode:

$$I = -nFD_0\left(\frac{\partial c_0}{\partial x}\right)_{x=0} \tag{2.9}$$

where *F* is the Faraday constant, *D₀* is diffusion coefficient of **O**, *c₀* is concentration of **O** and *x* is distance from the electrode surface. This equation is valid if all other mechanisms of mass transport (such as migration and convection) can be neglected. In other words it means that diffusion is the sole mode of the mass transport. In diluted and unstirred solutions at constant temperature this can be taken as a good approximation [Bard 2001].

If these conditions are fulfilled, then the cyclic voltammogram is a result of the solution of the Fick's second Law:

$$\text{a) } \frac{\partial c_O}{\partial t} = D_0\frac{\partial^2 c_O}{\partial x^2} \quad \text{and} \quad \text{b) } \frac{\partial c_R}{\partial t} = D_R\frac{\partial^2 c_R}{\partial x^2}, \tag{2.10}$$

with the following boundary conditions:

$$\begin{array}{lll} t=0, x\geq 0 & c_O = c_O^\infty \text{ and } c_R = 0, & \text{a} \\ t\geq 0,\ x\to\infty & c_O = c_O^\infty \text{ and } c_R = 0, & \text{b} \\ t>0, x=0 & \left\{\begin{array}{l} D_0\left(\frac{\partial c_O}{\partial x}\right) = -D_R\left(\frac{\partial c_R}{\partial x}\right), \\ \left(\frac{c_O}{c_R}\right)_{x=0} = \exp\left\{\frac{nF}{RT}\left(E-E^0\right)\right\}, \end{array}\right. & \begin{array}{l}\text{c} \quad (2.11) \\ \text{d}\end{array} \end{array}$$

where E^0 is the equilibrium potential under standard conditions, *c* and *D* are concentration and diffusion coefficient of the species **O** and **R**, respectively, other parameters have their usual meaning (see also Eq. 2.9).

The first three conditions, 2.11a-c, are quite general, whereas the last one, 2.11d, holds only for a reversible reaction (reaction, for which the electron transfer is so fast that for any change in electrode potential Nernstian equilibrium is always maintained [Southampton 1990]).

The solution of this problem is quite difficult and details can be found, for example, in [Bard 2001]. The final result at 25 °C for the peak current is given by the following expression:

$$I_p = (2.69{\cdot}10^5)n^{3/2}AD_O^{1/2}v^{1/2}c_O^\infty, \tag{2.12}$$

where *A* is the electrode area. One can see that the peak current is proportional to the concentration of O species and to the square roots of sweep rate and the diffusion coefficient. Thus a simple test of the reversibility of the system can be made. If the system is reversible, then a plot of I_p as a function of $v^{1/2}$ should be linear and passes through the origin. In this case the diffusion coefficient can be estimated from the slope.

Irreversible reaction. The shape of cyclic voltammogram can be altered, if the electron transfer is very slow and surface equilibrium is not maintained. Such system is called irreversible. In this case the following expression for the peak current at 25 °C [Bard 2001]:

$$I_p = (2.69{\cdot}10^5)\alpha^{1/2} nAD_O^{1/2} v^{1/2} c_O^{\infty}, \tag{2.13}$$

where α is an electron transfer coefficient.

For an irreversible system the peak current density is also proportional to the square root of the scan rate, but the peak potential shifts in the negative direction on $30/\alpha$ mV for each decade increase in the scan rate.

For both (reversible and irreversible) systems there are a number of additional criteria, which should be satisfied [Southampton 1990]. They are summarized in Tab. 2.1.

Table 2.1 *Diagnostic tests of reversibility and irreversibility of a system; letters "a" and "c" referred to anodic and cathodic process,* $E_{p/2}$ *is half peak potential,* α *is an electron transfer coefficient.*

reversible process	*irreversible process*
$I_p \sim \sqrt{v}$ $\left\|I_p^A / I_p^C\right\| = 1$ E_p independent of v $\left\|E_p - E_{p/2}\right\| = \left\|E_p^A - E_p^C\right\| = \ln 10 \frac{RT}{nF}$	No reverse peak $I_p^C \sim \sqrt{v}$ E_p^C shifts on $30/\alpha$ mV for each decade increase in ν $\left\|E_p - E_{p/2}\right\| = 48/\alpha$ mV

Reversibility of a system can be strongly affected by the time scale of the experiment. It is possible, that the system satisfies the reversible criteria at low sweep rates and becomes irreversible at higher sweep rates. It should be also mentioned, that sometimes a studied system can be even more complicated, if several processes overlap. Their analysis then is not always straightforward.

2.3.2. Chronoamperometry

Chronoamperometry is a technique, which consists basically in applying some constant potential to the working electrode and recording the current-time response. This is a very useful technique for obtaining initial information about nucleation and growth in a studied system. From the current-transient curve such quantities of the system as a diffusion coefficient and amount of charge for deposition can be determined. Also, this method can be applied for the determination of a nucleation rate constant and an adsorption isotherm [Southampton 1990].

Principle of chronoamperometry. Consider again a reversible reaction, Eq. 2.8. At the beginning of the transient experiment the potential of the working electrode is held at E_i, Fig. 2.8a. At t=0 the potential is instantaneously changed to a new value E_1, Fig. 2.8a, and corresponding current-time response is recorded. An example of the current response is shown in Fig. 2.8b.

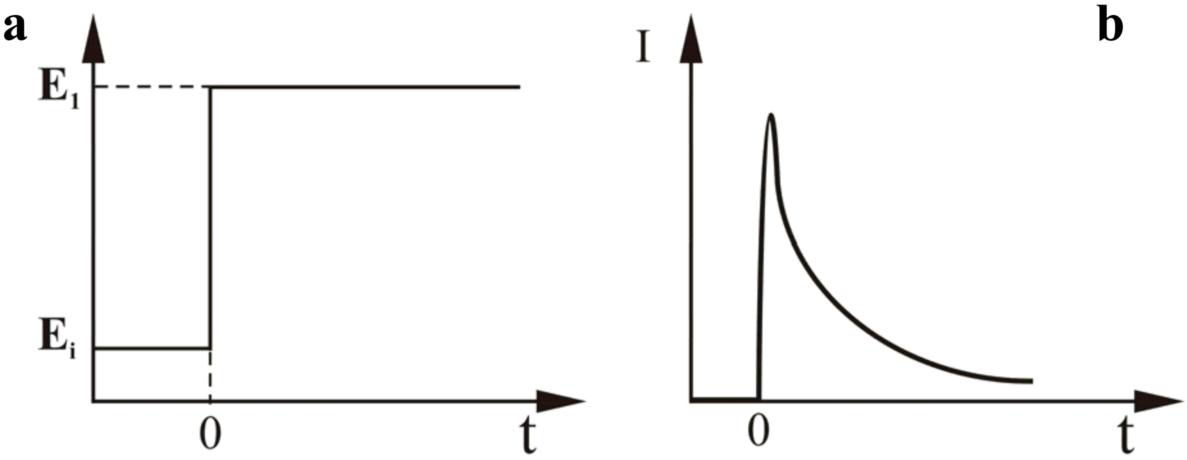

Fig. 2.8. *The chronoamperometric experiment.* ***a)*** *The potential-time profile applied during experiment, E_i is initial value and E_1 is the potential where no reduction of O occurs or some other potential of interest.* ***b)*** *The corresponding response of the current due to changes of the potential.*

Solution of the diffusion equation. In order to determine the exact form of current-time dependence it is again necessary to solve the Fick's second Law (Eq. 2.10) under the following boundary conditions:

$$t = 0, x \geq 0: \quad c_O = c_O^\infty, \qquad \text{a}$$

$$t \geq 0,\ x \to \infty: \quad c_O = c_O^\infty, \qquad \text{b} \qquad (2.14)$$

$$t > 0, x = 0: \quad c_O = 0. \qquad \text{c}$$

For details of solution of this problem see [Bard 2001]. For a planar electrode the current density is given by the Cottrell equation:

$$|I| = \frac{nF\sqrt{D_O}c_O^\infty}{\sqrt{\pi t}}. \tag{2.15}$$

For diffusion controlled process it can be noticed that the current falls as $t^{-1/2}$. This feature is frequently used as a test for this type of process and from the slop of I *vs*. $t^{-1/2}$ the diffusion coefficient D_O can be calculated.

It is important, that such an analysis has to be applied over a broad time interval in order to ensure the reliability of results. At short times the current consists of a large nonfaradaic component due to charging of the double-layer capacitance. The nonfaradic current decays exponentially with time constant R_uC_d, where R_u is an uncompensated resistance and C_d is the double layer capacitance) [Bard 2001]:

$$|I| = \frac{E}{R_u} e^{-t/R_uC_d}. \tag{2.16}$$

Thus, the time constant R_uC_d will determine the shortest time required to conduct the chronoamperometric experiment. Therefore, measurements should be performed for times which are much greater then R_uC_d. After passing the time equal to R_uC_d, the double layer capacitance is charge by 63 % and after $3R_uC_d$ by 95 %, see Eq. 2.16. Thus, knowing the time constant one can easily estimate the time needed for double layer charging.

At long time, however, the natural convection comes into effect and diffusion in that case is not the only mode of the mass transport. Hence, the typical time range of chronoamperometric measurements lies normally in the range from 0.001 to 10 s. However, there are a number of additional instrumental and experimental limitations [Bard 2001]. For example, current and voltage characteristics of a potentiostate can limit the current maximum and time resolution (*potentiostatic limitations*).

Nucleation. The current-transient curve can reveal different behaviour, if, for example, nucleation plays a significant role and the reaction will not be any more purely diffusion controlled. Generally, nucleation can be represented with the help of the following equation:

$$N(t) = N_\infty - N_\infty \exp(-A_o t), \tag{2.17}$$

$$\text{where } A_0 = k \exp\left\{-\frac{\Delta G_c}{RT}\right\}. \tag{2.18}$$

In Eq. 2.17 $N(t)$ denotes a number of nucleation centers per unit area at time t, N_∞ is the number of active sites on the electrode surface, ΔG_c is the activation energy, k is preexponential factor, which depends on experimental conditions and A_0 is the first order nucleation rate constant. A_0 is known to be a function of several parameters (potential, concentration and substrate). For the initial time range two limiting cases of Eq. 2.17 can be considered. If A_0 is large, then all active sites on the surface are occupied by the nuclei essentially at time $t=0$ and

$$N(t)=N_\infty . \tag{2.19}$$

This is referred to as *instantaneous nucleation*. If A_0 is small, only a part of all active sites will be occupied at $t=0$ and the number density will develop with time in the following way:

$$N(t)=N_\infty A_0 t \tag{2.20}$$

Such a process is called - *progressive nucleation*. Both cases were considered by Scharifiker and Hills [Scharifiker 1983] in the model of hemispherical diffusion. The model is based on the assumption, that the growing nuclei are surrounded by some hemispherical diffusion zones. The problem of their overlapping was solved by introducing the concept of an extending area, which is the area that a nucleus would cover without overlapping [Avrami 1940]. The mass transfer occurs by hemispherical diffusion, until the electrode surface is sufficiently dense covered by nuclei. Then the diffusion becomes linear and at longer times the Cottrell equation, Eq. 2.15, can be applied.

Not necessary diffusion is the rate determining step (the slowest step). For example, this can be an incorporation of adatoms in the growing centers, which depends on several factors. Different geometries can be formed.

Generally, if the liquid metal completely wets the electrode surface, then the monolayer growth is expected. Otherwise, the shape will be, for example, hemispherical, conical or needle-shaped. In any case the trend of current-transient curve will have different behaviors and several models are available in literature, which can be applied for such situations [Armstrong 1966], [Bosco 1982], [Southampton 1990] etc.

As it can be noticed, even though the chronoamperometry is relatively simple technique, there is a number of difficulties, which are related to the interpretation of the current-transient curve. Hence, it is very important to find the possibility of comparative analysis of the chronoamperometric results with the results of cyclic voltammetry and scanning tunneling microscopy. This type of comparison will also help to understand the studied system more completely and with better precision.

A detailed analysis of the measurements of this work is presented in Discussion, Chapter 5.3

3. Experimental part

In this chapter the experimental equipment, which has been used and particularly developed in the course of this work is introduced. The experimental assembly includes initial sample, tip and molten salt preparation. First, a brief overview of the main experimental difficulties will be given.

3.1 General problems and requirements

One of the main objectives of this work was the *in-situ* investigation of the electrochemical behavior of Zn(II) in a room temperature molten salt on nanometer scale at different temperatures with the help of electrochemical, variable temperature scanning tunneling microscopy (EC-VT-STM). For the experiments described here the molten salt was produced by mixing two components – $AlCl_3$ and BMIC[1] (1-butyl-3-methyl-imidazolium chloride). The combination of them gives a very interesting result. First, the obtained melt is a liquid already at room temperature. Second, it exhibits a broad electrochemical window in comparison to aqueous solutions (from 2 to 4 V, depending on $AlCl_3$/BMIC ratio). Last but not least, the thermal decomposition of the melt begins well above room temperature (~ 200 °C). These unique properties represent a great advantage for application of this room temperature molten salt in the study of the electrochemical deposition and dissolution of Zn at 25 °C and at elevated temperatures.

---

[1] sometimes referred as MBIC

Unfortunately, there are several essential problems, which can considerably hinder obtaining of experimental results. Above all, it is the extreme sensitivity of the melt to even the smallest amounts of water. The addition of water into the melt leads to an exothermic reaction with the evolution of HCl. As a result of this reaction oxide- and proton-containing species are produced. Depending on the ratio of $AlCl_3$/BMIC the species can have different structures [Zawodzinski 1990], [Trulove 1992]. In principle, if the concentration of them is minute, they do not have a strong influence on the result of electrochemical measurements. But at just a little higher concentration of water a film of aluminum hydroxide will form on the electrode surface. The film brings a negative influence on the electrochemical measurements, as well as on STM experiments. Furthermore, HCl provokes a corrosion of the whole microscope, especially of the scanner.

The study of an electrodeposition (-dissolution) process on nanometer scale imposes special requirements to the substrate and to the STM tip. Very careful control over all possible impurities should be done. The impurities can adsorb on the substrate and lead to worsening of the resolution of STM (due to change of the tunneling barrier height) as well as creation of some pseudo nucleation centers. On the other hand, the substrate has to exhibit big enough terraces (~ 100×100 nm^2 size), were the deposition can be studied. Small terraces have high a density of kink sites, which of course affects a nucleation process. The quality of terraces is determined mostly by the annealing procedure of the Au sample (see Section 3.2.3). There is no exact way how to perform it and normally one has to rely on experience. In the worst case the number of steps between terraces will be so high, that it will be almost impossible to find a flat uniform terrace of sufficient size on the substrate.

Also the resolution of scanning tunneling microscopy (in other words – quality of obtained information) is strongly affected by the tip shape. Blunt tips produce images with somewhat lower resolution and have the effect of smearing of localized, fine structure. The ideal tip would be the one with only one atom at the very end. For such ideal tip about 90 % of the total tunneling current would flow through that atom (as it follows from exponential dependence of the current on the distance). Unfortunately, such geometry is not achievable in the experiments reproducibly. After an electrochemical etching the radius of curvature of the tip is in a limit of 1 nm and one can estimate the resolution of the STM in the following way.

The tip shape can be approximated by a parabolic curve $x^2/2r$, where r is radius of curvature and the tip apex is at $x=0$. The tunneling current flowing from a point $x\neq 0$ is roughly given as (according to Eq. 2.1):

$$I(z+\frac{x^2}{2r}) = C\cdot\exp\left\{-2\kappa(z+\frac{x^2}{2r})\right\} = C\cdot\exp(-2\kappa z)\cdot\exp(-\frac{\kappa x^2}{r}), \qquad 3.1$$

where z is the tip-substrate distance; C and k are constants. The second term of the final equation is a Gaussian function. So, the resolution can be approximated as $\sim (r/\kappa)^{1/2}$ (half width of the Gaussian function). With 1 nm radius of curvature and κ of the order of 1 Å^{-1}, the resolution in the (x,y)-plane will be about 3 Å [Freyland 2001].

Besides these problems an STM image can be strongly distorted by mechanical and acoustical vibrations. Generally, for a good resolution the noise from any source should be less then 0.01 Å in vertical and 0.1 Å in horizontal directions [Bonnell 2001]. The building vibrations lie in the range of 1 – 25 Hz [Welland 1990] and have the same order as a scan rate. The amplitude of these vibrations depends on the distance from the ground, hence the higher floors have the larger amplitudes. Therefore the STM measurements were performed in a lab located in the basement, where the STM-setup always stood on an active vibration damping table. Nevertheless, in spite of all precautions, the measurements in this work were planed to be done late in the evening or during the night, to take advantage of the low vibration level at this time.

The electrochemical environment in combination with the scanning tunneling microscopy poses a new problem. The metal tip immersed into the electrolyte can act as a forth superfluous electrode in addition to the conventional three (reference, counter and working) electrodes. The total current between tip and sample then consists of two components – tunneling current and current attributed to Faradaic charge transfer reaction on the tip. The magnitude of the Faradaic current is defined by the solution concentration, the applied potential, the tip potential and its exposed area [Bard 2000]. Under the conditions of this study this contribution to the total current was always large - order of several hundred milliamperes. Thus it overlapped the tunneling current (1 - 5 nA) and lead to the violation of the feedback control of the tip position or (more frequently) it became simply impossible to perform the STM experiment at all.

Since the Faradaic current is proportional to exposed area of the tip, it can be minimized by properly insulation of the tip (the perfect tip would be completely coated, with only one conducting atom at the end). For experiments at room temperature, the tungsten tips with epoxy coating can be used. The W tips are relatively simple in preparation and normally have very uniform sharp shape of the apex. The coating procedure does not require special equipment and the obtained coating is stable in the room temperature molten salt up to several days. But unfortunately all that is no longer valid as the experiment temperature increases. Already at 50 °C reliability of the tungsten tips coated by epoxy-paint is questionable. It means that another insulation material has to be applied, which would be stable under these conditions. Almost all known materials, used usually in the EC-STM, could not stand either the molten salt by itself or an increase of the ambient temperature. Glass coated tips are (probably) the most stable, but are very difficult to fabricate. In the course of this work a new type of coating procedure was developed by enclosing Pt/Ir tips in a small glass capillary. The way of coating is not trivial and in most cases needs inspirations. Any way, after development of this technique, as a rule, about 9 (in the worst case – 8) of 10 tips showed very low Faradaic current (< 100 pA) and were successfully applied in the EC-STM.

Last but not least, a crucial point in the STM-studies on a nanometer scale is temperature control. Even 0.1 K/hour deviations distort the STM picture considerably taking into account thermal drift and long acquisition time of one picture. If there is no thermal equilibrium inside the electrochemical cell, then it would be problematic to study the same place of interest permanently, since the image would be “walking” under the tip. It is clear, that control of the temperature becomes more difficult with rising the temperature of the measurements. In this case the thermal drift increases and the images following one by one could be so different, that it is even not possible to recognize in which direction the image is “running away”, to adjust the new corrected position of the tip above the substrate.

With all these difficulties it becomes more or less obvious, that the success of the experiment depends on a successive combination of several factors. Only if all of them simultaneously satisfied the necessary requirements the experiment could be performed with some positive result.

3.2 Experimental setup

3.2.1 Electrochemical Variable Temperature Scanning Tunneling Microscope

The STM and STS measurements have been performed with the help of a home-built Electrochemical Variable Temperature Scanning Tunneling Microscope (EC-VT-STM) presented in Fig. 3.1 [Shkurankov 2002]. The Microscope was driven by a Digital Instruments Nanoscope E controller ⟨DI⟩. In order to obtain electrochemical information about the system during STM study the microscope and controller were linked up via a bi-potentiostate, Molecular Imaging Picostat.

The idea underlying this microscope design was to enable the study of highly corrosive and volatile molten salts at elevated temperatures. The final EC-VT-STM, Fig. 3.1, appeared as a result of combination of various requirements to the setup and to the choice of materials. First of all, the different parts of STM had to be stable in the melt or/and to be optimized with respect to the thermal expansions. The latter was important for the measurements at elevated temperatures, where thermal drift has to be minimized. In the following the main parts are only briefly introduced, while the changes and improvements made during this work are highlighted. For details the reader is referred to [Shkurankov 2002].

The EC-VT-STM consists of three main parts:

(i) microscope head,
(ii) STM scanner,
(iii) Electrochemical cell (EC-cell).

The microscope head contains stepping motors (⟨Oriental Motors⟩, Vexta 243M-03AA) and electronics to control the tip movement in vertical and horizontal direction relative to the sample (the feedback), as well as to communicate with a user interface. The stepping motors are placed on the corners of an equilateral triangle and on their axes four round very strong NdFeB magnets ⟨Frank-Magnete⟩ are placed.

The microscope head sits on a steel base plate. In the center of this plate the STM scanner is positioned. The scanner - one of the main parts of every STM - contains a piezo ⟨PI Ceramic⟩, which is a small tube (19 mm outsight diameter and 8 mm height) made from piezo ceramic material ($Pb(Ti,Zr)O_3$) and coated from both sides with a thin metal electrode. The outside part of the piezo tube is divided into four equal quadrants, which are insulated from each other.

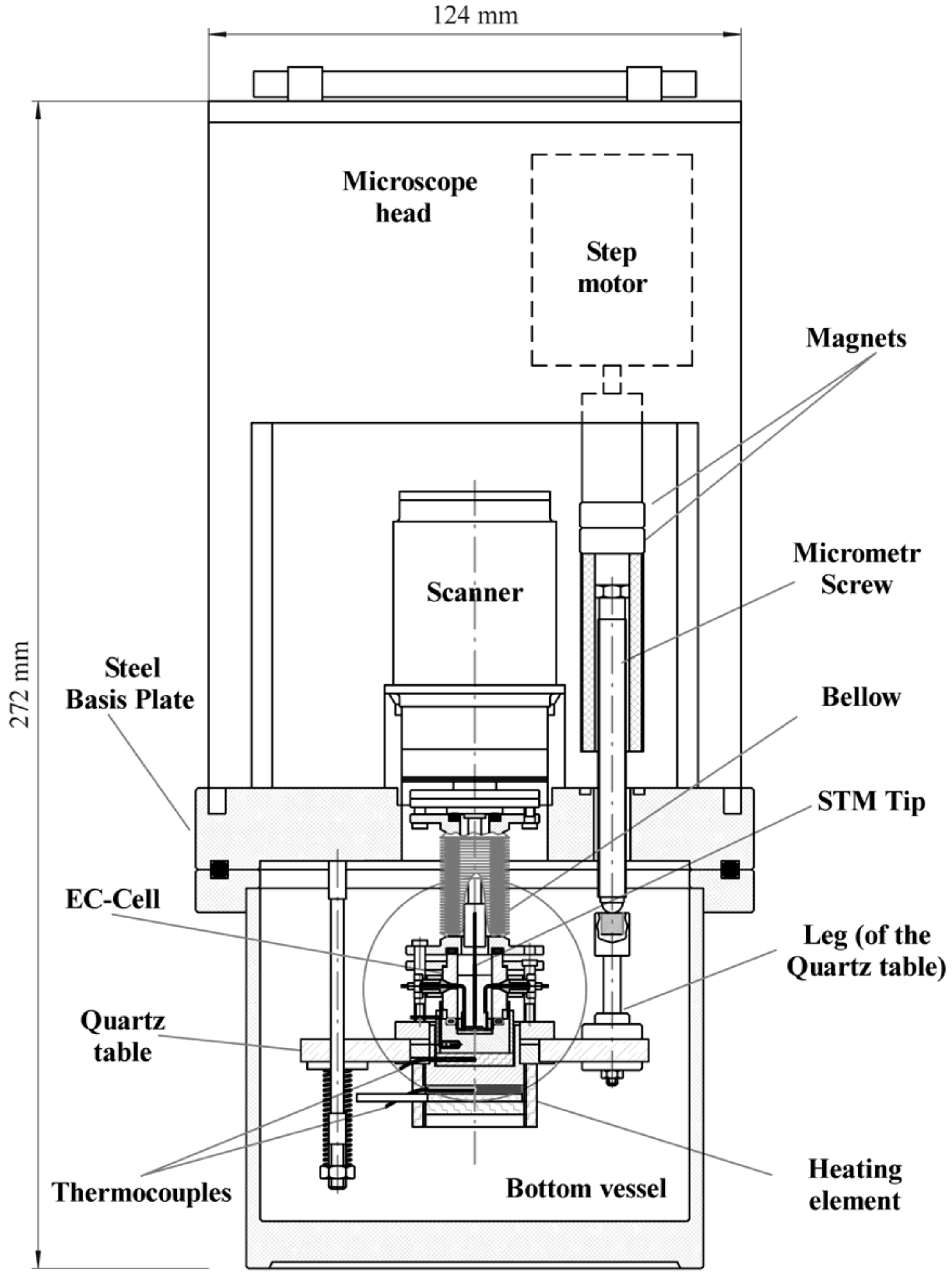
124 mm
272 mm
Microscope head
Step motor
Magnets
Micrometr Screw
Scanner
Steel Basis Plate
Bellow
STM Tip
EC-Cell
Leg (of the Quartz table)
Quartz table
Thermocouples
Bottom vessel
Heating element

Fig. 3.1 *The Electrochemical Variable Temperature Scanning Tunneling Microscope (EC-VT-STM). The electrochemical cell, in the middle of the picture, will be shown in more detail in Fig. 3.2. The heating element is fixed to the bottom of the EC-cell. The scanner (the piezo is inside, not shown) is sealed with the EC-cell with the help of the bellow. The tip-approaching is done through micrometer screws, governed by the stepping motors. The whole setup after assembling is put in a vacuum tight steel chamber (not shown). See also text for further details.*

By applying different voltage to the opposite quadrants and/or to the inner side of the tube, the piezo can be bent, elongated or compressed. (This effect is known as *piezoelectricity*.) The piezo tube is placed insight the stainless steel housing of the scanner. A small flange connected to the piezo holds a tip-holder with a tip. The tip holder (the main part of which is made of molybdenum) is performed so that it can be easily removed and exchanged. The electrochemical cell designed and made during this work will be described in details in the next section. The cell is located on a quartz table (130 mm diameter), at the bottom part of which the BORALECTRIC heating element ⟨Advanced Ceramics⟩ is connected. The heating element is carefully electrically insulated from the electrochemical cell. Two thermocouples (Ni-CrNi, 0.5 mm diameter) are used for temperature control, one, for the heating element, and another for the cell. The first thermocouple is placed inside a copper tablet on top of the heating element and the second one is inside of a corundum plate under the EC-cell. Quartz, as a material of the table, was chosen because of its good electrical insulation properties and extremely low coefficient of thermal expansion. The latter was especially important during heating, because otherwise it would be difficult to keep the sample-tip separation stable.

In the present configuration an approach of the substrate to the STM tip is realized in the following manner. Connected to the stepping motors, long micrometer screws (⟨New Focus Inc⟩, 300 µm/per full rotation) go through the thread insight of the steel basis plate. The screws stay on three legs, joined to the quartz table. Strong flexible connection between screws and the table legs are achieved trough SmCo magnets (which were chosen due to their high temperature of demagnetization). Cylindrical springs put on three steel bars, go through the table and push it up. Those bars serve also as guide rods. Rotation of single screw (correspondingly its retraction) leads to an inclination of the table; subsequent steps of other two motors accomplish the one cycle and provide microscopic approach of the sample to the tip.

The EC-cell can be tightly sealed to the scanner with the help of a flexible stainless steel below ⟨MEWASA⟩. The bellow serves as a protection of the STM (especially steel parts) from violent corrosive mediums and presents a significant difference to conventional STM constructions. Unfortunately the bellow defines a final length of the tip-holder and hence a relatively long tip-holder is required. In this case the sensitivity of the microscope to vibrations increases and in general, the quality of STM images decreases, what in turn hinders analysis of results. Since the melt used in this work was not highly corrosive and not volatile at room temperature and taking into account the above mentioned disadvantages of using bellow, for simplifying and acceleration of experiment's assembly, it was decided to remove this part of the EC-VT-STM.

To protect the molten salt, after assembly of the setup in the argon atmosphere of the glove box, the microscope is placed in a big vacuum tight steel cylinder (not shown in Fig. 3.1), closed under Ar. This additional chamber also helps to decrease the vibrations due to acoustic noise and, with thermal insulating material around it, facilitates better control of a temperature.

3.2.2 Preparation and initial assembling of the electrochemical cell

As was already mentioned, the electrochemical cell (Fig. 3.2), which will be described below, was partly reconstructed and improved in the course of this work. The cell had to sustain highly corrosive and aggressive media at room and elevated temperatures and, at the same time, had to be vacuum-tight. These requirements defined the choice of materials in the contact with the room temperature molten salt: sapphire, molybdenum and Teflon.

The EC-cell mainly consists of two parts – the *sapphire cell* (with reference and counter electrodes) and the *molybdenum cell base* (with the working electrode), Fig. 3.2.

The sapphire cell presents a cylindrical tube with two conical holes on the opposite sides for the counter and reference electrodes. From all insulating materials sapphire stands quite good a mechanical stress (which will be induced later) and is perfectly stable against corrosion at any temperature of the present study. Cleaned initially in the manner described below sapphire was slowly heated up to 1000 °C in a closed corundum crucible. After reaching this temperature (~ 4 hours), it was cooled down to 300 °C. At this temperature, still inside the crucible, the sapphire was transported into the glove box. This annealing acted as a final cleaning of the sapphire and also allowed to reduce mechanical stress induced in the tube during machining and later assembling of the electrodes (from a previous experiment). After the sapphire was cooled down, the counter and reference electrodes were tightly sealed to the sapphire tube insight the glove box.

Before assembling of the electrochemical cell a strict control had to be performed over all possible impurities (see Chapter 3.1). For this propose all parts of the electrochemical cell (Fig. 3.2), which will have a contact with the melt (except of molybdenum components), were cleaned in the following way. After cleaning with ethanol and subsequent rinsing with triple-distilled water they were placed in mixture of H_2O and H_2SO_4 (1:1) for 24 hours. Then everything was boiled for several hours in a diluted solution of hydrogen peroxide and afterwards in triple-distilled water (exchanging water several times).

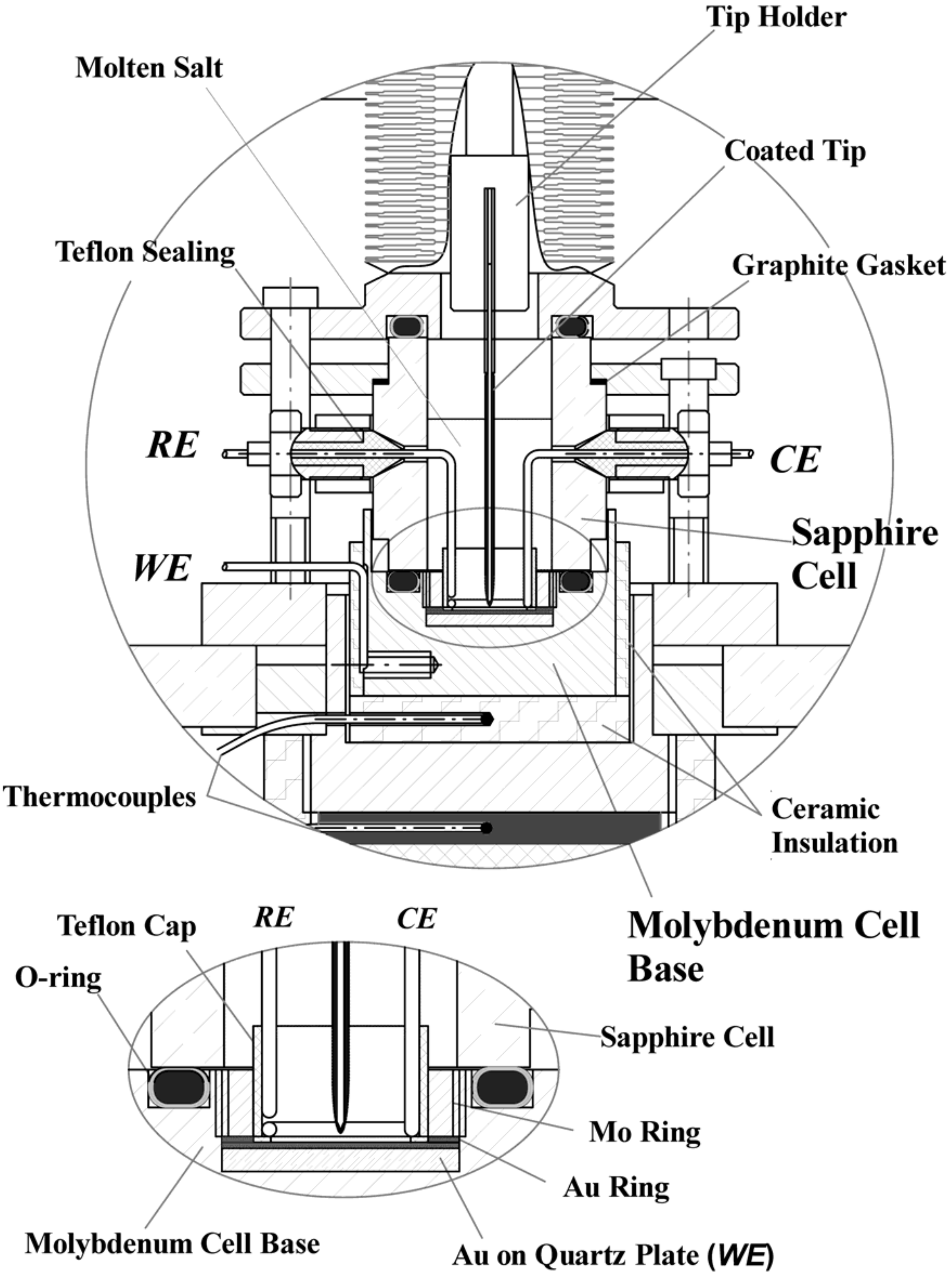
Tip Holder
Molten Salt
Coated Tip
Teflon Sealing
Graphite Gasket
RE
CE
Sapphire Cell
WE
Thermocouples
Ceramic Insulation
Molybdenum Cell Base
Teflon Cap
RE
CE
O-ring
Sapphire Cell
Mo Ring
Au Ring
Molybdenum Cell Base
Au on Quartz Plate (WE)

Fig. 3.2 *The electrochemical cell (EC-cell). The reference, RE, and counter electrodes, CE, are sealed with the sapphire tube. The tip-holder holds the tip immersed into the solution inside the EC-cell. The heating element (shown not in full) is connected to the molybdenum cell base.* ***In the bottom of the figure*** *the inner part of the cell is shown in more detail: the coated tip is brought very close to the Au film, which is pressed by the Mo-ring; the Teflon cap served as electrical insulation of RE and CE from the Mo-ring. (See text.)*

After that, these parts were dried at 120 °C in a desiccator, usually more than one day. The same procedure was applied to all auxiliary instruments (such as pipettes etc.) and glass containers required during the later storage of the melt.

The electrodes were produced from Zn wire (〈Alfa〉, 99.9985 %, 0.5 mm diameter) and no special cleaning procedure was applied to them. The wire was just kept in the glove box "as delivered" in order to avoid passivation and adsorption of water.

The sealing of the counter and reference electrodes with the sapphire tube was achieved in the following way (see Fig. 3.2): a conical gasket from Teflon, with one electrode put through it, was pressed into the hole of the sapphire tube and fixed there by a metal collar. Leak detector test showed nearly UHV quality of such sealing. To ensure a big enough area of the counter electrode, it was preliminary bent in form of a ring (~ 8 mm insight diameter). The length of the reference electrode should be long enough, so that the electrode could be positioned later as closed as possible to the working electrode, but on the other hand between both should be no contact. After sealing of the electrodes the sapphire cell was left in the glove box until the final assembling of the whole STM.

The molybdenum cell base serves as the bottom of the EC-cell, where a working electrode is placed. The preparatory manipulations with the working electrode (7 mm in diameter Au film deposited on quartz) require special description and are given in the next section. The Mo-cell and a Mo-screw-ring (to fix the Au sample inside) were annealed under vacuum in an induction furnace at 1100-1200 °C for half an hour before each experiment. It was done to get rid of the Mo-oxides, which are volatile at such temperatures, and other impurities. After cooling down to room temperature, the Mo-parts were transported under atmosphere of Ar into the glove box.

The preparation and assembling of the electrochemical cell (Fig. 3.2) is relative laborious. Therefore all chronoamperometric and some STM measurements at room temperature were performed with the help of the conventional electrochemical cell. It consisted of a Teflon cell, which was pressed *via* a silicon O-ring coated by Teflon 〈Alwin Hoefert〉 to the working electrode. The working electrode in that case was again the Au film deposited on a quartz plate, but different in a size -12×12 mm 〈Arrandee〉. Before experiment this electrode was treated as it will be described in Section 3.2.3. The counter and reference electrodes were Zn wires (〈Alfa〉, 99.9985 %, 0.5 mm diameter) placed inside the Teflon cell. For more details of the cell construction the reader is referred to [Zell 2002].

3.2.3 Au substrate

The working electrode consisted of a thin gold film (200-300 nm thickness) deposited on a quartz plate ⟨Arrandee⟩. Under the Au film a very thin (~ 2 nm) layer of chromium is deposited, which improves adhesion of the gold to the quartz. The working electrode was first cleaned with triple-distilled water and dried on air. Then it was settled in a quartz tube and carefully annealed at ~ 600 °C under vacuum in a high frequency oven. This initial annealing paved the way for good quality of the final Au substrate and the procedure was normally done over several hours. Then the gold sample was slowly cooled down to room temperature under the same vacuum conditions. Afterwards the quartz tube was filled with the argon and closed with a vacuum tight valve. In such conditions the Au substrate was left until assembling of the electrochemical cell.

Directly before the STM experiment the Au substrate was taken from the atmosphere of argon and annealed under hydrogen flame: the sample is placed on clean Ceran plate and by moving it horizontally the gold was uniformly flame-annealed from the top in to a reddish colour, corresponding to 600-700 °C, for about 2-3 min. During such a thermal treatment one had to remember, that too high temperature would decrease the quality of the final gold terraces, as well as very low temperature could be insufficient for appearance of them. After annealing the electrode was cooled down to room temperature in a nitrogen stream for about 15 min. Only then the substrate was transported into the glove box, where it was immediately used for assembling of the EC-cell. If all described above manipulations were done properly, one can expect the gold film with (111) orientation which exhibits large flat terraces with similar quality as for a gold single crystal.

3.2.4 Molten salt

In all measurements the Lewis acidic $AlCl_3$/BMIC (1-butyl-3-methyl-imidazolium chloride) molten salt with the molar composition of the components of 58:42 was used. This salt is extremely hydroscopic and already a small amount of water leads to a hydrolysis of aluminum chloride. The degradation of the melt can be caused also by the presence of other impurities, which have negative influence on the final STM image. To minimize these negative effects all preparations were done in the inert atmosphere of the glove box (O_2 and H_2O < 2 ppm). Moreover all instruments and containers required for the molten salt preparation were cleaned with great care in the way described in Section 3.2.2.

The preparation of the room temperature molten salt includes four steps: cleaning of $AlCl_3$, synthesis of BMIC, mixing them together in order to obtain the room temperature molten salt and finally the dissolving of Zn(II) into the melt.

• Cleaning of $AlCl_3$

The commercially bought aluminum chloride (〈Fluka〉, puriss.p.a. > 99%) had normally yellowish color, what is the sign of the presence of such undesirable components as water, oxides and $FeCl_3$. To get rid of all of them the following sublimation procedure was performed. The aluminum chloride together with 2 % of high purity NaCl and some pieces (shavings) of pure aluminum (〈Alfa〉, 99.999 %) was placed in a quartz ampoule, which was evacuated and vacuum sealed. The mixture was then slowly heated up to 200 °C. The heating was done in a vertical spiral Au mirror oven over several hours. At this temperature the mixture was melted and after 6 hours the ampoule was moved slightly out of the furnace. In such a way the temperature was locally decreased to 150 °C and the aluminum chloride began to crystallize from a liquid phase as big transparent crystals inside the upper part of the quartz tube. Continuously moving the tube up, the whole $AlCl_3$ was allowed to condensate.

Normally after this procedure the aluminum chloride was free from $FeCl_3$, but there still could be some rest of water and oxides. To improve the quality of the $AlCl_3$ crystals further, the whole sublimation was done as a rule three times. The freshly sublimated aluminum chloride was transported into the glove box. Unfortunately, in the course of time, even under the argon atmosphere of the glove box, this chemical agent picks up water. To avoid this problem freshly sublimated $AlCl_3$ was used for each melt preparation.

• The synthesis of 1-bythil-3-methyl-imidazolium chloride (BMIC)

The synthesis of 1-bythyl-3-methyl-imidazolium chloride was performed in a closed glass container inside a simple glove box, without circulation and filter systems, filled with argon.

Initial products for the synthesis of BMIC were 1-methylimidazole (〈Merck〉, > 99 %) and 1-chlorobutane (〈Merck〉, > 95 %). For cleaning propose 1-chlorobutane was boiled first for several hours over P_2O_5, distilled at 78 °C, then placed in a tightly sealed flask and transported into the glove box. 1-methylimidazole was distilled under vacuum at 198 °C and after that left under the atmosphere of Ar in a protective glass container.

To synthesize BMIC, 1-methylimidazole was slowly added to 1-chlorobutane under argon. This mixture was stirred at 50 °C under the same atmosphere for two weeks. During that time the mixture formed an oily product, whose subsequent recrystallization was initiated by addition of several small pieces of BMIC. The whole crystallization of BMIC took approximately one hour and transparent crystals were the final product. These crystals were filtered out and recrystalized two times from acetonitrile (〈Merck〉, > 99.8 %). The resulting white crystals of BMIC were dried under vacuum for 14 days and only after that used for the further preparation of the room temperature molten salt.

- **The Electrolyte**

The electrolyte was produced by slow mixing together $AlCl_3$ and BMIC in proportional composition of 58:42. Immediately after the addition of the first several crystals of the aluminum chloride to the BMIC the mixture began to melt. This melting was a result of a spontaneous exothermal reaction. Therefore mixing had to be done slowly to avoid local overheating, what could lead to a decomposition of the whole melt in general and the organic component in particular. During 2-3 hours $AlCl_3$ and BMIC were mixed up and then left under stirring over next 14 - 16 hours. After that time aluminum chloride was completely dissolved and the molten salt was ready for the next step – dissolution of Zn in it.

- **Dissolution of Zn into the melt**

The introduction of Zn(II) into the melt was done by the controlled-potential coulometric anodization of a zinc wire. This method was found to be the most appropriate and precise [Pitner 1996, 1997], [Zell 2002] in comparison with the common way of preparation of such solutions by dissolving the metal salt (ZnCl).

During electrodissolution of Zn the following setup was used, which is schematically shown in Fig. 3.3. The working and reference electrode were Zn wires (〈Alfa〉, 99.99 %, 0.25 mm diameter) placed in an individual glass container (right, Fig. 3.3). A disposed in the second container (left, Fig. 3.3) aluminum wire (〈Alfa〉, 99.99 %, 0.25 mm diameter) served as the counter electrode. After installation of the electrodes, each container was filled with approximately 4 ml of the melt and then connected with each other through the melt bridge.

Zinc was dissolved in the melt by the controlled-potential oxidation of the working electrode at a potential of 750 mV applied between the counter and reference electrodes. The control of the passing charge was done with the help of the coulometer 〈Bank〉. The concentration of zinc, $C_{Zn(II)}$, (or necessary amount of the charge, q) in the solution of volume V was determined in accordance with the basic equation of any coulometric method [Bard 2001]:

$$q = zFVC_{Zn(II)}. \qquad 3.2$$

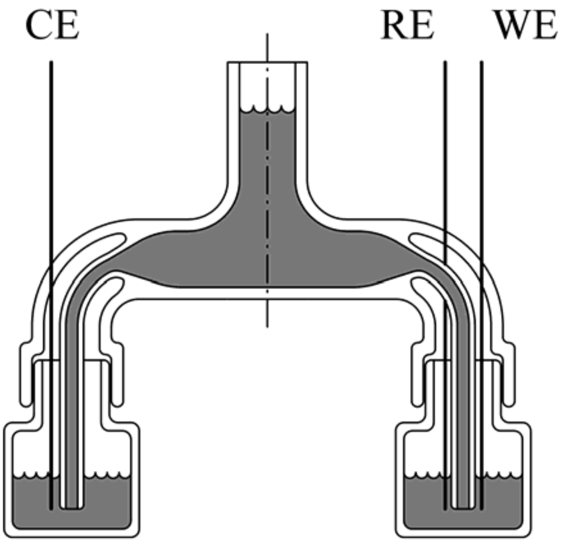

Fig. 3.3 *The electrodissolution of Zn(II). The counter electrode, CE, is Al wire, the reference and working electrode, RE and WE, are Zn wires. The working electrode is bent as a spiral to insure big enough electrode surface. The glass containers are connected though the melt bridge.*

All EC-STM experiments described in this work were performed with the concentration of zinc of 1 $\mathrm{mmol \cdot l^{-1}}$. At higher concentrations (for example 5 $\mathrm{mmol \cdot l^{-1}}$) the deposition process was too fast to be monitored by *in-situ* STM-measurements. The solution of Zn(II) had just the same transparent color as the initial molten salt.

3.2.5 Preparation of STM tips

During STM measurements two kinds of tips and correspondingly two kinds of insulating coatings were used: tungsten tips with epoxy-paint coating and Pt/Ir tips covered by glass. As was already mentioned the first type of the tips can be successfully used at room temperature, whereas the glass coated Pt/Ir tips proved to be better at elevated temperatures.

- **The Pt/Ir tips**

The STM tip were prepared from Pt/Ir wire (〈Advent〉, 90 %-Pt/10 %-Ir, 0.25 mm diameter) by etching it in an unstirred solution of 4 mol sodium cyanide. The wire was cut into pieces of approximately 30 mm length, cleaned with ethanol and then dried. From each cut piece two STM tips could be produced. The piece of wire was passed through a 5 mm diameter ring of Pt wire (〈Advent〉, 0.25 mm diameter). It was important to position the Pt/Ir wire in the center of the Pt ring; otherwise the future tip would have an asymmetrical form of the apex. Then the lamella of the NaCN solution was created on the Pt ring. The thickness of the lamella was easily adjusted by removing some part of the solution with absorbent paper. An dc voltage of 3 V was applied between the ring and the wire. The wire immersed into the solution of NaCN was etched until its bottom part fell down in a glass holder. The etching was stopped and both parts – upper and lower – could be employed for a STM experiment. For neutralization the tips were first rinsed in $Na_2S_2O_3$ solution and then washed with water. The freshly prepared clean and dried tips were used for the next step of tip preparation – coating.

For coating of Pt/Ir tips a soda/lime glass ⟨Hilgenberg⟩ was chosen because its thermal expansion coefficient (9.5×10^{-6}/K) is very close to that of Pt/Ir, which was estimated to be 8.7×10^{-6}/K by assuming that the coefficient depends linearly on the composition of Ir in the alloy [Heben 1988] with the values for pure Pt and Ir 8.9×10^{-6}/K and 6.5×10^{-6}/K correspondingly [CRC 1991]. As a result, a good wetting between wire and glass can be achieved, what ensures homogeneous insulation of the tip.

To prepare the glass for coating of the tip, a glass capillary (0.95 mm outside and 0.41 mm inside diameter) was cut in approx 14 mm long pieces. Each piece was cleaned with ethanol, dried on air and carefully put on the tip from the blunt (not etched) side until the tip apex was staying inside the capillary. For the melting of glass a special designed coating apparatus was used. The tip with the glass capillary on it was fixed horizontally and slowly moved trough a Pt wire (⟨Advent⟩, 0.25 mm diameter), which was bent in a 1 cm long and 5 mm in diameter spiral. By applying a voltage to the spiral it was heated up and the glass capillary began to melt uniformly covering the tip. This stage was accomplished successfully if the tip was completely covered by glass and there were no cracks or bubbles between the metal wire and the glass, Fig. 3.4a.

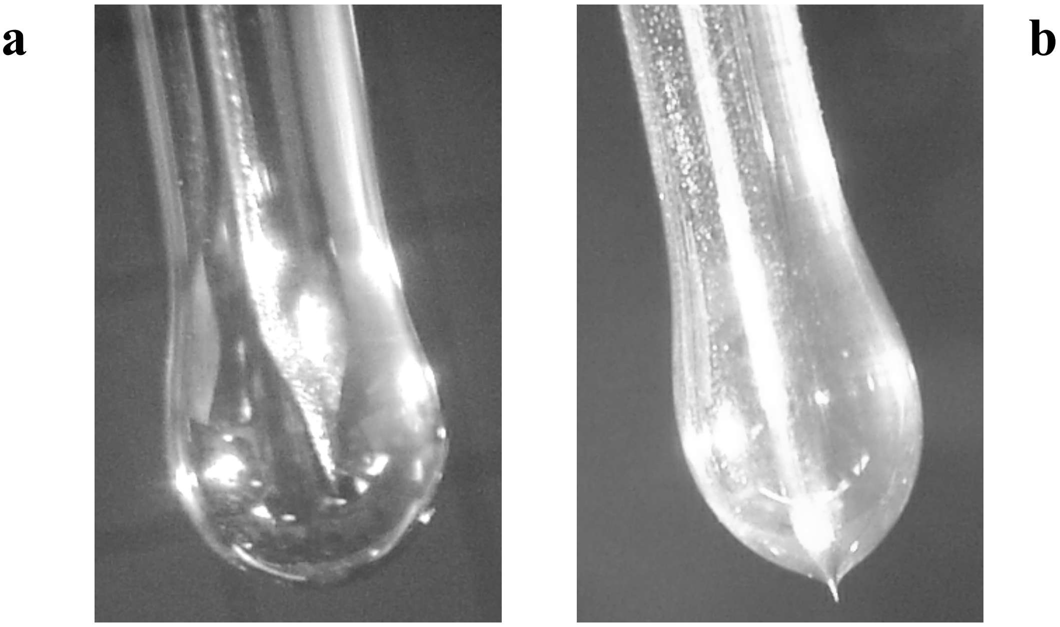

Fig. 3.4 *The insulation of the Pt/Ir tip;* ***a)*** *the first stage, the tip is uniformly completely coated by the glass;* ***b)*** *the second stage, the only very end of the tip is open.*

This was checked under an optical microscope and only then the next stage of insulation was begun.

Next, the very end of the tip had to be opened. This was done by heating the tip in vertical position in an oven at the temperature of 780 °C for more than one hour. At some point the glass started to flow down and the apex of the tip came to the light. Normally after 80 min the tip was taken from the oven and checked with an optical microscope for rough estimation of the size of the open part. If the very end of the tip looked out, Fig. 3.4b, then the size was examined more precisely. If not - the tip was put once again into the oven for the same or a bit shorter time. The size or area of the open part plays a crucial role in EC-STM and should be as small as possible (see Chapter 3.1). The final suitability of the tip was tested under electrochemical conditions in aqueous solution of $CuSO_4$ by measuring the offset current. The tip was used further only if the detected offset current was lower than 100 pA.

- **The W tips**

To produce the STM tips from tungsten wire (〈Alfa〉, >99.98, 0.25 mm) a similar etching procedure as in the case of Pt/Ir tips was used. The only difference was that the etching solution was 2 mol NaOH and dc voltage around 3 V was applied between the piece of W wire (anode) and the Pt-ring (cathode).

For the insulation the freshly prepared tips were first completely coated with an epoxy-paint (〈BASF〉, ETL ZQ 84-3225). For this propose the tip was immersed into the epoxy-paint and 90 V dc voltages were applied between it and a Pt plate, which served as the counter electrode for the time period of 5 minutes. Subsequent opening of the very end of the coated tip was performed by stepwise heating. The tip was transported in an oven and left there for 2 h at 100 °C first and finally 10 min at 250 °C. During this time the paint slowly flew down and the tip apex became just a little open, so it was enough to perform an electrochemical STM experiment.

3.3 Experimental procedure

3.3.1 Assembling of the EC-VT- STM

Directly before each experiment the gold substrate was annealed under the hydrogen flame (see Section 3.2.3) and transported into the glove box. Then it was fixed inside the molybdenum cell base with the help of the Mo-ring. To achieve better electrical contact between the Mo-ring and the gold film on the quartz plate, a thin ring from polycrystalline gold was put between them. Otherwise the film was simply scratched under the Mo-ring leaving a bare quartz surface. Afterwards the sapphire cell with the two electrodes (Section 3.2.2) and Mo cell (with the working electrode) were tightly sealed together *via* a silicon O-ring coated by Teflon ⟨Alwin Hoefert⟩. This type of O-ring was selected after a corrosion test in the molten salt (at T≅120 °C). Assembling "fine mechanical" setup in the glove box, it was difficult to prevent an electrical contact between the counter electrode and Mo-ring, so a small thin-wall Teflon cap was placed on the top of the Mo-ring, Fig. 3.2.

The quartz table with the heating element and the complete EC-cell was fastened to the bottom part of the microscope head (see Fig. 3.1). For measurements at elevated temperature two thermocouples were then inserted unto the cupper and corundum tablets – to control the temperature of the heating element and of the EC-cell, respectively.

The EC-cell was filled with approximately of 0.5 ml of the melt. The scanner, with a freshly prepared STM tip, was carefully (paying attention to the delicate tip) inserted into the holder in the middle of the steel base plate. The microscope head was settled onto the base plate and the whole construction was put onto the bottom of the microscope vessel. All cables and connections were plugged and the microscope was placed inside the steel vacuum tight chamber. The STM setup should not touch the walls of the chamber; otherwise acoustical waves could be transmitted and additional vibrations would be induced during measurements. The chamber was attached to the bottom of the glove box and could be tightly sealed inside the glove box. From time to time (before assembling of the experiment) the chamber was baked out at 120 °C in order to get rid of water adsorbed on its inner walls.

The chamber with the microscope inside was carefully transported to the STM laboratory in the basement, where it was put on a special table (active vibration damping) ⟨IDE⟩ and connected to the Nanoscope controller. Some period of time should be given for thermal stabilization of the whole system, because the temperatures in the glove box room and in the STM lab have always small difference. In addition the microscope by itself produces heat when the stepping motors run. Therefore the first tip approach was done normally after 2...4 hours.

3.3.2 STM measurements

At the beginning of the experiment the tip should be brought to the substrate close enough so that the tunneling current could flow between them. The typical tunneling current is 1÷5 nA and the tip-sample distance in this case is in the range of 0.5 - 50 Å. During approach one step of the stepping motors corresponds to a reduction of the distance between the tip and substrate by 350 nm. After each step the piezo extended in *z*-directions and the presence of the tunneling current was checked. The maximal extension of the piezo could be 500 nm and if the tunneling current was detected, the approach stopped. If the tunneling current was absent, the piezo retracted and the next step of stepping motor was done and so on until the tunneling condition was established.

After reaching the tunneling conditions, for measurements at room temperature the place of interest was found. First, a maximum surface area (2.5×2.5 μm^2) was scanned. At the same time the potential applied to the working electrode was chosen so, that no deposition/dissolution processes should occur. For experiments described in the present work the initial potential was always 750 mV *vs*. Zn/Zn(II). The area of interest for a detailed study lay in the range of from 100×100 to 150×150 nm^2.

For the measurements at elevated temperature, after reaching the tunneling conditions, the tip was withdrawn by 15-20 µm and heating of the sample was started. The control over temperature was done with the help of a PID controller ⟨Eurotherm⟩ and a dc power supply. Experimentally it was found out, that a heating rate of 10÷15 K/h gave better results for the thermal stability of the STM images. In any case, before scanning of the substrate additional hours were waited for the complete thermal stabilization. After this time the scanning was started, but if thermal drift was still too high, the process was stopped and continued later, when the temperature was more stable.

3.3.3 Electrochemical measurements

The cyclic voltammogram (CV) was recorded using the Molecular Imaging Picostat, which was connected to the Nanoscope Controller. In principle, the STM pictures and electrochemical information could be obtained simultaneously. However, the cyclic voltammogram was normally taken at the end of the measurements without recording STM pictures. This was because of the following reason. It was known (and observed experimentally in this work), that gold and zinc form an alloy. It means recording CV at the beginning of the experiment might modify and age the gold surface, what could lead finally to inconsistent results.

To extract the electrochemical data from a Nanoscope file the program “VOLT” [Vinzelberg 1997] was used.

The chronoamperometric measurements were performed as a rule in a separate experiment inside the glove box using the conventional electrochemical cell with the help of an EG&G potentiostate.

3.3.4 STS measurements

The spectroscopic information was obtained on the DI Nanoscope controller in the Current Imaging Tunneling Spectroscopy (CITS) mode. In this mode a tunneling spectrum is taken on each specified location while scanning and hence local electronic structure can be directly imaged in the current measurements.

During measurement of tunneling spectra at each CITS point the feedback was deactivated for a few hundred microseconds to maintain the position of the tip constant. Meanwhile the tunneling voltage was linearly ramped between two given values and the corresponding current was recorded. At the end, the voltage was switched to the initial value, the feedback was activated again and the tip continued to scan the studied surface until the next CITS point was reached. If current-voltage curves were recorded relatively fast (~200 μs) in comparison with the scan rate (~5 Hz), then the STS spectrum could be measured on 32×32 points while scanning the substrate.

The major advantage of this technique is that all spectroscopic information could be obtained simultaneously. So, the problem associated with sample-drift instabilities was minimized.

3.4 Data evaluation and errors

The evaluation of STM results was performed mostly with the help of the DI Nanoscope 4.23 software. The surface coverage of zinc islands on the gold surface, however, was measured in the following way. First, all islands were marked manually with the help of some image program (Paint Shop Pro). The STM image was converted in a two-color picture with size of 512×512 pixels, where the islands were painted black and the rest (uncovered gold surface) was painted white. Afterwards the image was digitalized: the value "1" was given to the black regions of the image and "0" to the white. The image in this format could be evaluated with the help of the FORTRAN program "CGRAPH" [Koslowski 2001], which counted the number of each sort of pixels ("1" and "0"). The systematic error due to the transfer of the STM image into "black and white" picture was estimated to be ~10 % of the surface coverage. In graphs "coverage *vs.* time" (Chapter 5.4) the error bars represent average errors of several evaluated images.

In any case, there was always a certain contribution to the error connected with the tip influence on the STM image. For example, the tip scans some feature of the surface, which is approximately of the same size as the tip apex. The corresponding image reveals the surface feature somewhat smaller or larger, than it is in reality, Fig. 3.4a. Generally a blunt tip smears edges of the surface terraces and makes the image fuzzy. The lack of the control over the tip geometry can also lead to the so-called double image, when the same surface place is imaged twice (or even more times), Fig. 3.4b.

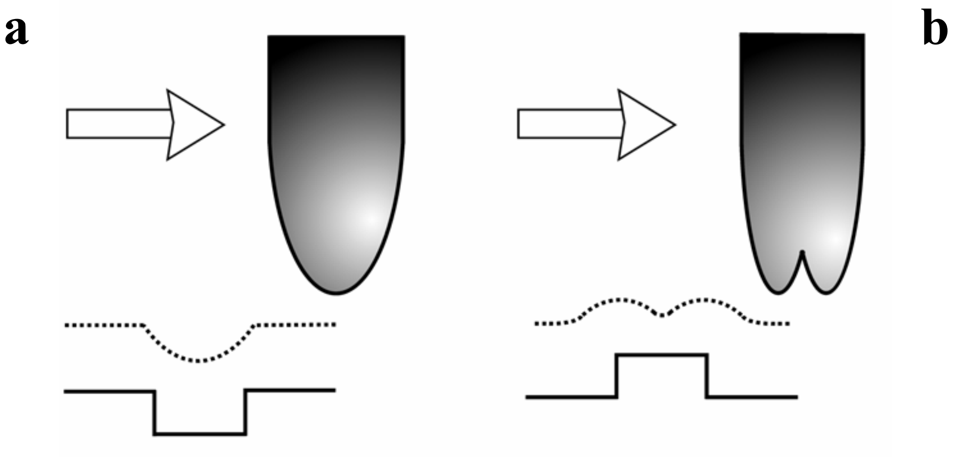

Fig. 3.4 *Influence of the tip geometry on the STM image;* ***a)*** *the blunt tip images the feature of the surface smaller than its original size, also with degraded edges,* ***b)*** *the tip has two apexes where each of them make its own contribution into the tunneling and the final STM image does not reveal the real topography.*

The contribution of the thermal drift has to be taken into account as well, since it is responsible for the distorted images, when a round cluster, for instance, is depicted as an oblong oval. All these factors were considered and corresponding corrections were applied. Careful selection of the images during the evaluation was always performed. The measurement of island heights (Chapter 5.1) was made in such way, that *z*-profile was taken in several directions and average value with an error was calculated.

The error of the Zn(II) concentration in the room temperature molten salt during the controlled-potential coulometric anodization was due to an inaccuracy of the determination of the solution volume (see Eq. 3.2). In principle, the error of the charge measurements has to be also considered, but it so small that it could be neglected. The error of the solution volume was ± 0.1 ml, what corresponded to concentration error of $\pm 0.1 \cdot 10^{-3}$ $\mathrm{mol \cdot l^{-1}}$.

The stability of Molecular Imaging Picostat is about ± 0.02 V. That corresponds to ± 0.8 μA of current measurement during recording of cyclic voltammetry. This value was used during evaluation of cyclic voltammetry data.

As in the case of STM measurements the influence of the tip geometry on the obtained STS spectra had to be taken into account as well. For example if the tip has two micro tips, then both of them would participate in the tunneling and as it was shown by Klitsner et al. [Klitsner 1990] one micro tip could dominate over the second one. The main problem in this case is that it is not possible to distinguish which of the two micro tips is conducting the tunneling current and the obtained spectrum cannot be interpreted. Generally, tip-related artifacts can be excluded comparing the results of several independent experiments with the variety of tips and samples. At the same time within a single measurement the electronic structure of the tip is known to be at least constant.

The value of the effective tunneling barrier between the tip and sample in this work was determined by evaluation of several STS spectra and average error bars are shown in a graph (Chapter 4.5), corresponding to the noise of current measurements and uncertainty in the fit procedure.

4. Results

In this chapter the electrodeposition at room temperature and at 50 °C and electrodissolution at room temperature of Zn from $AlCl_3$/BMIC molten salt on Au(111) are described. At the beginning the system was examined with the help of cyclic voltammetry at both temperatures. It has been found that in the UPD range three reductions peaks can be distinguished. In order to receive further information the current-transient curves were additionally obtained.

In the following section of this chapter the STM results are presented. The deposition of Zn occurs according to the layer-by-layer mode. In the UPD range zinc forms three successive layers on gold. The layer-by-layer mechanism extends in the OPD range as well, where the number of layers can not be estimated, since the growth is much faster than in the UPD. At the same time in the OPD range aluminum codeposition takes place, the beginning of which is marked by a *Moiré pattern* formation. Dissolution of Zn shows that surface alloying of zinc with gold occurs. This conclusion is strongly supported by STM images. Alloying is present already during deposition of the first zinc monolayer. Due to experimental difficulties, the deposition at 50 °C is only briefly treated in the subsequent section.

In the last section of the chapter the results of STS measurements are summarized. They show almost no variation in the tunneling barrier value, ϕ, in the UPD range, except of the formation of the first monolayer, whereas in the OPD range a clear reduction of ϕ can be recognized.

4.1 Cyclic voltammetry

Prior to the *in-situ* STM study, the electrodeposition and electrodissolution of Zn were characterized by the cyclic voltammetric measurements. Typical cyclic voltammograms at room temperature and at 50 °C on Au(111) electrode in a solution of 1 mmol/l Zn(II) in $AlCl_3$/BMIC (58:42) are shown in Fig. 4.1a and b, respectively. Both cyclic voltammograms were received with the same cell geometry and sweep rate.

The positive limit of the cyclic voltammograms is 1250 mV *vs*. Zn(II)/Zn reference electrode, since the Au bulk oxidation begins at 1350 mV. If this potential is applied, the solution turns red and the gold film is removed from the quartz plate. Reducing the potential the first feature met in the CV is the redox couple B/B', which is clearly seen on both cyclic voltammograms and is located at around 650 mV. In accordance with previous investigations of Ag electrochemical phase formation on Au(111) from the room temperature molten salt [Zell 1999], this peak can be attributed to the gold step oxidation. By means of STM it was possible to observe, that in this case Au atoms were oxidized at the step edges of terraces and then adsorbed on the gold surface. In the course of this work the peak B/B' was always found at the same potential, what demonstrated a good stability of the zinc reference electrode.

Following the potential changes in the negative direction of the CV recorded at room temperature, three reduction waves – C_1, C_2 and C_3 - can be distinguished in the UPD[1] range, Fig. 4.1a. Around 400 mV the current decreases and approximately at 300 mV the first wave C_1 can be seen. The passage from C_1 to C_2 (at 100 mV) is very smooth, whereas between C_2 and the last peak in this potential range C_3 (at 10 mV) there is a clear increase in the current. A similar structure was recorded during the measurements at 50 °C, Fig. 4.1b – all peaks preserve their positions. However, it can be noticed, that peak C_3, for example, becomes broader and is almost smeared out in comparison to the CV at room temperature. Although the temperature difference between these cyclic voltammograms is not big, changes in the current magnitude are pronounced. For instance, the current difference between two reduction peaks D and C_2 is 3-4 times bigger at 50 °C in comparison to room temperature. If the deposition is diffusion controlled, this increase of the current is consistent with the enhancement of a diffusion coefficient with temperature.

The appearance of three UPD peaks is very surprising; normally in this potential range one can expect one or maximum two peaks.

---

[1] UPD (underpotential deposition) – a potential range which lies positive of the Nernst potential, which per definition is 0 mV.

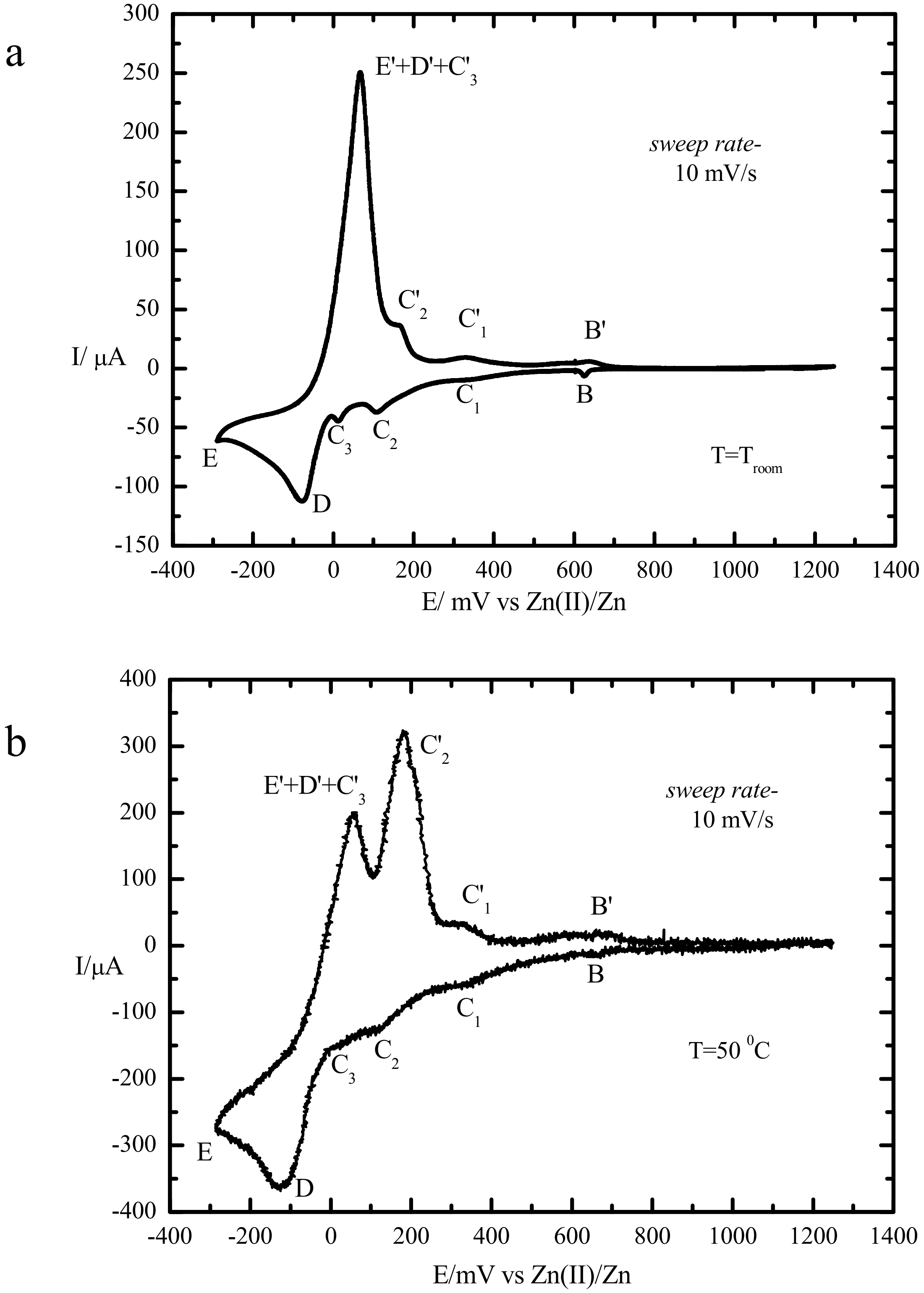

Fig. 4.1 *The cyclic voltammogram of Zn on Au (111) in $AlCl_3$/BMIC(58:42);* ***a)*** *at room temperature and* ***b)*** *at 50 °C. The electrode area in both cases is 0.4 cm^2. (I-scale is different.)*

The underpotential deposition of Zn has been intensively studied in the last decades, however mostly in aqueous solutions and correspondingly with different deposition mechanisms, e.g. 2 UPD peaks. For example, in the work of Chu et al., the Zn deposition from alkaline zincate solutions was investigated on various substrates using conventional methods, above all cyclic voltammetry and potential pulse methods [Chu 1981]. The results showed that in the case of Au and Cu approximately one monolayer of Zn is formed prior to the bulk deposition. In addition to a single UPD peak the authors reported also about an evidence of the alloy formation in both cases. Similar results (including an alloy formation) were obtained by Despic and Pavlovic in the study of the initial stage of the zinc deposition from zinc sulphate solution on gold and platinum electrodes [Despic 1982]. An extended research in this field was performed on polycrystalline Pt in solutions with various pH by Aramata and coworkers [Aramata 1992]. The results obtained by cyclic voltammetry were interpreted with the help of one UPD peak of zinc. However, in the later work of Aramata already two UPD peaks of Zn on Pt after the addition of some amount of Br^--ions into the 0.1M KH_2PO_4 solution were found [Aramata 1996].

Zn electrodeposition from molten salts is very rare. Several investigations were performed in $ZnCl_2$/EMIC (1-methyl-3-ethylimidazolium chloride) melt [Lin 2001], [Chen 2001]. It was shown that during electrodeposition of Zn-Co and Zn-Te alloys underpotential deposition of zinc on cobalt and on tellurium occurred. Pitner and Hussey performed electrodeposition of zinc at 40 °C from a molten salt similar to this work, which was produced by mixing $AlCl_3$ and EMIC [Pitner 1997]. During the underpotential deposition of Zn on a Au polycrystalline electrode the authors discovered the presence of two UPD peaks on cyclic voltammograms. These peaks were referred to the formation of Zn-Au surface alloys – cubic γ_1-$AuZn_3$ and tetragonal α-Au_3Zn.

So, as was already mentioned, the appearance of 3 peaks in the present study is unusual and not fully understood. This aspect will be touched in the discussion.

After the Nernst potential the current drops on each CV and peak D at -80 mV is discriminated. This process is attributed to the zinc overpotential deposition (OPD[2]). In the negative range CVs are limited to - 300 mV. At this potential, peak E, Al bulk deposition sets in. At both temperatures the stripping peak, attributed to an oxidation of the three reduction waves E, D and C_3, is situated at ~65 mV. The following waves C_2' and C_1' do not change their position with the temperature as well. They are located at 170 mV and at 350 mV, respectively. Although both cyclic voltammograms do not exhibit a significant difference in peaks position, there is a clear change during the back sweep in the current magnitude. It is interesting, that at room temperature the peak E'+ D'+ C_3' is greater than C_2', whereas at 50 °C the situation is reverse.

---

[2] OPD (overpotential deposition) – a potential range which lies negative of the Nernst potential.

In order to investigate the system behavior in more details, the cyclic voltammetric measurements at room temperature were performed over a wide range of sweep rates. The results are shown in Fig. 4.2.

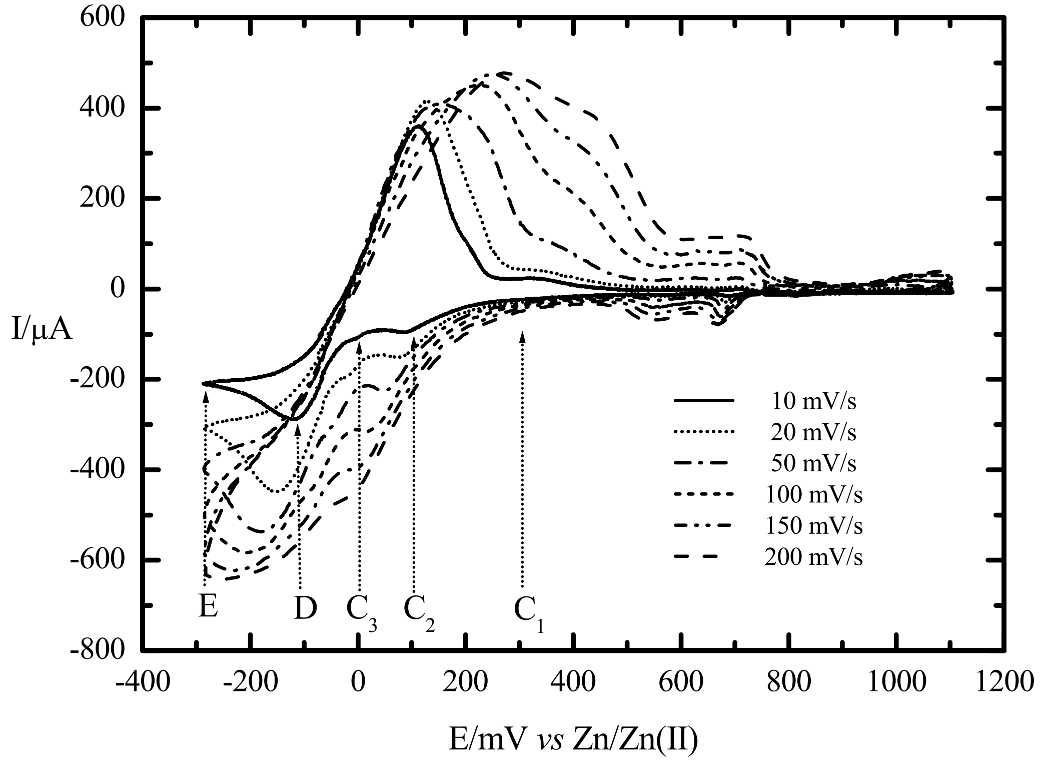

Fig. 4.2 *The cyclic voltammograms of Zn on Au (111) in $AlCl_3$/BMIC (58:42) at room temperature taken at different scan rates. The cathodic peak currents are shown with arrows in consistency with the CV at the slowest sweep rate.*

As can be seen, the magnitude of the current increases with an increase of the scan rate. This is due to the fact, that for the faster sweep rates the relaxation time will be less and this leads to the higher concentration gradient at the surface, which is in turn proportional to the current [Southampton 1990]. Decreasing the time, required for recording of one cyclic voltammogram, the peak C_1 becomes almost absent, Fig. 4.2. At slow sweep rates (10 and 20 mV/s) it is still possible to distinguish between two neighbor peaks – C_2 and C_3, while for the higher sweep rates they merged into a single peak. It can be noticed, that this resulting peak (C_2 +C_3) is dependent on a sweep rate and is shifted in the negative direction with an increase of the sweep rates. In contrast to that, the peak D is difficult to analyze. At higher sweep rates several redox waves overlapped and this complicates the determination of peak current values for one single process and interpretation of the observed results quantitatively. Besides that, as it is shown below, this peak does not correspond to the pure Zn deposition alone, but to Zn-Al codeposition (see Chapter 4.3).

For a purely reversible process, the electron transfer is much faster than mass transport and the position of a peak current should be independent on sweep rates. But it is also quite common that the reversibility of a system is dependent on the sweep rate, and at higher sweep rates the system becomes irreversible. In other words the time scale of the experiment will not be sufficient long to allow the electron transfer to maintain the equilibrium at the electrode surface. Such a situation seems to be the case for underpotential deposition of Zn (waves C_1, C_2 and C_3 on CV, Fig. 4.1), which - as reported by Pitner and Hussey [Pitner 1997] and proved by STM measurements of this work - involves surface alloying with gold.

4.2 Chronoamperometric study of Zn electrodeposition

For the further study of kinetics of the Zn electrodeposition a chronopotentiometry experiment has been performed. The experiment was based on recording current-transient curves in a wide range of electrode potentials *E*. At the beginning the sample was held several minutes at 750 mV *vs*. Zn/Zn(II) reference electrode. Then the potential was rapidly switched to a new value of interest. The current-transient curves were taken with steps of 50 mV in a range from 400 to -400 mV. The results of the measurement are shown in Fig. 4.3. In this figure the final potential values lying from 400 to 0 mV belong to the UPD range and from 0 to -400 mV to the OPD range. It is known that the shape of the obtained current-time response on a potential jump depends on the kinetics of various steps involved in the deposition [Southampton 1990]. As it can be seen from Fig. 4.3a, all curves in the UPD range have monotonous character, relatively fast approaching some value close to zero. They all do not show any peaks or waves, except of only one, which reveals the current response on the potential jump from 750 mV to 400 mV. For convenience this curve is shown separately in inset “I” together with the next one belonging to a change of *E* from 750 mV to 350 mV, which looks similar to all others. Two waves can be distinguished at the “400 mV-curve”. All curves from 300 to 150 mV are placed very close to each other and could be attributed to the same process on the surface, whereas the two last curves – at 50 and 0 mV belong probably to two additional separate processes. This can be seen better in inset “II”, which shows the same curves but in the smaller time interval.

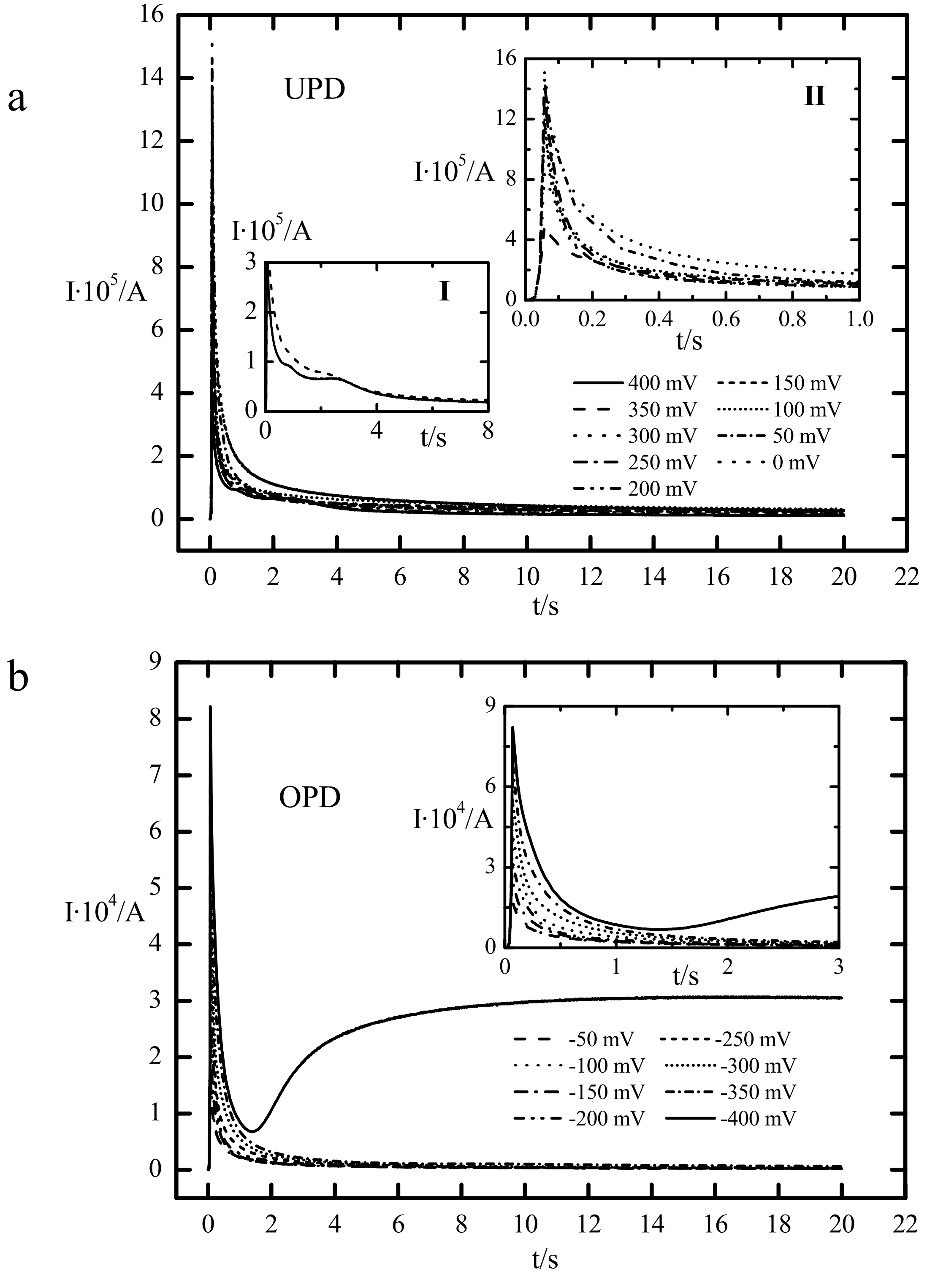

Fig. 4.3 *Results of chronoamperometric measurement. The initial potential was 750 mV, the final values lie in an interval* ***a)*** *from 400 to 0 mV (UPD range) and* ***b)*** *from -50 mV to -400 mV (OPD range) with steps of 50 mV. In the insets the same results but with bigger resolution are shown, see also text for more detail. The area of the electrode is 0.4 cm^2.*

As it was mentioned, at later times the current seems to be independent on the deposition time. It is interesting, that almost the same observation was made by Despic and Pavlovic during the study of Zn on Au electrodeposition from zinc sulphate solution [Despic 1982]. The authors referred this fact to a repetitive 2D layer growth, when smooth deposit reproduces the original surface morphology.

As for the OPD range, Fig. 4.3b, the current transient results represent a similar type of curves in comparison to the UPD range. However, the corresponding current is ~5 times bigger than in the UPD range. Remarkable is the last curve in this set – at -400 mV. First it decreases rapidly within 2 s, but then grows again achieving some constant value of the current. Such behavior is typical for 3D growth with the rate determining step of the lattice incorporation [Southampton 1990].

On a basis of the current-transient measurements it is possible to determine a diffusion coefficient of electroactive species with the help of the Cottrell equation (Eq. 2.15). Thus by presenting experimental results, from Fig. 4.3, as I *vs.* $t^{-1/2}$ the diffusion coefficient can be obtained from the slope. In Fig. 4.4 one typical experimental curve, which was analyzed with the help of the Cottrell equation is shown.

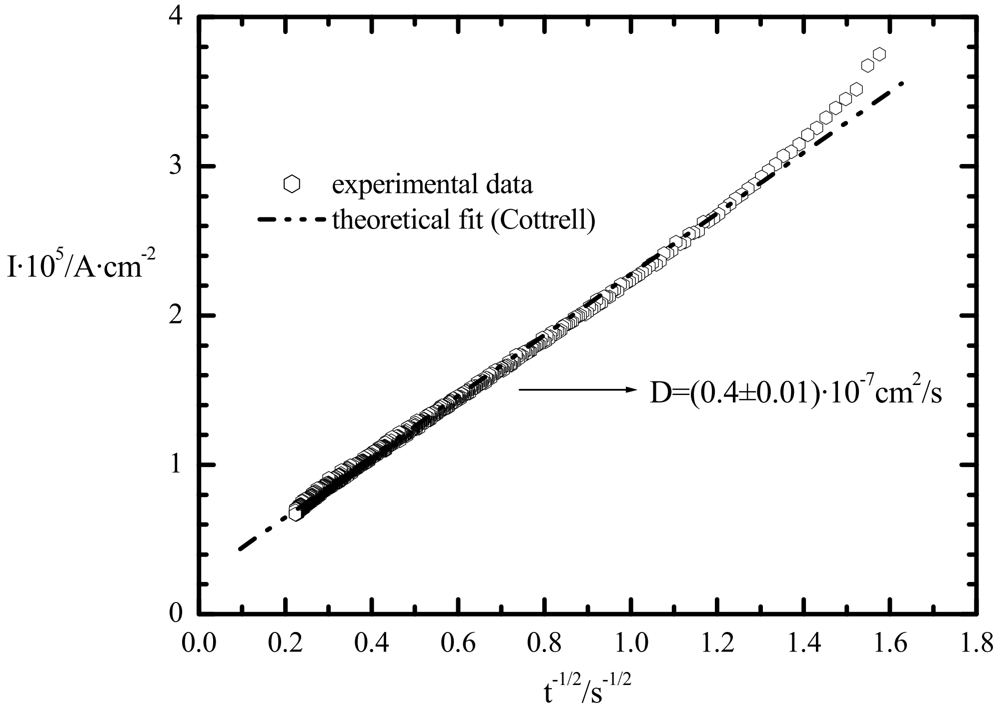

Fig. 4.4 *The plot of I vs.* $\sqrt{t}$ *for the evaluation of the diffusion coefficient by Cottrell equation (Eq. 2.16). The presented curve corresponds to the potential step from 750 to 200 mV, the obtained value for D is* $(0.4\pm 0.01)\cdot 10^{-7}\ cm^2s^{-1}$.

According to the transient curves (see Fig. 4.3) at the initial time the current exhibits very pronounce spike, which is attributed to double layer charging. Hence for the evaluation, the data obtained for the later times only were used. Concerning this particular case, presented in Fig. 4.4, the time of double layers charging was estimated to be about 0.6 s.

The similar analysis was performed for the whole curves obtained during chronoamperometric experiments. The results are shown in Tab. 4.1. More detailed analysis of chronoamperometric curves is given in Chapter 5.3.

Table 4.1 *The diffusion coefficient estimated with the Cottrell equation. For the evaluation results of initial time were excluded. Error is about 10 %.*

E/mV	200	100	50	0	-50	-100	-150	-200	-250	-300
$D\cdot10^7/cm^2s^{-1}$	0.4	0.6	0.6	2.1	2.5	2.2	2.7	4.3	6.6	8.5

As it is seen from the table in the UPD range the diffusion coefficient, which is attributed to the zinc-ion, is approximately $0.5\cdot10^{-7}$ $cm^2\cdot s^{-1}$. In the OPD range *D* increases significantly. It is more then four times bigger in the potential window from 0 to -100 mV and drastically increases to $8.5\cdot10^{-7}$ $cm^2\cdot s^{-1}$ at -300 mV. It necessary to mention, that in accordance with the cyclic voltammetry measurements (Chapter 4.1) and STM results, which are presented below (Chapter 4.3), starting from -100 mV an aluminum codeposition occurs in the studied system. Hence such a strong increase of *D* is related with this effect. The obtained values are in a good agreement with the work of Pitner and Hussey [Pitner 1997]. In their work the diffusion coefficient of zinc was determined in $AlCl_3$ /EMIC molten salt at 40 °C with the help of sample current voltammograms constructed from the results of current-transient experiments and the obtained value is $(6.7\pm0.4)\cdot10^{-7}$ $cm^2\cdot s^{-1}$ [Pitner 1997].

The diffusion coefficient of a metal ions in aqueous solutions should be typically on the order of 10^{-5} $cm^2\cdot s^{-1}$ [Southampton 1990]. For instance, the diffusion coefficient of zinc-ions in KOH solution at 25 °C lays in the range of $(1\div10)\cdot10^{-6}$ $cm^2\cdot s^{-1}$ [McBreen 1978]. In the molten salts, however, *D* is normally smaller. For example, the diffusion coefficient of Ga in the $AlCl_3$/EMIC is $9.12\cdot10^{-7}$ $cm^2\cdot s^{-1}$ [Chen 1999]. For the electrodeposition of lead from the same melt the obtained value is $9.0\cdot10^{-7}$ $cm^2\cdot s^{-1}$ [Hussey 1991]. It is necessary to stress, that the reduction of diffusion coefficient is affected by the absolute viscosity ($D \sim 1/\eta$), which is of several orders of magnitude greater in the molten salts in comparison with that in aqueous solutions, see e.g. [Fannin 1984] and [Atkins 2000].

4.3 STM study of electrochemical phase formation of Zn

In this chapter the results of the Zn electrodeposition obtained by *in-situ* STM are presented. The first part focuses on the deposition process. As the deposition in the underpotential and overpotential ranges has different physical nature, it is of interest to investigate them separately. Dissolution of a deposited metal is of fundamental importance, since it can help to understand better the behavior of the whole system. Hence the second part of Chapter 4.3 is dedicated to this surface process.

4.3.1 Underpotential deposition of Zn

According to the cyclic voltammogram, Fig. 4.1a, in the UPD range three reduction peaks (C_1, C_2 and C_3) can be discriminated. At the beginning the potential window from 750 to 150 mV was examined. This is shown in Fig. 4.5, where the STM images reveal the same surface area, however at different times and potentials.

Formation of the first monolayer. A typical gold surface after flame annealing in contact with the electrolyte is shown in Fig. 4.5a, where the potential of the working electrode[3] is 750 mV. This potential is chosen as a starting value, since in accordance with the CV there are no chemical reactions in this case and one can expect to see a bare gold surface. This potential is also relatively far from the redox couple B/B', Fig. 4.1a, where the step oxidation of the gold surface occurs. Normally after flame annealing (see Section 3.2.3) the gold surface with (111) orientation in the molten salt possesses very broad flat terraces, separated by monoatomically high steps, see Fig. 4.5a. The experimentally measured height of these steps is 2.2 ± 0.3 Å, which is slightly less than value of 2.35 Å expected on the basis of simple geometrical considerations for (111) metal plane (with r_{Au}= 1.44 Å). Such discrepancy can be explained by the influence of tip geometry on the image (see error discussion in Chapter 3.4).

A number of images was recorded at 500 and 400 mV during several independent experiments and no sign of any deposition processes could be found. At 300 mV, Fig. 4.5b, the gold surface is still in its original appearance as at 750 mV. Only few small particles can be spotted in the right bottom part of the image. They could be attributed to the beginning of the zinc deposition, but they also could be some "dirt". Both possibilieties can not be excluded due to unclear chemical composition of these clusters. The potential was kept at this value for further 3 minutes and the surface seemed to be unchanged. After decreasing the potential by 50 mV, the appearance of the picture has a completely different character in comparison with the previous one at 300 mV. Small clusters, clearly seen in this case, are related to the initial stage of the Zn deposition in the underpotential range, Fig. 4.5c. Immediately after changing the potential the STM tip began to scan in the direction shown in the figure as a black arrow. If one scrutinizes the obtained image, it can be noticed, that some areas of the surface at the beginning were left uncovered or that first clusters were so small, that it was not possible to resolve them, Fig. 4.5c - upper part. Detailed analysis of the image shows, that the clusters do not have specific locations – as, for example, along the step edges – and are randomly distributed over the Au terraces. They are roughly equal in size. Exceptions are clusters in the upper part of the image, on one of the brightest terraces (insight an oval in Fig. 4.5c). Interestingly, that 3 minutes later the situation is only slightly changed, Fig. 4.5d. However, the number of clusters grew a little. It is remarkable, that they do not attach to already existing clusters but settle independently somewhere near the old ones.

---

[3] The potentials of the working electrode are given *vs*. Zn/Zn(II) reference electrode.

The development of the islands growth was continuously followed further in the negative direction. In Fig. 4.5e-h several successive images at 200 mV with the time interval of about 3 minutes between them are shown. Comparing the previous image at 250 mV, Fig. 4.5d, with the first image in this set, Fig. 4.5e, one can see that the number of zinc islands increases dramatically after reducing the potential only by 50 mV. The islands occupy now almost the whole free surface leaving just a little space near step edges. During the next 3 min. the islands enlarge relatively fast their size and indicate a strong tendency to merge with each other, Fig. 4.5f. Following this process in the time interval of 12 min an unusual mechanism of the film growth was detected. The islands develop in such a way, that they (and correspondingly uncovered surface – or vacancy - as well) form some highly irregular structure on the gold surface. In Fig. 4.5e-h the evolution of a monolayer zinc film and the subsequent formation of this type of the structure is illustrated on three different places on the surface, marked with the white arrows.

Such features are known in the literature as *wormlike* or *labyrinth structure*. Similar observation was reported recently in the work of Pai et al. [Pai 2001]. The authors performed experiments for the evolution of wormlike monolayer vacancy structure in the systems Cu/Cu(100) and Ag/Ag(100). The monolayer film was produced, however, not by electrodeposition of a metal but with an e^--beam (for Cu) and a thermal (for Ag) evaporation. It is expectable that 2D metal clusters can move by diffusion on a metal substrate in order to find an equilibrium position.

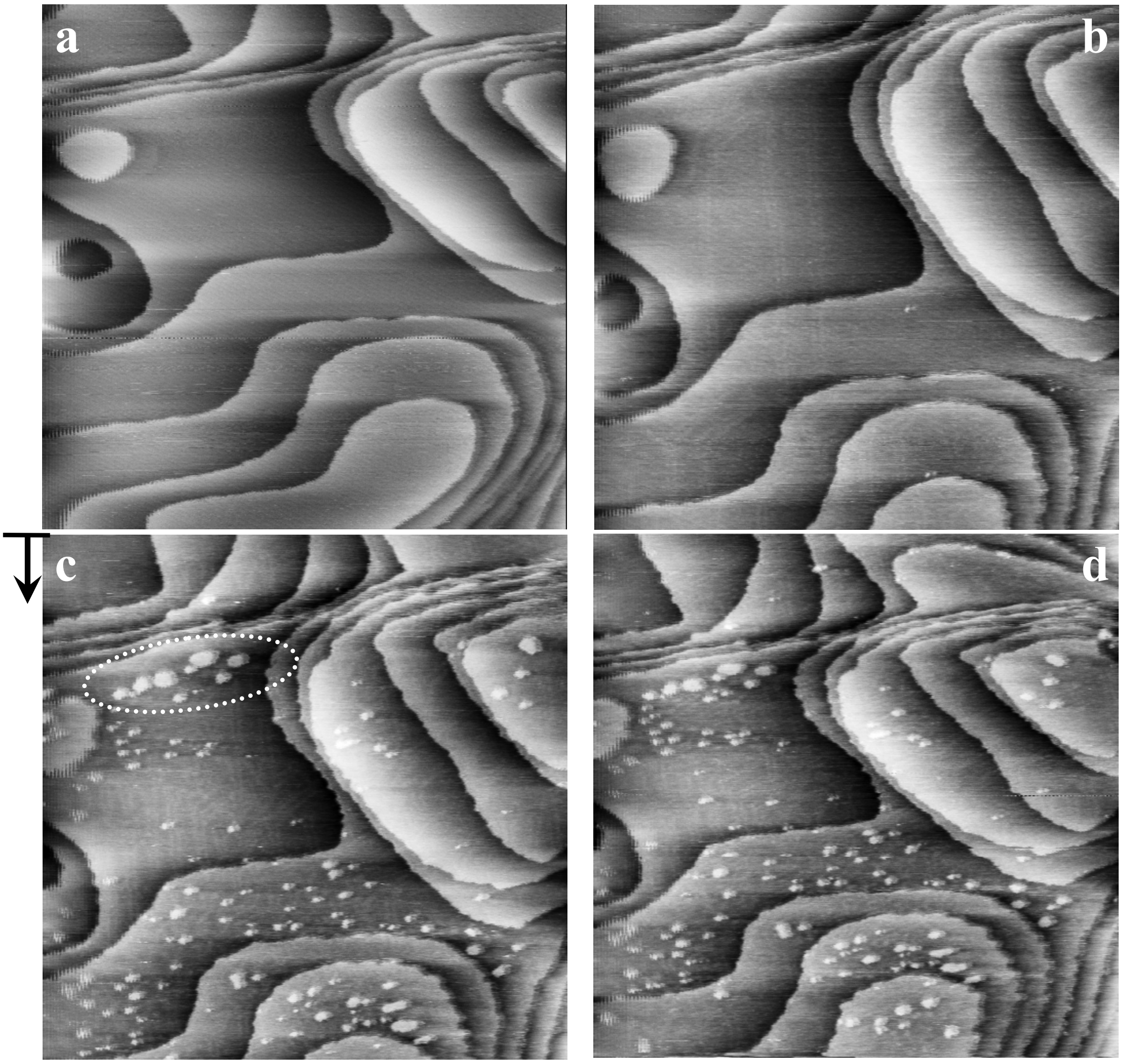

Fig. 4.5 *STM results in the potential window from 750 to 150 mV. Image size is 109×109 nm, scan rate is 3.39 Hz and I_{tun} = 5 nA.*

a)-d) *The initial stage of the first Zn monolayer formation on Au(111) in UPD range. E_{tip} =500 mV for a,b* ***a)*** *E=750 mV. Bare Au substrate, before the beginning of the deposition.* ***b)*** *Unchanged gold surface at E=300 mV.* ***c)*** *E=250 mV. The first few randomly distributed Zn clusters on the Au terraces.* ***d)*** *E=250 mV, 3 min later after the previous image.*

e)-h) *(next pages) The course of 2D growth of Zn at 200 mV. The images were recorded one after another with the time interval of ~ 3 min. E_{tip} =100 mV. The white arrows show some places on the surface, where the formation of the wormlike structure can be followed.*

i)-j) *The final stage of the first monolayer formation. E_{tip} =100 mV* ***i)*** *E=190 mV. The islands cover major part of the gold surface.* ***j)*** *E=160 mV. The growth of the monolayer is almost complete.*

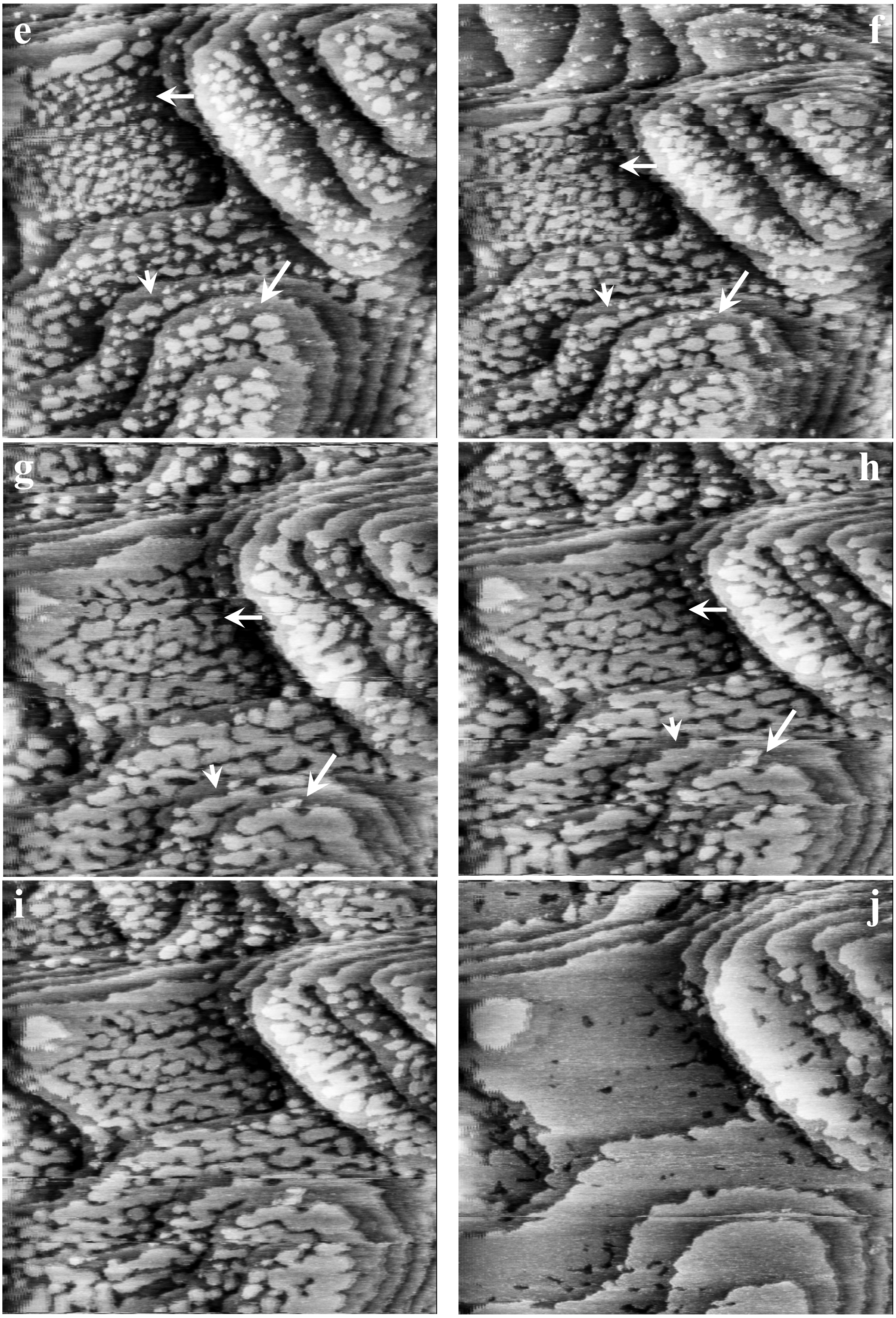

Fig. 4.5 *(sequel) see previous page for description.*

The appearance of the wormlike structure illustrates that periphery diffusion is dominant. It is a very fascinating phenomenon and could be clarified by STM only in recent years [Wen 1994], [Cadilhe 2000], [Schlößer 2000]. Periphery diffusion proposes that mass transport is dominated by diffusion of atoms along the cluster boundary.

With decreasing potential the surface coverage of Au by Zn increases further, Fig. 4.5i. At the same time the wormlike structure can be again recognized; what supposes that the periphery diffusion still dominates in the mass transport of zinc atoms to the already existing clusters. As this STM image was scanned to the end, the potential was switched to a new value - 160 mV and the monolayer of zinc almost completely closed the initial gold terraces leaving only a few uncovered holes, Fig. 4.5j.

Experimentally, on the basis of several independent measurements with different gold samples and tips, it was found that in the potential range between 300 mV and 150 mV (with error of ± 1 mV) zinc forms a very uniform monolayer on gold. In Fig. 4.5j it is possible to see the final stage of such a film formation. The deposited layer reproduces with amazing precision the original shape of the gold terraces. For comparison one can take the image in Fig. 4.5a – at the beginning of the experiment – and the almost final image at 160 mV in Fig. 4.5j. All steps and terraces can be seen again. Changing the potential to 150 mV a completely closed zinc film was obtained within one STM image.

Formation of the second monolayer. In exactly the same way the growth of a second monolayer of zinc on the gold surface was observed and documented. In Fig. 4.6 this process is illustrated particularly.

Immediately after the first monolayer of zinc covered the whole surface several new zinc clusters appeared, Fig. 4.6a. It is interesting, that they occupied the space on one of the biggest terraces between the middle size island (left part of the image) and several closely placed steps (on the right); in the image it is marked with an oval. Approximately at the same place the beginning of the first monolayer growth was detected, see Fig. 4.5c. This image shows that the biggest clusters are located on the discussed place. It means that during the initial stage of the first and second monolayer deposition the clusters prefer to appear at the same location. The potential was left unchanged during the scanning of the next image. As far as this did not bring any visible modification of the amount of the deposited metal, the next potential jump of 20 mV in the negative direction was made, Fig. 4.6b. Several new small zinc clusters are distributed over the terraces, whereas the gold step edges became smoother. As an illustration of this, one specific place is indicated with an arrow in Fig. 4.6a and b. This observation can be assigned to the fact that clusters are distributed not only on the terraces but also across the steps boundary. As it could be expected, with a decrease of the potential towards the equilibrium value the flux of deposited material, and correspondingly the coverage as well, increases, Fig 4.6c. On some intermediate stage the wormlike structure appeared again. As in the case of the first zinc monolayer growth, periphery diffusion is responsible for the mass transport between clusters here also, Fig. 4.6d.

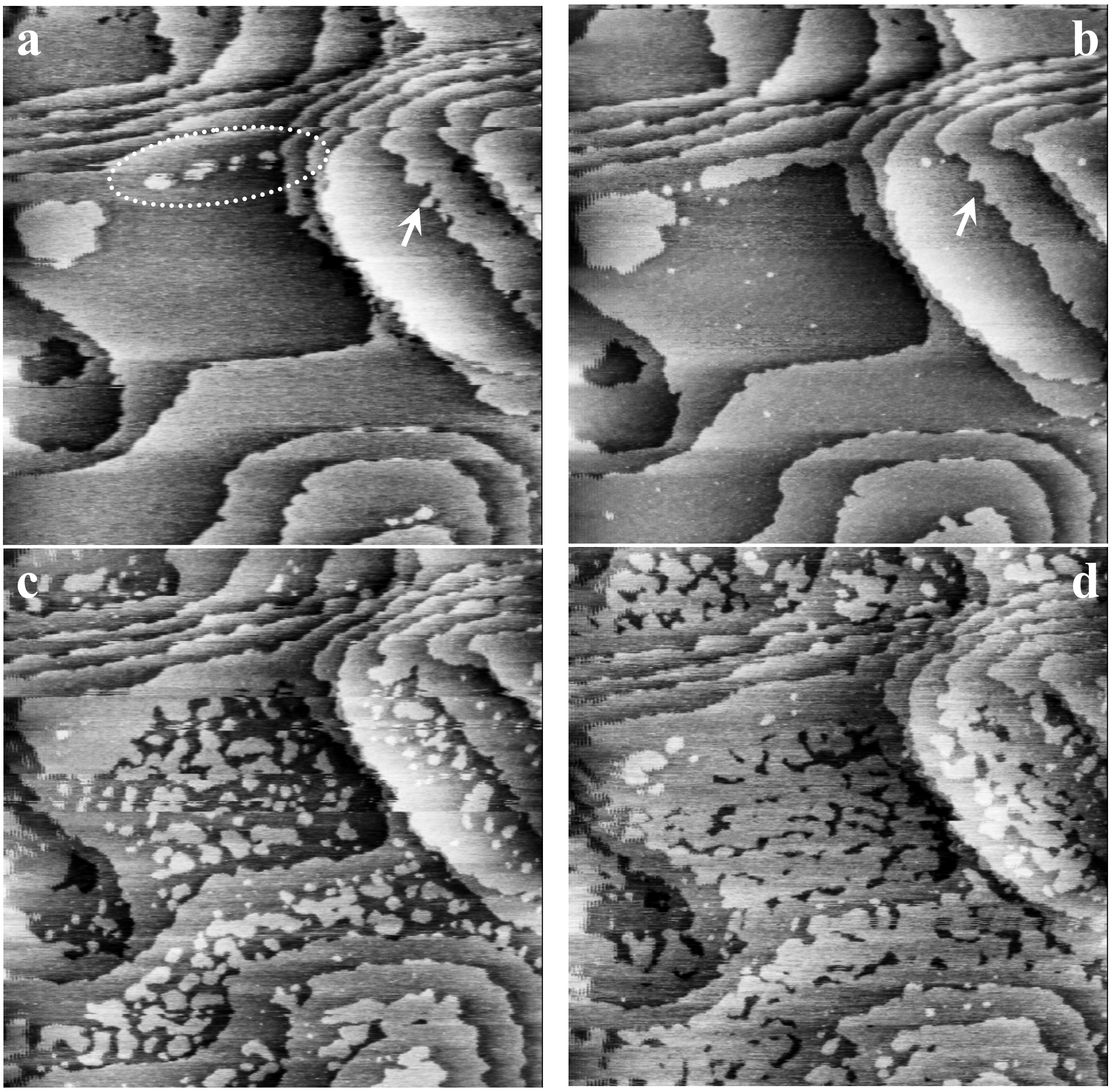

Fig. 4.6 *The second layer formation in the potential window from 150 to 55 mV. The image size is 109×109 nm, scan rate is 3.39 Hz,* I_{tun} *= 5 nA and* E_{tip} *= 50 mV. For the grey scale see the legend of Fig. 4.5.* ***a)*** *E=150 mV. The appearance of the earliest Zn islands on top of the previous monolayer, marked for convenience with an oval.* ***b)*** *E=130 mV. The number of clusters increases, edges of the terraces slightly change their shape, white arrows exemplify this.* ***c)*** *E=100 mV. The islands occupy whole terraces and grow together.* ***d)*** *E=80 mV. Development of the second monolayer on its last stage.*

Changing the potential, the film is forced to grow faster and at 65 mV this process is normally accomplished. The obtained film reveals a very flat surface, the contours reproduce very nicely the original gold terraces. The similar observation was made for the first Zn film already.

Formation of the third monolayer. It was very interesting to see, that in the remaining several tens of milivolts lying in the UPD range, the layer-by-layer zinc growth did not stop, but proceeded further. From 65 to 0 mV with the help of STM one could see the third zinc monolayer formation. This is illustrated in Fig. 4.7.

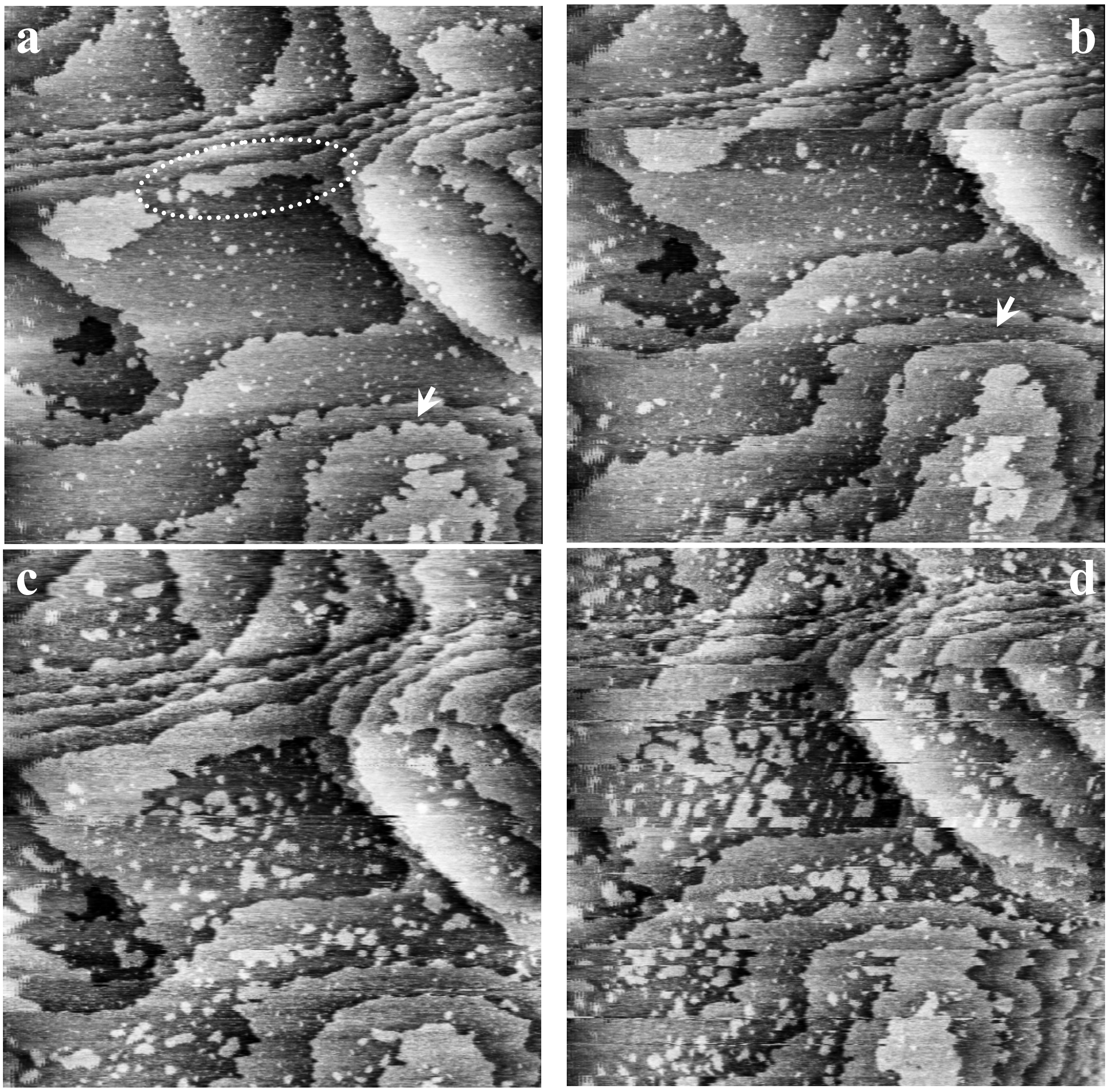

Fig. 4.7 *The growth of the third Zn monolayer in the potential range from 55 to 0 mV;* ***a)*** *E=55 mV,* ***b)*** *E=45 mV,* ***c)*** *E=30 mV,* ***d)*** *E=10 mV. The image size is 109×109 nm, scan rate is 3.39 Hz, I_{tun} = 5 nA and E_{tip} = 10 mV, except of d, where - E_{tip}= 20 mV. For the grey scale see the legend of Fig. 4.5*

As can be seen the scenario is very similar to the evolution of the first two monolayers. At the beginning relatively big clusters are located on the flat terraces; see middle part of the image in Fig. 4.7a (marked with an oval). These clusters form somehow a bridge, binding together two gold surface features. Several small islands are homogeneously distributed on the surface. At the same time the steps edge have a wavy character, which disappears with an increase of the surface coverage. This can be very nicely followed in Fig. 4.7a and b (one example is indicated with an arrow). In the experiments, to which this image sequence belongs to, one could not observe the film growth to the complete final stage due to the some tip problems (first indication of this problem can be already noticed in Fig. 4.7d), but from a variety of experiments this measurement run (Fig. 4.5-7) it is the best as far as quality is concerned and gives a complete overview of the whole UPD of zinc.

To summarize briefly the experimental observation of the underpotential deposition of Zn, it is necessary to mention that the formation of three successive metal monolayers at UPD was monitored in this work for the first time.

4.3.2 Overpotential deposition of Zn

Detailed analysis of Zn deposition in the UPD range showed that Zn has a very strong tendency to build uniformly three successive films on the gold surface. Thus, an interesting question arises - would the growth mechanism change its character going from UPD to OPD range. In order to get an answer on this question the study was continued into OPD range as well, and the results are presented in the following section.

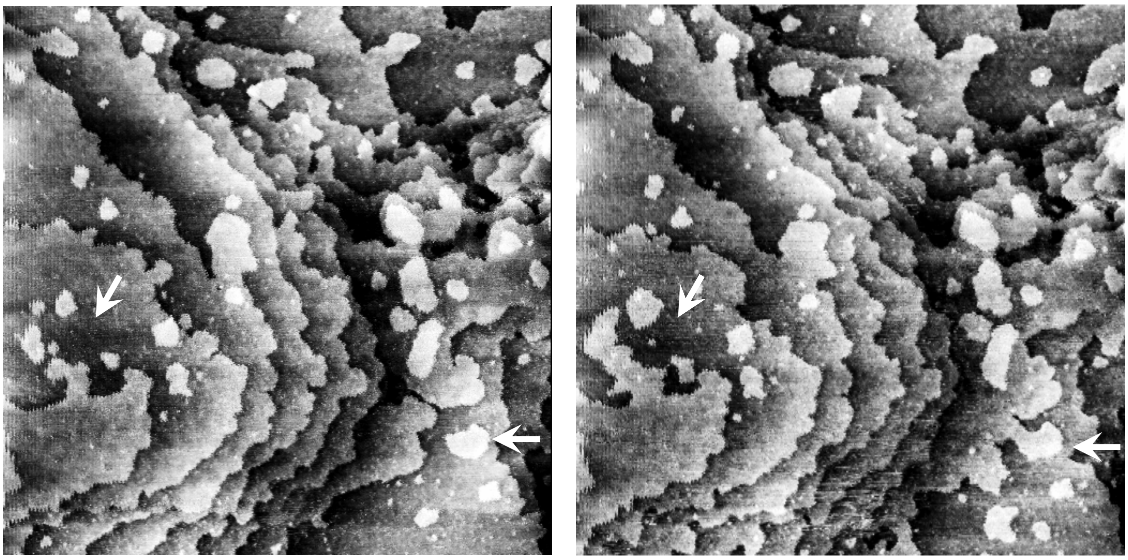

Fig. 4.8 *Layer-by-layer overpotential deposition of Zn on Au, initial stage. E= -10 mV . The time interval between images is ~ 3 min. The image size is 96×96 nm, scan rate is 3.39 Hz,* I_{tun} *=3.5 nA and* E_{tip} *= 50 mV.*

The cyclic voltammetry is marked by very strong drop of the current with the minimum at -80 mV (Fig. 4.1a, peak D). The study of zinc deposition in this potential range shows that the growth mechanism stays unchanged. Zinc indeed continues to form the layers on gold. Beginning of this process is clearly seen in Fig. 4.8. In this experiment the gold surface was first covered with three zinc monolayers by slowly changing the potential from 750 to 0 mV (the experimental procedure is very similar to that described above for UPD of Zn). Then at -10 mV it could be observed that the next few first islands appeared on top of the surface structure. As it is seen from the image, Fig. 4.8a, they have very different sizes, but at the same time the majority has larger structures. 3 minutes were sufficient enough to allow the existing islands to increase significantly. The arrows on both images, Fig. 4.8a and b, mark two places which can be taken as an example of such growth process. The smaller features increase, but also attach themselves to the bigger structures, Fig. 4.8b.

Experimentally it was found, that until -50 mV it is still possible to recognize the original surface morphology of the gold structure. Later, in more negative range, the deposition occurred significantly faster and zinc covered all area without repeating the shape of the gold steps. Besides that, starting from -50 mV one can observe the formation of a superstructure (*Moiré pattern*). At -100 mV – the zinc bulk reduction peak potential – the superstructure covers the whole scanned surface, Fig. 4.9.

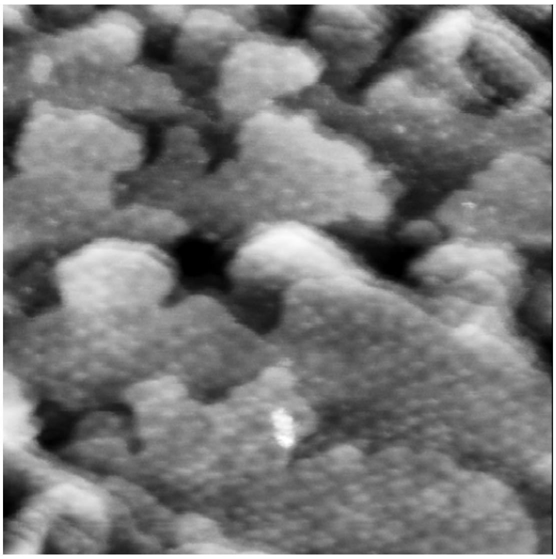

Fig. 4.9 *Moiré pattern occurring at -100 mV. Image size 92×92 nm, scan rate is 3.39 Hz,* I_{tun}*=3.5 nA,* E_{tip}*= 100 mV*

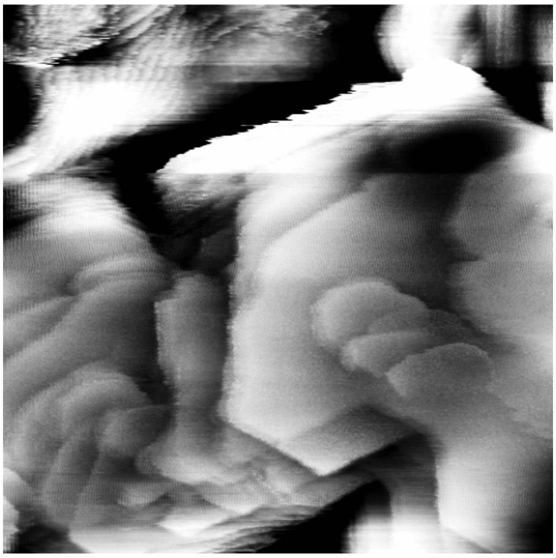

Fig. 4.10 *OPD of Zn. E= -200 mV, Image size 87×87 nm, scan rate is 3.39 Hz,* I_{tun}*=1 nA,* E_{tip}*= 0 mV*

Due to the thermal drift during the measurement this structure looks a little bit distorted, but the hexagonal long-range order of it can be recognized. It was determined that a nearest-neighbor spacing between “white dots” is 22.5±2 Å and a modulation amplitude of 0.9±0.1 Å. The modulation amplitude arises from the misfit between the substrate lattice and the lattice of the deposited metal. Even though this structure appeared on the Zn layers, it would be surprising, if Moiré pattern would incorporate zinc atoms. There is no obvious reason why zinc should suddenly form superstructure at this potential. Comparing the cyclic voltammograms for the pure molten salt [Zell 1999] with that containing zinc (from this work), it is possible to explain appearance of the superstructure as Al underpotential deposition on zinc. In CV of the pure melt on Au (111) a clear evidence of Al UPD, which is indicated as a strong reduction peak near 340 mV vs. Al/Al(III) reference electrode, was found in the work of Zell et al. [Zell 1999]. Taking the gold bulk oxidation as a reference point, both CVs (of Al and of Zn) can be compared directly. Thus it was found that UPD of Al is located at approximately -100 mV vs. Zn/Zn(II) as a reference electrode.

This structure could not be followed in a broader potential window and already at -120 mV it is completely covered by subsequent zinc or zinc aluminum alloy monolayers. These layers grow very fast, so it is almost impossible to monitor their development with STM, since the feedback does not have sufficient time to make reasonable response during surface altering. Some example of a typical surface structure very deep in the OPD range (at -200 mV) is shown in Fig. 4.10 (see also Fig. 4.14b). It was observed that at – 425 mV the character of laminar growth has changed - the deposits form rather clusters, than layers. Such behavior is known to be due to aluminum bulk deposition [Zell 2002], what is also discernible from the cyclic voltammetric measurement of this work.

4.3.3 Dissolution of Zn

In the following section the experimental observations during the zinc dissolution are presented. At the beginning of the measurement on the bare Au substrate, which is shown in Fig. 4.11a, one monolayer of zinc was deposited. This was performed by switching the potential from 750 to 160 mV. Formation of the first layer was followed for a certain time. In the experiment described here, after ~ 21 min an almost complete (except of several very small holes) film was obtained. After that the potential was changed again to its initial value – 750 mV. According to the CV (see Fig. 4.1a), all deposited zinc should be dissolved at such conditions.

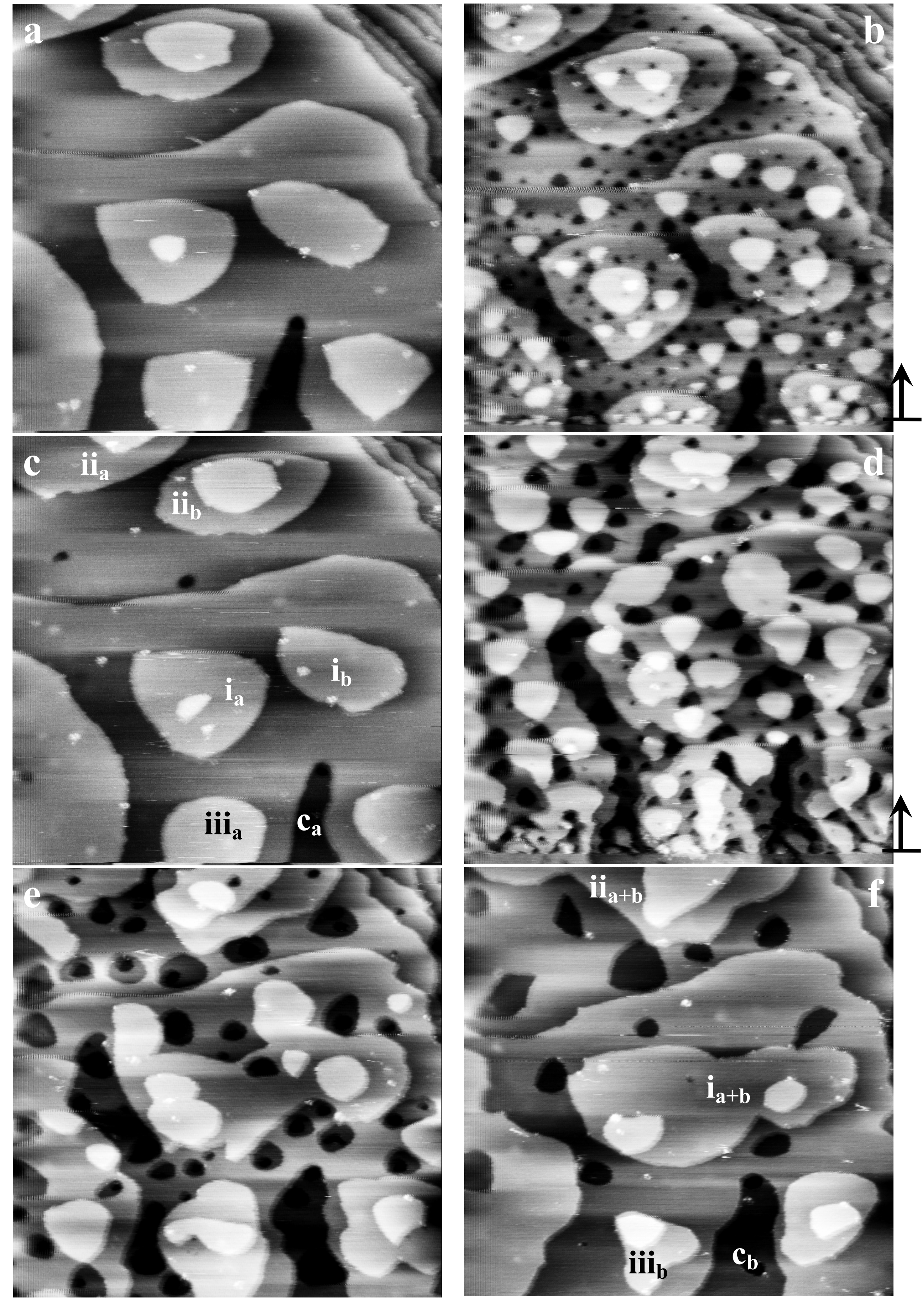
a
b
c
ii$_a$
ii$_b$
i$_a$
i$_b$
iii$_a$
c$_a$
d
e
f
ii$_{a+b}$
i$_{a+b}$
iii$_b$
c$_b$
1 nm
0 nm

Fig. 4.11 *Zn-Au surface alloying. Scan size is 110×110 nm, Scan rate is 3.39 Hz, E=750 mV* ***a)*** *The Au surface before deposition was started.* ***b)*** *The same surface after dissolution of 1ML of Zn.* ***c)*** *56 min later.* ***d)*** *The surface shown in b, but after dissolution of 2 ML of Zn.* ***d,e)*** *5 and 40 min later.*

The STM image obtained in this case is shown in Fig. 4.11b, where the place marked with the black arrow indicates the beginning of the dissolution. In the very bottom of this image the deposited film can still be seen. All subsequent area of this image corresponds to the dissolution process. As it can be noticed, the scanned surface is immediately pierced by a number of holes. These holes are a direct indication of surface alloying which took place during the deposition of zinc on gold. As it can be concluded from the image (see Fig. 4.11b) the holes are distributed on the whole surface without any preferential locations on some specific surface features. Staying at the same potential conditions (750 mV) one can follow the "healing" process as a function of time. In Fig. 4.11c the same surface (as in a) is shown approximately one hour later. Almost all holes disappeared, with exception of only a few in the upper part of the image. It is remarkable, that the initial shape of the terraces can be seen again – compare Fig. 4.11a and c.

As the next step, this surface (Fig. 4.11c) was covered with two monolayers of zinc. The deposition was done continuously reducing the potential from 750 to 90 mV. In this way one can obtain a homogeneous first zinc monolayer and then on top of it - the second one, which is almost completed at 90 mV. Afterwards the dissolution was started again.

The image obtained during the dissolution is depicted in Fig. 4.11d. Again as in the example described above, the place where the potential was changed is indicated with the black arrow. At a first glance one can notice a stronger modification of the surface, than after dissolution of one Zn monolayer only. If in the latter case the initial shape of the gold terraces can be recognized (Fig. 4.11b), in the former case it is almost impossible (Fig. 4.11d). After 5 minutes at the potential of 750 mV the surface changes drastically, Fig. 4.11e. It is difficult to see from the single picture presented here, but possible to follow in the experimental sequence of images, that there is a certain tendency in the surface modification. Smaller holes disappear, whereas the bigger ones require longer time for that, and the shape of the gold surface becomes slowly visible. 40 minutes later there is still a significant amount of defects, Fig.4.11f. Besides this, the original shapes of terraces are altered, what was almost invisible after dissolution of one zinc monolayer – Fig. 4.11c. Comparing the figure 4.11c with 4.11f one can see, that two middle size gold islands in the center of the image (indicated as i_a and i_b in Fig. 4.11c) have merged in the latter case (i_{a+b} in Fig. 4.11f). The same is true for the two islands in the upper part of Fig. 4.11c and f (ii_a and ii_b produce ii_{a+b}). A long trench in the bottom of the images 4.11c and 4.11f (c_a and c_b) seems to become broader. At the same time one small terrace on the left side of the channel shrank (iii_a and iii_b).

Analyzing the observations described above it seems that there is some dependence of the degree of surface modification during surface alloying on the number of the deposited layers. In order to prove this the STM images were taken on the dissolution of bulk zinc deposits (OPD). Some selection of images obtained in this case is displayed in Fig. 4.12. For clarity, the first image in the figure shows the bare Au surface at the beginning of the experiment, before the deposition was started. Reducing the potential in the negative direction till -50 mV this gold surface was covered by several zinc monolayers. As it was concluded from the results of STM measurements in the OPD range at this potential at least 4 subsequent zinc layers have to be expected (Section 4.3.2). In the very bottom of Fig. 4.12b these layers can be seen. The following area represents beginning of dissolution at 750 mV (indicated with black arrow).

The obtained image has clearly different character in comparison with the images recorded at the initial stage of dissolution of one and two monolayers of zinc, Fig. 4.11b and d. First, there are definitely more holes. Second, islands are relatively small in size. Their origin is not always clear: they can be both rest of zinc deposits and gold islands. 5 minutes later a very strong disordered gold substrate can be seen in Fig. 4.12c. Such a structure indicates nonequilibrium state of the surface and the corresponding "healing" process was followed in the time interval of ~ 1 hour. All observations can be summarized as follows. Smaller holes vanish, at the same time it can be noticed that some of them generate bigger ones. For instance, it can be viewed in the middle of the images marked with a circle, Fig. 4.12c-f. Two small holes go towards each other and merge. Then this new hole leaves the terrace and moves to the right, Fig. 4.12d. After that it integrates into an assembly of several defects on the low terrace. As it can be seen from the following STM image, Fig. 4.12e, during the next 40 minutes the number of holes decreases and only two holes insight the marked area can be detected: smaller and bigger ones. The latter is a result of merge several holes (see image c and d). The former, smaller, will not be attached to the bigger one, but will go in the opposite to it direction toward another defect, even though the migration way is longer (this process is not shown here). Finally, it will completely disappear. The trace of this hole still can be seen in Fig. 4.12f, after ~100 minutes from the beginning of dissolution (follow arrow from the image e to f). The changes in shape of the terraces can be followed as well. Two very small islands to the left (inside the circle) are dissolved in 18 minutes. Dissolution of them happened somewhere between two images recorded after 8 and 10 min. Thus it might be possible that one of these islands was consumed for the healing of holes, described above, which are located close by. More examples can be found in the presented images.

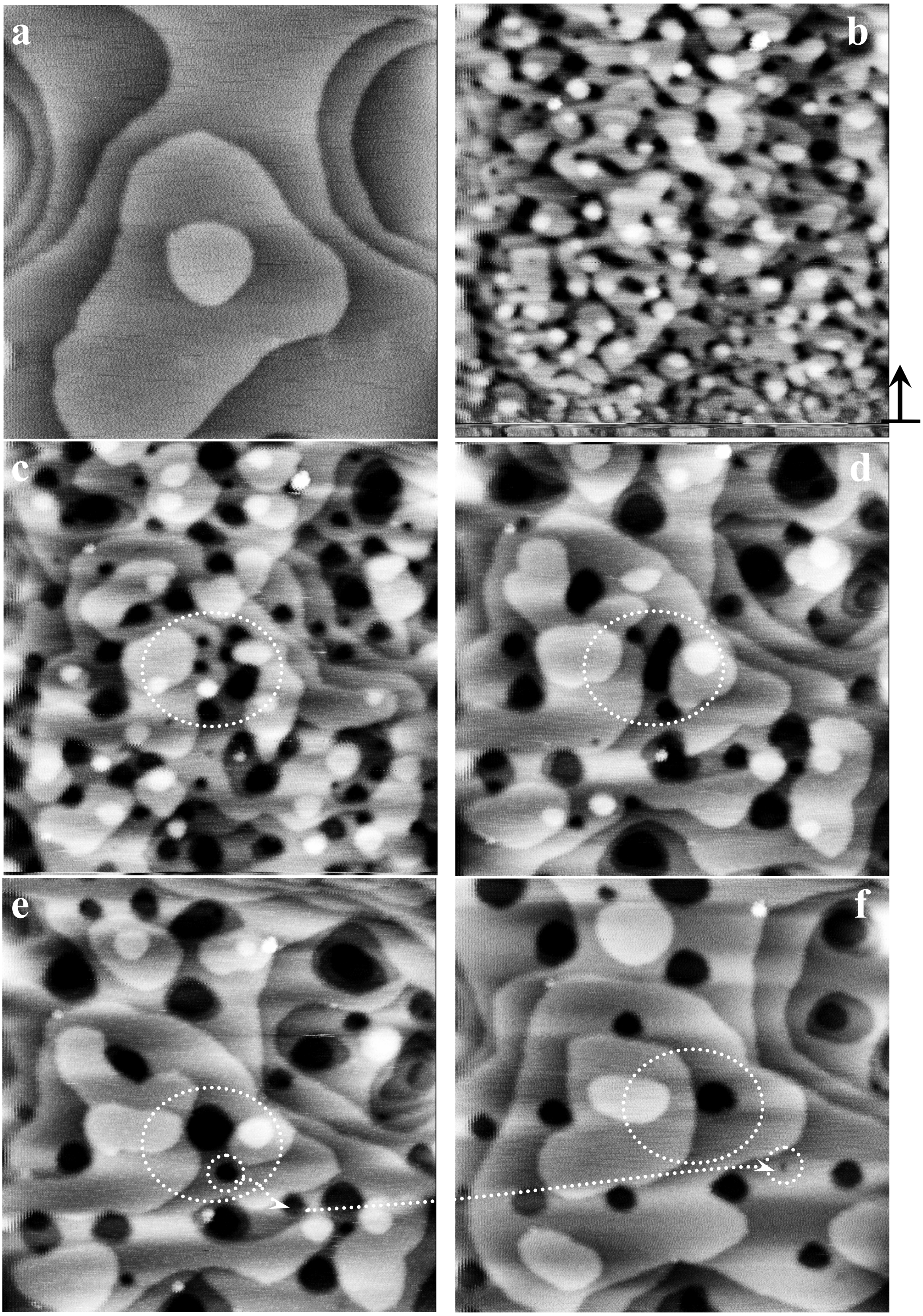

Fig.4.12 *Zn-Au surface alloying, modification of Au after OPD of Zn as a function of time. E=750 mV, scan size is 129×129 nm, scan rate is 3.39 Hz, E_{tip}=600 mV, I_{tun}=5 nA.* ***a)*** *initial Au surface,* ***b)*** *start of dissolution;* ***c)*** *5 min;* ***d)*** *18 min;* ***e)*** *41 min;* ***f)*** *98 min.*

Summarizing, it can be concluded that the terraces have changed their form with time, become greater and more uniform, Fig. 4.12f. After approximately 1 hour the initial form of gold surface (Fig. 4.12a) is distinguishable again, but still marked with relatively big holes. The more detailed analysis of surface alloying occurring in the studied system, as it is clearly seen from the results of STM measurements, is given in Discussion (Chapter 5.2).

4.4 STM study of Zn UPD at 50 °C

The STM study of Zn UPD at 50 °C was focused on the growth of a monolayer of zinc on gold at 200 mV *vs*. Zn/Zn(II) to compare it with the results of the room temperature measurements. According to the cyclic voltammogram, Fig. 4.1b, one does not expect any deposits at 750 mV. Indeed, the STM image, Fig. 4.13a, demonstrates a typical gold surface. It can be noticed, that nanometer size terraces can be resolved with good quality. This place was chosen from some part of the gold surface, which did not have any trace of an additional adsorption and contamination. It means the place shown in the figure is quite representative. In the course of measurements at elevated temperature it was noticed, that very frequently the gold surface was covered by some particles already at 750 mV. These particles were normally located at the terraces steps and were attributed to contamination, presumably of the ionic liquid. On a cyclic voltammogram no additional waves were found, so this situation seemed to be occurring only due to the temperature increase (during the STM experiment) Next sequence of images, Fig. 4b-e, was recorded one by one with the time interval between them of about 3 min. It should be mentioned, that due to the problems with thermal drift, which was difficult to avoid in this type of STM measurements, the images appear slightly distorted. Before switching the potential to 200 mV, the image was scanned just a little and then the potential jump was performed. This is marked with the black vertical arrow in the figure 4.13b. Immediately afterwards the surface was covered with zinc islands which are round and are equal in size. They are distributed on the terraces in such a way, that no preferential locations can be detected, Fig. 4.13b. Interesting that already after 151 s. the character of the film growth has changed completely, see Fig. 4.13c. Instead of separate clusters one can see the formation of a specific wormlike structure, which was also observed at room temperature at the same working electrode potential (Section 4.3.1). The development of this structure can be clearly followed, beginning from the image b in Fig. 4.13 and ending with e. For instance, one can consider the places near one of the two holes in the middle of the biggest terraces, marked with ovals.

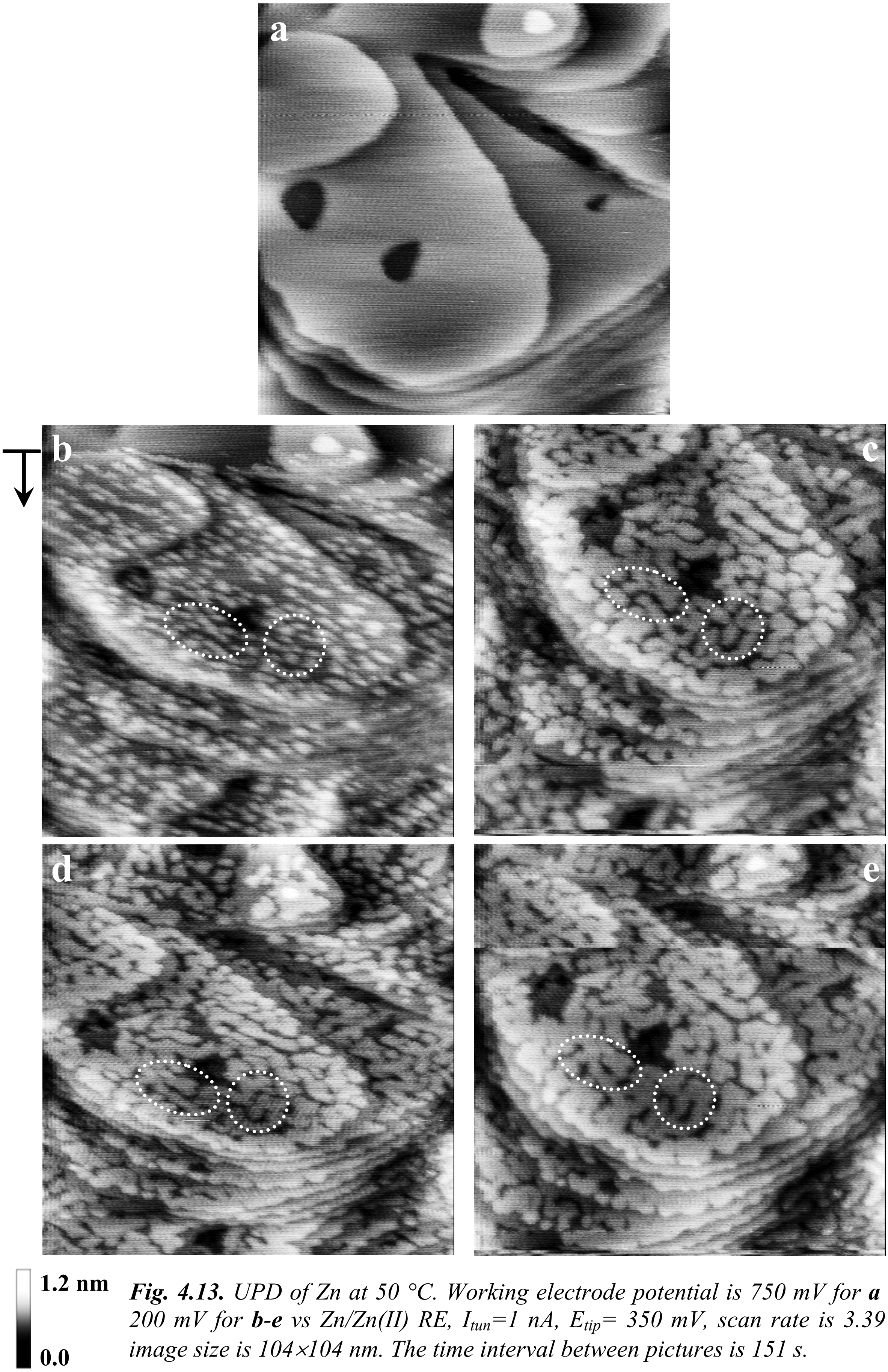

Fig. 4.13. *UPD of Zn at 50 °C. Working electrode potential is 750 mV for* ***a*** *and 200 mV for* ***b-e*** *vs Zn/Zn(II) RE,* I_{tun}*=1 nA,* E_{tip}*= 350 mV, scan rate is 3.39 Hz, image size is 104×104 nm. The time interval between pictures is 151 s.*

Distributed at the beginning as clusters, the islands formed “worms”, Fig. 4.13b and c. At this stage they are mostly separated from each other. The development of the structure is relatively fast and already next image (3 minutes later) shows, that they built some kind of interconnected structure, Fig. 4.13d. Even though distortion due to thermal drift complicates the analysis of the obtained image, it can by noticed any way, that the “worms” are continuously connected with one another, building small bridges between themselves, Fig. 4.13e.

4.5 STS measurements

In order to get a deeper insight into the electrodeposition process in the studied system, spectroscopic measurements (STS) were additionally performed. These measurements were performed also *in-situ*.

In Fig. 4.14 two representative spectra from the UPD and OPD ranges are shown. On the left side of the figure STM images depict the surface which was studied and a cross in them indicates the place, where a STS spectrum was acquired (shown on the right side of the figure). First image, a, demonstrates the Au surface covered with one monolayer of zinc. During this experiment the potential of the working electrode was slowly changed toward the Nernst potential, to the value, where the formation of the first zinc layer was completed. In this way a very homogeneous surface has been obtained. This can be seen in Fig. 4.14a. Afterwards the current–voltage curves were recorded in CITS mode (details are given in the experimental chapter, Section 3.3.4). At the end of the measurement 1024 spectra were received from one particular image. They all were carefully examined. Some of them were selected and fitted by Eq. 2.6, which is based on the assumption, that in the case of metals the density of states for sample and tip remain constant. The fitting procedure was performed using three variables: the tunneling barrier height (average work function), ϕ, distance between the sample and tip (typically 5-6 Å), z, and some constant, C. Results of the fit were accepted only in the case, when experimental and theoretical curves overlap and the output (ϕ, z, C) possesses physical values.

The example of the experimental curve fitted by described procedure is shown in Fig. 4.14a. The corresponding value of tunneling barrier ϕ for the first zinc monolayer deposited on gold is 0.75 ± 0.1 eV. The second example in this figure reveals the gold surface but now very deep in negative range at -300 mV.

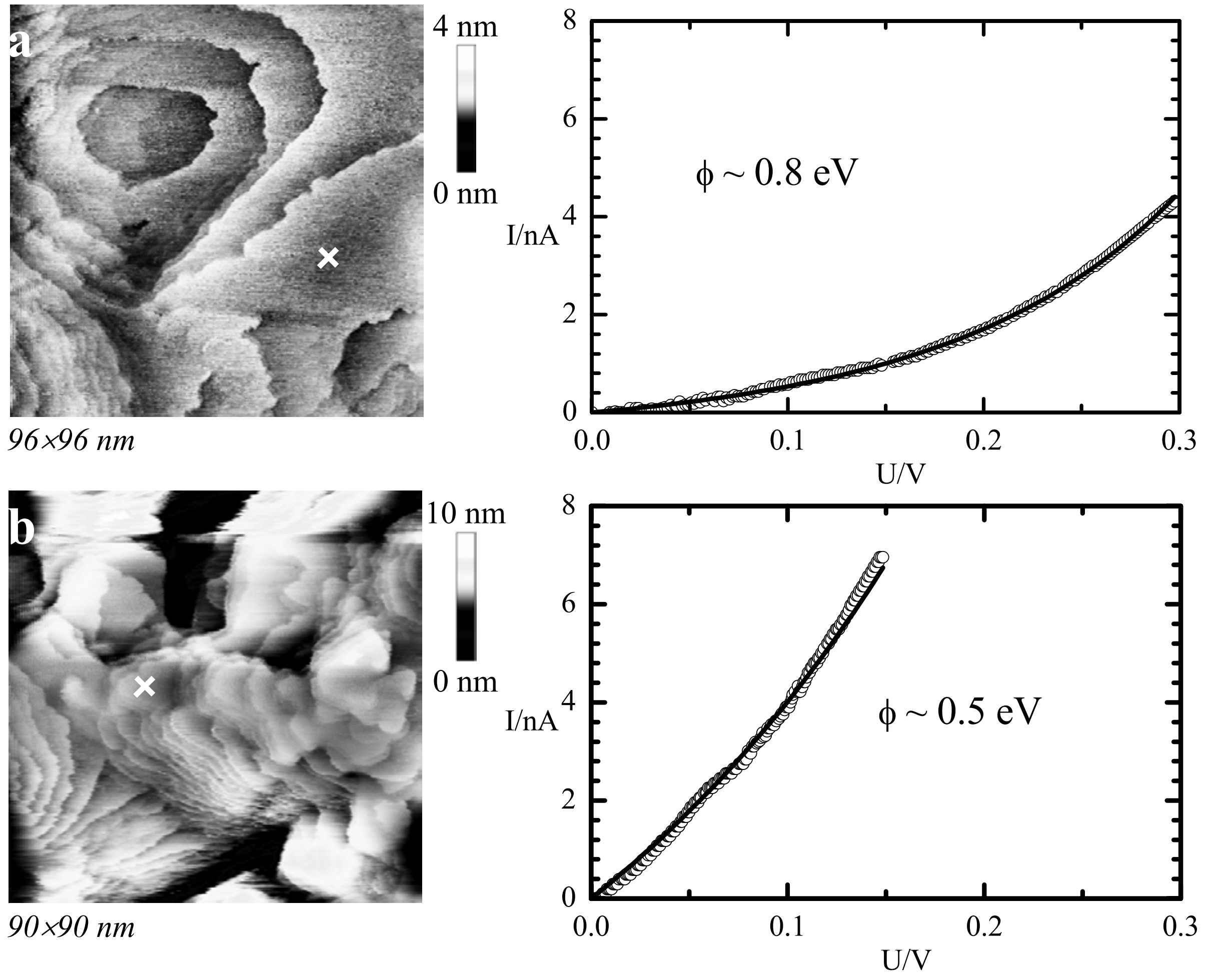

Fig. 4.14 *Experimentally measured I-U curves in:* ***a)*** *UPD range, (left) the STM image of the Au surface completely covered by 1ML of Zn, where from place marked with a cross the spectrum is taken, the experimental data is presented by circle and fitting cutve is solid;* ***b)*** *OPD range, the STM image of surface morphology at -300 mV and corresponding STS spectrum.*

At this potential the surface is covered by massive zinc layers. It should be noticed, that this potential is very close to the value of the beginning of the aluminum bulk deposition. Already from the course of the acquired spectrum it can be concluded that there is a clear difference in the tunneling barrier in this case in comparison to the first example. At the same time both curves show nonlinear dependence of the tunneling current on the tunneling voltage. The value of the tunneling barrier at -300 mV found after fitting is 0.5±0.05 eV.

In the same way the spectra were taken in the broad potential range extending from the UPD to OPD range. The results for ϕ of several independent experiments (using the different freshly prepared substrates, tips and solutions) are summarized in Fig. 4.15. The error bars in the figure represent an average error after comparison of several fits. Although the experimental values are distinctly less then the absolute values measured in vacuum, the relative changes can be easily recognized. The value obtained for a bare gold substrate in contact with the molten salt (~1 eV) is almost 5 times smaller than the absolute vacuum value of 5.1 eV [CRC 1991]. Such reduction of the tunneling barrier height can be explained by the influence of the double layer, which exists at the electrode/ionic liquid interface. As it was qualitatively shown by Venables on the basis of the jellium model, the work function is "*face-specific"* and very sensitive to any changes on the surface [Venables 2000]. Besides that, the tunneling in fluid medium is different than in vacuum, what results in changing of the vacuum barrier height [Halbritter 1995], for more details see also Chapter 2.1.

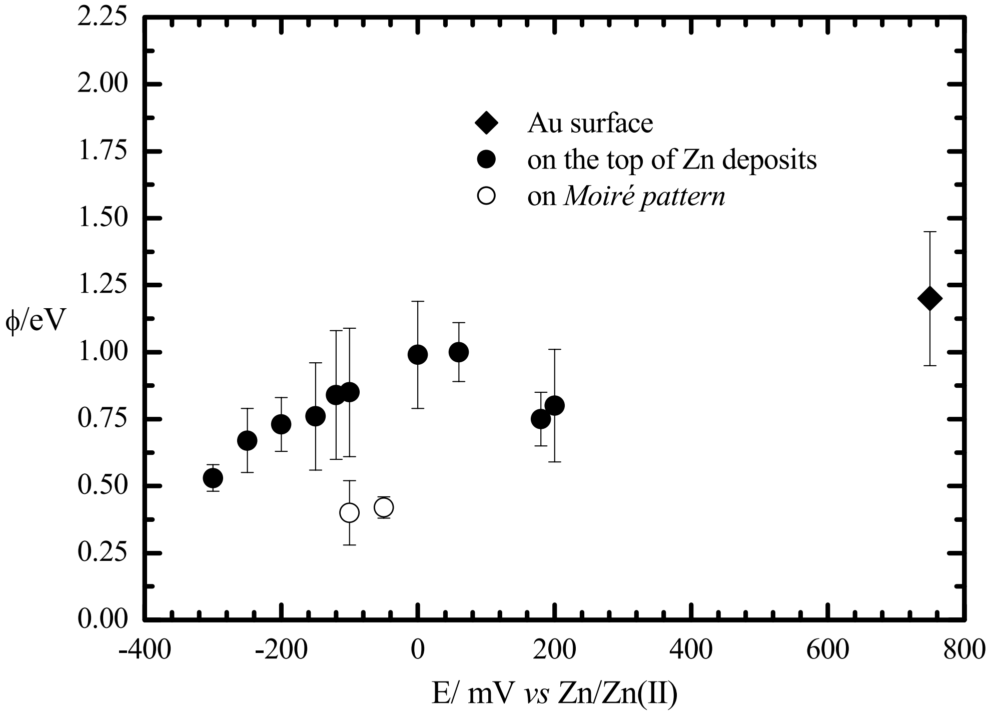

Fig. 4.15 *Effective tunneling barrier, ϕ, measured at the Au (111)/ (AlCl$_3$-MBIC) interface at different potentials, E, of Zn deposition; all points have been averaged from measurements at different sites on the same layer, constant E and at constant tip distance.*

The same tendency for the decrease of the tunneling barrier value in the molten salt in comparison to vacuum was found by Zell [Zell 2002]. The value of pure gold/electrolyte interface received in this work (1.2 eV) is in a good agreement with the values reported by Zell ~1 eV [Zell 2002].

It is interesting, that within experimental error no variations in the work function can be seen for the second (data point at 60 mV) and for the third (at 0 mV) Zn monolayers, see Fig. 4.15. In both cases the obtained value is ~ 1 eV. At the same time, even taking into account the relatively big errors bars, there is a clear drop of ϕ for the first zinc monolayer (two points around 200 mV). This can be explained by Zn-Au surface alloying. Alloying is strongly supported by the STM study, which beyond doubts demonstrated, that the alloy formation begins already during the first zinc monolayer deposition (Section 4.3.3).

In OPD range ϕ decreases strongly from 1 to 0.5 eV. As it is known at about -100 mV the very periodic superstructure can be seen during the STM measurements. The first trace of this structure can be observed already at -50 mV and thus STS spectrum could be taken from the Moiré pattern at this potential. Approximately from -100 mV next layer of zinc begins to cover the superstructure. In such a way, it was possible in some experiments to obtain STS spectra from two specific structures at constant E – from the Moiré pattern and from the place which was not occupied by it. Consequently, at -100 mV two data points could be acquired. Remarkable that ϕ from the superstructure (open symbols) is significantly less then ϕ from the zinc deposits. Following the observed tendency of decrease in the work function with decrease of the working electrode potential, it can be assumed that the value for pure aluminum bulk deposition should be around 0.4 eV. Indeed, the work function for pure Al deposition has the same value of 0.4 eV, obtained by Zell during the study of Co-Al codeposition [Zell 2002]. So, $\phi \sim 0.4$ eV (from this investigation of Zn electrodeposition) measured on the Moiré structure may indicate underpotential deposition of Al on the top of zinc layers. In addition it is necessary to add, that the same statement is followed from the comparison of CVs for the pure molten salt [Zell 1999] and containing zinc, what is discussed in Section 4.3.2.

5. Discussion

5.1 Layer-by-layer mechanism of Zn deposition

Zinc electrodeposition from an ionic liquid, monitored by *in-situ* STM, was conducted in this work for the first time. The results have shown that during the electrochemical phase formation in the UPD range, Zn exhibits a strong tendency to form very uniform monolayers on the Au(111) surface. The deposited layers are so homogeneous, that they nicely reproduce the original surface morphology of the substrate. By deposition of up to four zinc monolayers, where three of them were obtained in the UPD range, the initial shape of the gold terraces could be followed. A layer-by-layer growth was observed in other STM works as well, however only one or two UPD-metal layers could be experimentally detected [Randler 1999], [Zell 1999]. So, in the subsequent part a first discussion of this interesting "many layers" zinc deposition phenomenon will be given.

The underpotential deposition is nowadays a well known phenomenon and considered as the initial stage of a metal electrocrystallization. First studies of the underpotential deposition were performed with the very low concentration of metal ions in the solution. Due to this fact, probably, it was originally understood as a purely adsorption process [Pangarov 1983]. The deposition of metals in the UPD range can involve formation of both 2D metal phase and surface alloying [Budevski 1996]. UPD occurs at conditions of "undersaturation".

Thermodynamically the underpotential range is determined as $\Delta E_{2D} = E - E_{2DMe} > 0$ with the equilibrium potential of 2D metal phase E_{2DMe} given by

$$E_{2DMe} = E^0_{3DMe} + \frac{RT}{nF} \ln\left(\frac{a_{Me^{n+}}}{a_{2DMe}} \right), \tag{5.1}$$

where and E^0_{3DMe} is the standard potential of the bulk metal phase [Budevski 2000].

The phenomenon of UPD, in principle, can be explained in terms of a strong interaction between the substrate and deposited metal. Generally, three cases of metal growth during the electrochemical phase formation can be distinguished [Budevski 1996]: "*Volmer-Weber*" (VW), "*Frank-van der Merwe*" (FM) and "*Stranski-Krastanov*" (SK) modes, Fig. 5.1.

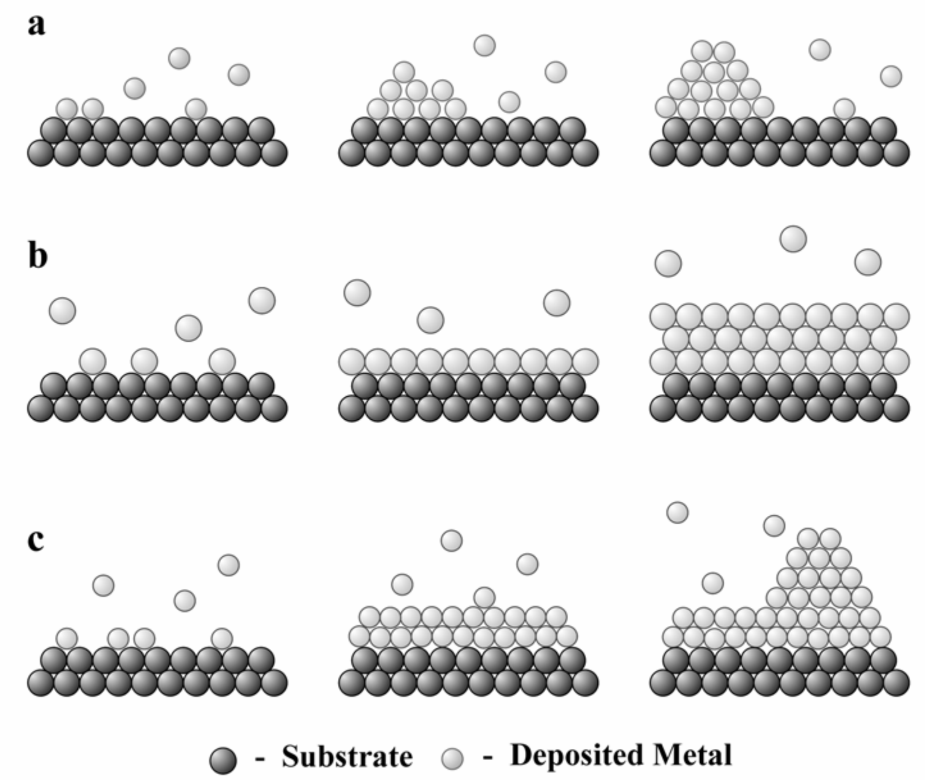

Fig. 5.1 *Schematic representation of the metal epitaxial growth on foreign substrate:* ***a)*** *Volmer-Weber (3D),* ***b)*** *Frank-van der Merwe (2D) and* ***c)*** *Stranski-Krastanov (2D+3D)****.***

The first mode is related to such systems, where the binding energy between atoms of the deposited metal is higher, than between atoms of this metal and the substrate. For such a case the crystallographic misfit of the two lattices is not important and the 3D growth takes place, Fig. 5.1a. For the FM mode the metal-substrate binding energy is much higher than that of metal-metal. Besides that, this model is regarded to a low crystallographic misfit and hence the layer by layer growth occurs, Fig. 5.1b. This type of growth can extend from the UPD to

OPD range and the thickness of deposited structure (or the number of monolayers) will be determined by the strength of the interaction energy. For the relatively big misfit between atoms of substrate and metal, the SK mode, which combines two previous mechanisms of growth, dominates, Fig. 5.1c. Due to the strong interaction energy the layer-by-layer growth (FM) will occur at the initial stage of the deposition. However, if the atomic radii of metal and substrate are significantly different, the lattice mismatch will become more pronounced with increasing the number of the addlayers. At some point the FM mode will not be favorable any longer and the 3D growth will begin, Fig. 5.1c.

Considering the atomic radii of zinc and gold, it can be noticed that they are very close (1.37 and 1.44 Å, respectively). The same extend of the crystallographic misfit is known to occur for the Pd/Au system. The atomic radii of palladium and zinc are equal. In this sense it could be expected that both systems (Zn/Au and Pd/Au) reveal the similar behavior during the deposition process. Indeed, in the work of Naohara et al. the electrochemical layer-by-layer growth of Pd on Au(111) electrode from H_2SO_4 electrolyte containing $PdCl_4^{2-}$ was observed by means of the electrochemical quartz crystal microbalance and *in-situ* STM [Naohara 1998]. However, the small crystallographic mismatch for the layer-by-layer growth is not a crucial factor and can not alone determine the deposition mode. An influence of the interaction energy is more important. But before an energetic aspect of the growth mechanism will be discussed, we will consider some other important features of the zinc electrodeposition.

The underpotential deposition of metals is strongly affected by the electrochemical ambient, or solution. The impact of a solution can be shown on the example of the Ni deposition on Au(111). *In-situ* STM study of the electrodeposition of Ni on Au(111) from various electrolytes demonstrated that the first Ni clusters appeared below the Ni/Ni^{2+} Nernst potential [Möller 1997]. Whereas the STM investigation on the same metal system but from a room temperature molten salt demonstrates, that already in the UPD range a complete monolayer of nickel is formed [Zell 2001]. It is remarkable, that in the first case the gold surface underwent a reconstruction and the nucleation of Ni occurred preferentially at the defects on the reconstructed gold surface (at the elbows or at gold steps, depending on the overpotential) [Möller 1997]. As it was shown during the deposition of Ni on Au(100), for initiation of a nucleation on the relaxed surface lower overpotential is required, than for that on reconstructed surface [Möller 1999]. This can be due to the fact that the different mechanisms of a strain release are involved in these cases. Remarkably, that in the molten salt the reconstruction of the gold surface is not detected [Zell 2001]. So, it is evident that the type of an electrochemical solution (aqueous solution against molten salt) has influence on the deposition process. Metals, dissolved in the molten salt, are solvated differently than in aqueous solutions [Dent 1990], [Hussey 1994] and consequently this explains such a difference in the electrochemical behavior of metal ions.

The deposition of zinc from an ionic liquid, similar to the one used in this work, was performed by Hussey and Pitner [Pitner 1997]. However, these authors reported about two UPD peaks only. A possible explanation of such discrepancy between their work and this study can be due to the fact, that the polycrystalline Au (and not Au(111) as in this work) surface was used. As it was discussed above the relaxation of the uppermost layers of the substrate can play a significant role in the deposition process. Not less an important role has the crystallographic orientation of the substrate. The whole UPD process (a number of peaks on a cyclic voltammogram, their position etc) might be strongly affected by the crystallographic orientation [Jüttner 1980], [Bort 1983]. For instance, in the work of Hümann et al. the underpotential deposition of Cd on Cu(111) and Cu(100) electrodes from the $CdCl_2$/HCl solution was studied [Hümann 2003]. From this study, performed by in-situ STM, the atomically resolved images showed that the deposited structures had different character. For the system Cd on Cu(111) a hexagonal surface structure was obtained, whereas the deposition of Cd on Cu(100) led to the streaks with a $(\sqrt{2}\times\sqrt{2})R45°$ missing row structure. Besides that, already from the analysis of cyclic voltammograms, obtained in the study of Hümann et al., it can be noticed that the UPD peaks are located at the different electrode potentials [Hümann 2003]. In the study of UPD of Ag on (111) and (100) crystallographic planes of Au [Garcia 1998] the results had a similar character as in the work of Hümann et al. [Hümann 2003]. Interestingly, at low underpotentials the deposition on Au(111) occurred on monoatomic steps, whereas on Au(100) on flat terraces [Hümann 2003]. The cyclic voltammetry study of underpotential deposition of Zn on Au(111), Au(100) and Au(110) performed by Aramata and Moniwa showed, that deposition on a high-index gold electrode is distinctly different from that on low-index electrodes [Aramata 1994].

Although the system studied by Hussey and Pitner [Pitner 1997] is very close to that one of this work, these authors used a polycrystalline Au electrode. Hence, the crystallographic orientation of gold substrate (polycrystalline *vs.* (111) plane) definitely plays a crucial role in the appearance of different results of Zn UPD on gold surface. Another possible explanation on this subject should be considered as well, namely the experimental techniques used in both studies. In the work of Hussey and Pitner the conventional electrochemical methods were applied [Pitner 1997], which did not allow to resolve a real space morphology, in contrast to the STM study of this work.

From the studies in aqueous solutions it is known, that the metal UPD can be accompanied by an anion adsorption [Kolb 1978]. Similar as in the case of Cu UPD on Au(111) [Batina 1992], [Will 1993], the anion adsorption during the zinc underpotential deposition can probably determine the kinetics of a surface process. Several investigations in aqueous electrolytes were performed to understand the correlation between the Zn UPD and anion adsorption in detail. For example, by means of cyclic voltammetry measurements [Taguchi 1995], [Aramata 1998] and radiotracer technique [Horányi 1997, 1997a] it was discovered that some anions co-adsorbed during the zinc underpotential deposition on platinum. Besides that, the presence of the anions affected the UPD potential, shifting it in the negative direction [Taguchi 1995]. At the same time for the Zn UPD on gold the influence of the phosphate anions was not detected [Aramata 1998]. Unfortunately, at the moment only one STM work on this problem exists in literature to our knowledge. The STM investigation of Takahashi et al. of the Zn UPD on Au(111) in phosphate solution demonstrate the adsorption of an ordered anion adlayer and the formation of a zinc phosphate complex [Takahashi 2002].

In the STM studies of this work it was not possible to achieve the atomic resolution to clarify the microscopic structure of the deposited monolayers. However, an analysis can be performed with atomic resolution by measuring z-profiling (the height) of the surface structure. The thickness, h, of the monolayers was measured and is shown in Fig. 5.2 as a function of the applied potential. The data presented in Fig. 5.2 were obtained from the results of several independent experiments, where within one single set the thickness was evaluated on many different sites. The error on the graph represents an average value and is around ± 10 %. For the calibration of the present results the height of Au(111) step edges of 2.35 Å was used.

The experimental results show that for the first monolayer the thickness is ~2.2 Å. In the Lewis acidic composition of the room temperature molten salts (in this work: $AlCl_3$/BMIC - 58/42) the metal-ion is complexed by $AlCl_4^-$ [Dent 1990]. If one considers the anion adsorption like $AlCl_4^-$, then on the basis of simple geometrical considerations (taking into account the atomic radii and assuming the metal atoms as hard spheres) the thickness of such adsorbed layer should be more that 7 Å. This value lies clearly beyond the experimental error, so $AlCl_4^-$ adsorption can be excluded. Similarly, the height of the Zn monolayer on Au can be estimated and should be 2.20 Å. This value precisely agrees with the experimental one, Fig. 5.2.

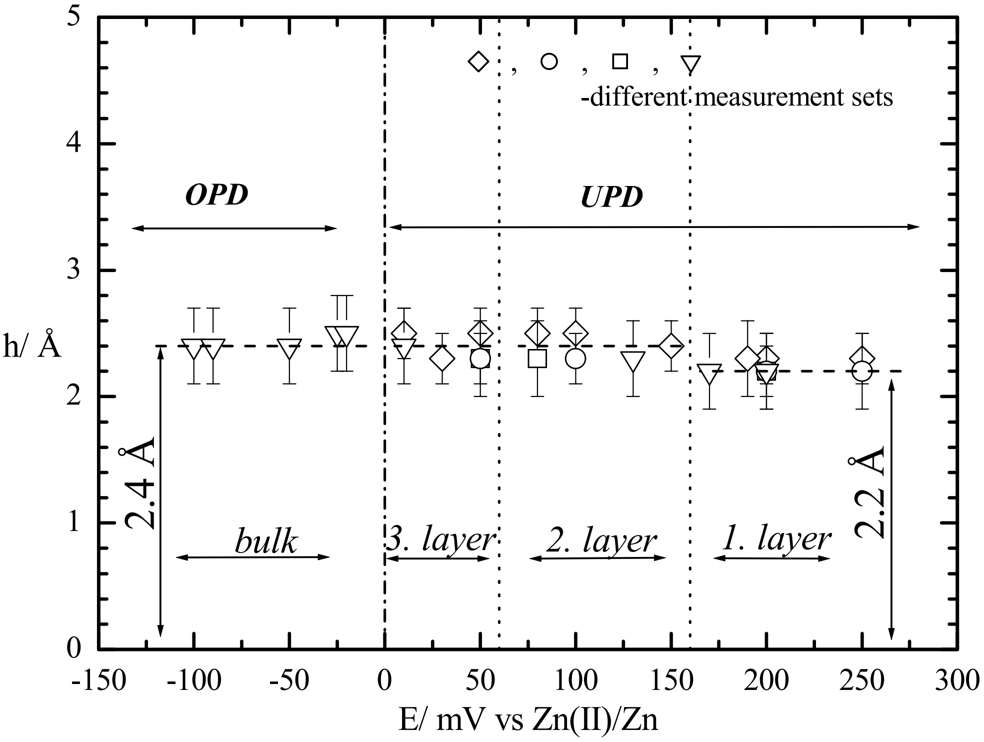

***Fig. 5.2** The height, h, of the zinc monolayers in the UPD and OPD ranges. For the first monolayer the obtained height is 2.2±0.2 Å and for subsequent layers it stays 2.4±0.2 Å.*

It is interesting, that according to Fig. 5.2 the height of the layers seems to increase slightly for the second and third monolayer and stays constant into the bulk deposition range. The value calculated for the bulk zinc (zinc monolayer on zinc surface) is 2.24 Å. Hence, the experimentally obtained monolayer thickness follows the theoretical predictions of the zinc deposition and anion coadsorption does not occur.

The anion adsorption in the studied system, nevertheless, should not be excluded completely. The chronoamperometric measurements showed that at the potential step from 750 to 400 mV the current response has completely different character, than all current transient curves both in the UPD and OPD ranges (except of the one, which was obtained very deep in OPD range and attributed to the Al 3D growth), Chapter 4.2. The fact that STM study did not support this assumption can be due to a very fast desorption-adsorption process, which could not be monitored by *in-situ* STM.

5.2 Zn-Au surface alloying

As it was seen in the previous part of this chapter, the growth of metal on a metal surface is a very complex process. One of the interesting aspects of this, which was already mentioned, but not considered so far, is the possibility of surface alloying, when two metals intermix into one phase. Surface alloying between the two metals of interest can occur in both cases – if bulk alloying of these metals takes place, for example during of the epitaxial growth of Au on Ag(110) [Rousset 1992], but also when it does not, as in the case of the Au deposition on Ni(110) [Nielsen 1993]. As it follows from its name, surface alloying exists only in a few uppermost layers of the substrate metal. Also, as for the nucleation and growth, the kinetics of surface alloying is strongly affected by surface inhomogeneities and crystallographic orientation. Experimental observations show that surface alloying is more pronounced on surfaces with (111) crystallographic plane [Budevski 1996]. Although there is a number of investigations (both experimental and theoretical, [Chan 1992], [Tersoff 1995], [Christensen 1997]) in this field, the whole mechanism is not fully understood at the moment.

The STM images, taken on the dissolution of deposited zinc monolayers, demonstrate that the gold surface is modified - pierced by a number of small holes, see Section. 4.3.3. These holes, the size and amount of which is affected by the number of deposited layers, are a good evidence of surface alloying. It is remarkable that formation of surface alloying begins already during the underpotential deposition of the first Zn monolayer on Au. As it was outlined already in Section 4.3.3, after the dissolution of one deposited monolayer the surface structure is only slightly modified, see Fig. 4.11b. Measurements of the *z*-profiles from such a surface demonstrate that the surface alloying takes place only over one surface layer. This is clearly seen in Fig. 5.3a, where a typical *z*-profile (right) over gold surface (left), scanned just immediately after applying of 750 mV - the dissolution potential value, is depicted. For convenience, one hole is marked, the depth of which is 2.2±0.2 Å. It means that, the penetration depth of zinc atoms is only one surface layer of gold. Small islands which appear after the dissolution and disappear during first several seconds of subsequent scanning (compare bottom and upper part of the STM image, Fig. 5.3a) have the characteristic height of 2.2±0.2 Å. Taking into account the experimental error (±0.2 Å) and the fine difference between gold and zinc islands height (Δ_{theor}=0.15 Å), it is problematic to conclude what is the nature of these islands. They can belong to both: to the gold, which is forced out from the surface lattice by zinc and also to the zinc, which requires a bit longer time to dissolve completely.

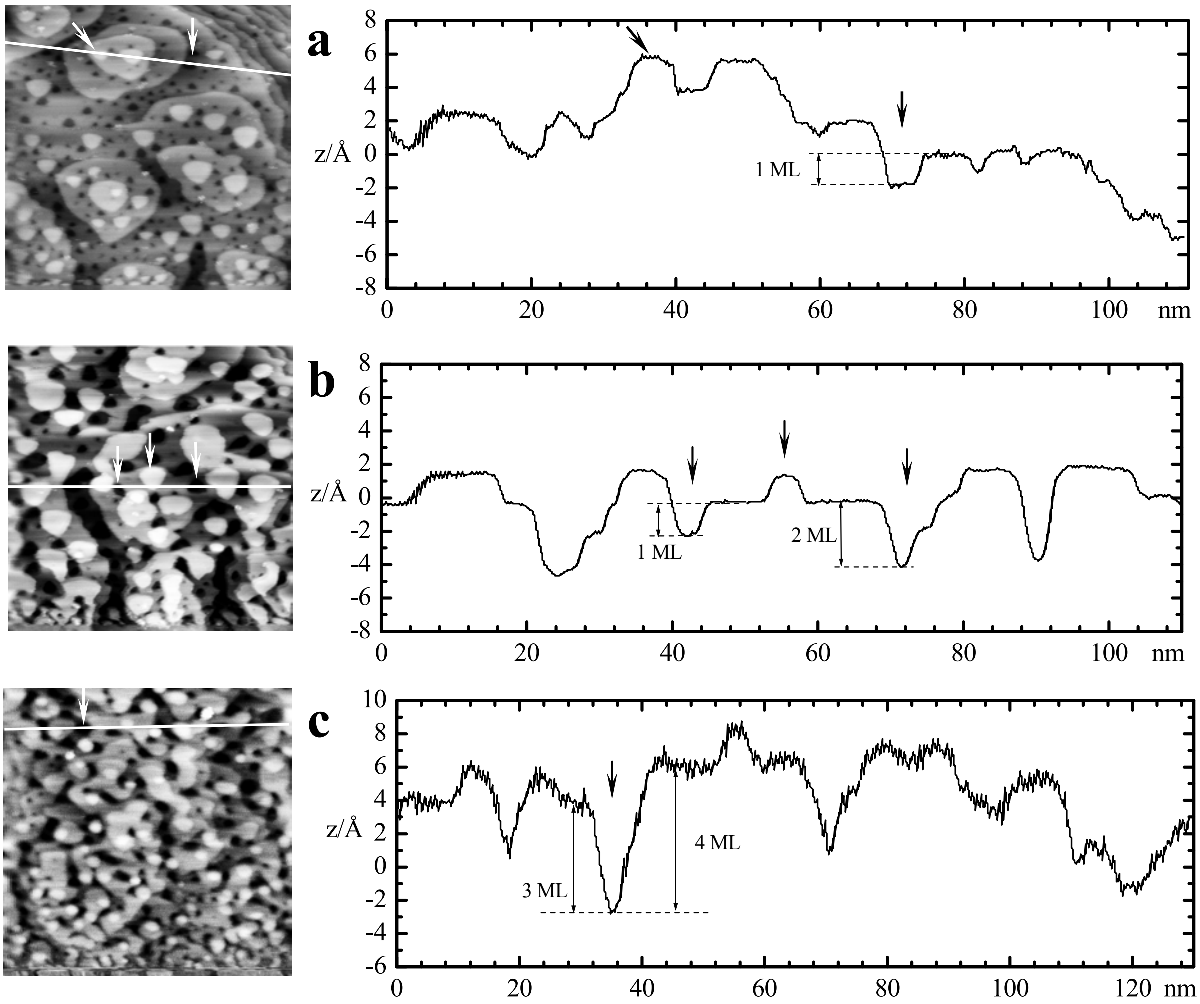

__Fig. 5.3__ Z-profile of gold surface after dissolution of __a)__ one, __b)__ two and __c)__ more then 4 zinc monolayers, ; __left__ is the bare Au(111) after dissolution of deposited zinc layers and __right__ is z-profile of the surface. ML is for monolayer of gold, the experimental value for 1ML is 2.2±0.2 Å, for 2ML is 4.3±0.2 Å, and for 4ML is 8.6±0.3 Å.

After dissolution of two zinc layers, the obtained surface is distorted to a greater extent, see Fig. 4.11d. At the same time, the depth of holes now exhibits two distinct values - 2.2±0.2 Å and 4.3±0.2 Å, Fig. 5.3b. So, surface alloying in this case occurs over one to two gold surface layers. The possible scenario of surface alloy formation could be as following. The zinc adatoms form a complete monoatomic film on the gold and simultaneously an intermixing of them with the uppermost surface layer takes place. At the moment when the second zinc layer settles on the substrate, the surface will consist of the gold atoms again (or of some intermixing phase from Au and Zn). Thus the situation would be similar to the first monolayer deposition and Zn-Au surface alloying should be again favorable.

The dissolution of more than 4 monolayers of zinc brings more pronounced destruction of the gold lattice, see Fig. 4.12. The STM image taken in the beginning of the dissolution, discloses a completely "unrecognizable" gold surface, compare Fig. 4.12a and b. The *z*-profile, Fig. 5.3c, demonstrates a distribution of hole depths. They change in the range from 1 to 4 monolayers (from 2.2 to 8.6 ± 0.3 Å). Therefore, from analysis of the *z*-profile, it follows that each monolayer of zinc intermixes with the gold surface, up to 4 uppermost layers. The depths of the zinc atoms penetration depends obviously on a number of deposited layers, but not on the deposition time, since the latter was nearly equal (±15 min). However, a diffusion into deeper layers is probably also kinetically hindered or/and requires longer than experiments of this work time (more than several hours). To go deeper inside the bulk phase the interlayer mass transport should overcome an activation energy barrier, which is high at room temperature [Budevski 1996].

Thermodynamically the epitaxial growth of one material (D) onto another one (S) can be characterized with the help of Young's equation [Adamson 1990], [Röder 1993]:

$$\gamma_S = \gamma_I + \gamma_D \cos\theta \,. \tag{5.2}$$

Here, γ_S and γ_D are surface free energies of the substrate-vacuum and deposit-vacuum interfaces, respectively, γ_I that of the deposit-substrate interface and θ is the contact angle. Thus the modes of metal growth, introduced above, can be described now more quantitatively, see e.g. [Lüth 2001]. If $\theta = 0$, then $0 \geq \gamma_D + \gamma_I - \gamma_S = \Delta\gamma$ and the layer-by-layer growth (Frank-van der Merwe mechanism) is expected. For the formation of 3D phase, $\theta > 0$ and $0 < \gamma_D + \gamma_I - \gamma_S$. This corresponds to the Volmer-Weber mode. The third case, the intermediate between layer-by-layer and 3D growth (Stranski-Krastanov type), occurs when $\Delta\gamma$ changes its sign or increases from zero to some positive value. It means that condition $\Delta\gamma \leq 0$ is held only for a limited number of layers in comparison to the Frank-van der Merwe mechanism, where $\Delta\gamma$ should be negative for all layers.

The treatment of the system in terms of the surface energy, Eq. 5.2, is valid strictly for solid/vacuum interface only. However, it can be assumed in the first approximation, that the same relations between energies should remain for the solid/liquid interface. Indeed, the work function of metals in contact with the melt is reduced by constant value of ~ 4 eV [Freyland 2003], what is also supported by the STS results of this work, Chapter 4.5. The surface free energy of zinc is 990 mJ·m^{-2} and that of gold is 1500 mJ·m^{-2} [Boer 1988]. Hence Eq. 5.2 can be written for this particular system as:

$$\Delta\gamma/\mathrm{mJ\cdot m^{-2}} = \gamma_i - 510. \tag{5.3}$$

The interface energy γ_i is normally poorly known, but it can be assumed that γ_i is much smaller than γ_a and γ_s and can be neglected [Röder 1993]. Thus, this simple analysis shows that the layer-by-layer growth of Zn on Au surface is favorable ($\Delta\gamma \leq 0$). The understanding of growth mechanism in terms of surface and interface energies is related to the macroscopic approach but not microscopic. Besides that, to consider the appearance of the surface alloying the role of the interface energy should not be neglected, though. The negative interfacial energy accounts for dissolving deposited metal into the substrate. But such an energy difference is present in the system, which form bulk alloying [Tersoff 1995]. As it is known the Zn-Au system does not correspond to such a situation – a number of intermediate compounds is formed [Massalski 1990]. Otherwise surface alloying would be favorable already in the underpotential range [Kolb 1978].

The positive interfacial energy can be due to a structural misfit between substrate and deposited layer. Different atomic sizes of the two metals ($r_{Zn} < r_{Au}$) cause the intrinsic surface stress. The release of the strain is known to account for the intermixing at the surface [Tromp 1992, 1993].

Unfortunately, the calculations, which would take into account the macroscopic and microscopic approach, are missing at the moment and further more quantitative analysis of Zn-Au surface alloying is not possible.

5.3 Nucleation and growth of Zn

In the previous two parts of this chapter the general aspects of the zinc deposition mechanism have been considered. The complete understanding of this process, however, requires an additional analysis of the deposition kinetics. Kinetic parameters of the zinc electrodeposition on gold from Lewis acidic $AlCl_3$/BMIC can be evaluated using current transients results of the chronoamperometric measurements (Chapter 4.2). Generally, with the help of different theoretical models, which can be applied for a description of the current-time response, it is possible to classify such quantities and processes as diffusion coefficient, adsorption kinetics, nucleation, growth rates, surface alloying etc. On the other hand, the deposition process, as it was shown in this work, can be rather complex, when certain parameters have a strong influence on the deposition: the type and crystallographic orientation of the substrate, deposit-substrate interaction, electrolyte, temperature.

Several general models for a description of current transients can be found in the literature. A good overview of them is given in [Southampton 1990]. Qualitatively the theoretical descriptions are based on the following assumptions. At the beginning a nucleation proceeds with a constant rate and at certain locations on the electrode surface – on the active sites. A number of active sites might change with the time, see Eq. 2.18, and two types of nucleation are normally considered: instantaneous and progressive, Eq. 2.20 and 2.21, respectively. The rate determining step plays a significant role in the theoretical description of the deposition kinetics. Such a step can be a rate of an incorporation of adatoms in the growing centers and/or rate of the mass transport (diffusion), see also Section 2.3.2.

The results of the chronoamperometric measurements of this work are shown in Fig. 4.3. None of the typical theoretical models, including a two-dimensional electrocrystallization with the rate of lattice incorporation as determining step, which corresponds to the monolayer growth [Budevski 1996], gave a reasonable agreement with the experimental results.

M. Palomar-Pardavé et al. proposed a procedure for analyzing the current transient curves [Palomar-Pardavé 1998, 2000], which considered a process occurring during the silver overpotential deposition on a carbon electrode as a sum of several contributions. Each contribution was modeled independently. Thus, after a proper analysis, the final general equation included 2D-2D or 2D-3D nucleation transitions and the effect of double layer charging [Palomar-Pardavé 1998]. For description of the latter, the same approach as in the work of Hölzle and coworkers was used [Hölzle 1994].

On the basis of the analysis used by Palomar-Pardavé at el. [Palomar-Pardavé 1998, 2000] it was assumed, that in the case of zinc electrodeposition on Au(111) from the ionic liquid more than one process could be involved. The first one is due to adsorption and the second one is unknown and has to be determined. It is important to understand, that adsorption overlaps with the double layer charging and in principle three contributions should be considered. For simplicity, however, adsorption and double layer charging are described as a one process.

Assuming that the rate of adsorption is much higher than that of desorption, the current-time dependence can be expressed as [Barradas 1985], [Varela 1992]:

$$I_{ads}(t) = k_{ads} q_{ads} \exp(-k_{ads} t) , \tag{5.4}$$

where k_{ads} and q_{ads} are the rate constant and total charge, respectively, which are attributed to the adsorption process.

Considering the deposition process in general, it can be assumed, that after some growth time, the depositing material will extend into the bulk electrolyte [Hyde 2003]. Such a situation will produce some intermediate case between two- and three-dimensional growths. The mathematical treatment, which would corresponds to this model, is not so straightforward. Nevertheless, Scharifiker and Hills gave an approximate solution of such a problem [Scharifker 1983]. Hemispherical nuclei are located on the surface and the mass transport is controlled by the hemispherical diffusion. Actually, a nucleus is not necessary hemispherical. The shape is not important for this model, because the diffusion zones grow much faster then the nucleus. After a certain time the diffusion zones will come in contact with each other and overlap. The supply of a new material can be done now only perpendicular to the substrate plane and the linear diffusion sets in. Hence the whole system can be reduced to the two-dimensional problem, which should be integrated over a number of monolayers. The resulting equation for the instantaneous nucleation is given by [Scharifker 1983]:

$$I_{Sch}^{inst} = \frac{nFD^{1/2}c^{\infty}}{\sqrt{\pi t}}\left\{1-\exp\left(-N_0 \pi k D t\right)\right\}. \tag{5.5}$$

In this equations $k=(8\pi cM/\rho)^{1/2}$, where c^{∞} is the concentration of zinc in the bulk, M is its molecular weight, ρ is the density and all other parameters have their usual meaning. In such a way a new approach in evaluating the results of the current-transient experiment is attempted, where the resulting current is given by:

$$I_{total} = I_{ads} + I_{Sch}^{inst}. \tag{5.6}$$

I_{ads} is given by Eq. 5.4 and the second contribution to the total current is determined by Eq. 5.5. Since the chronoamperometric curves in the UPD and OPD ranges exhibit similar behavior they both were analyzed by Eq. 5.6 and a typical result is shown in Fig. 5.4.

As it can be seen from this figure the model (Eq. 5.6) describes the experimental observations quite well. Remarkably, the same model indeed can be used for the description of the underpotential and overpotential deposition of zinc. This means, that a similar process takes place in both ranges. This suggestion is supported by STM results of this work, which revealed the layer-by-layer mechanism of zinc growth extending from the UPD to OPD ranges. Table 5.1 summarizes the kinetic parameters of the zinc deposition on Au(111) from the room temperature molten salt obtained on the basis of this model.

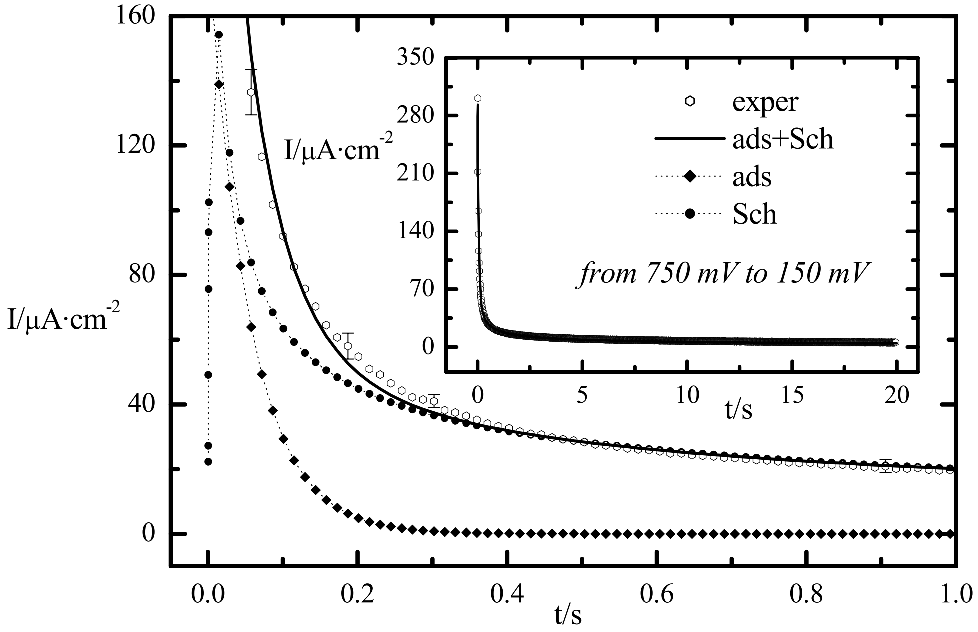

Fig. 5.4 *Comparison between experimental (open diamonds) and theoretical transients (line) for zinc UPD, with a potential step from 750 to 150 mV, see Fig. 4.3. The theoretical model is a sum of two process - adsorption (filled circles) and instantaneous nucleation and growth under diffusion control (filled squares), see Eq. 5.6. In the inset only experimental and theoretical curves for the whole time range are shown.*

Tabl. 5.1 *Kinetic parameters of the zinc electrodeposition from the room temperature molten salt on Au(111), estimated using Eq. 5.6*

		E vs. Zn/Zn(II)/mV	k_{ads} /s^{-1}	q_{ads} /$\mu C\cdot cm^{-2}$	$D\cdot 10^{7}/cm^{2}\cdot s^{-1}$	$N_0\cdot 10^{-11}$ /cm^{-2}
UPD	1ML	200	15	10	0.33	1.0
		150	18	10	0.34	1.1
	2ML	50	3.9	36	0.56	1.1
	3ML	0	3	37	0.70	1.2
OPD		-50	2.0	84	0.65	~5.0
		-100	3.0	67	1.11	
		-150	3.0	103	1.10	
		-200	3.5	143	1.10	
		-250	3.0	233	1.30	
		-300	2.0	300	1.31	
		-350	2.9	379	5.0	

The kinetic of adsorption is defined by the rate constant k_{ads} and the total charge q_{ads}, Tab. 5.1. As it is seen, the rate constant for the first monolayer deposition is significantly higher, than for all subsequent layers. The theoretical charge corresponding to the formation of one zinc monolayer is much greater than the obtained values of q_{ads}. So, they are inadequate. Indeed from the results of STM measurements, it follows, that at 200 mV, for instance, the formation of ~0.5 ML is determined, see Fig. 5.11.

According to the results, presented in Tab. 5.1, the number of active sites N_0 appears to be independent on the potential, whereas it distinctly varies from the UPD to OPD ranges. The rough analysis of STM images yields $N_0 \sim 10^{12}$ cm^{-2}. In both cases the number of active sites is greater than the value of ~ 10^5 - 10^7 for the metal (Ag, Hg) electrodeposition in an aqueous solution [Scharifker 1999]. Particularly, during the zinc electrodeposition from $ZnCl_2$+KCl solution the value of $N_0 \sim 10^6$ cm^{-2} was obtained [Lin 1993]. Moreover, N_0 is very sensitive to the time resolution due to the exponential dependence (Eq. 5.5), particularly in the region of the maximum in current transient, see Fig. 5.4, and can not be determined precisely. Concerning the diffusion coefficient, it is only slightly lower than that one received by the Cottrell equation, Tab. 4.1 and in general a good agreement can be claimed.

In spite of the good agreement between experimental results and theoretical fit (Fig. 5.4), the suggested model (Eq. 5.6) does not follow the "real" situation observed in the STM. The formation of wormlike structures and subsequently spinodal decomposition (see next chapter) reveal a slow mechanism of zinc surface alloying and therefore a model including lattice incorporation is of interest at longer times [Armstrong 1966]:

$$I_{3D-LI}^{progr} = nFk_{3D}^{\uparrow}\left\{1-\exp\left(-\frac{\pi M^2 N_0 (k_{3D}^{\rightarrow})^2 A_3 t^3}{3\rho^2}\right)\right\}. \tag{5.5a}$$

where $k_{3D}^{\uparrow}$ and $k_{3D}^{\rightarrow}$ are rate constants of islands growth perpendicular and parallel to the electrode plane, A_3 is the first order nucleation constant and all other parameters have their usual meaning. Thus the lattice incorporation as a rate determining step approaches closely to the mechanism observed in STM as well. The typical comparison of experimental results with this model is shown in Fig. 5.4a. The following parameters have been obtained at 200 mV: k_{ads} = 7.3 s^{-1}, q_{ads}= 50.7 μC·cm^{-2}, $k_{3D}^{\uparrow}$= 5.7·10^{-11} mol·cm^{-2}s^{-1}, $A_3(k_{3D}^{\rightarrow})^2$=0.06 mol^2·cm^{-6}s^{-3}. In comparison with diffusion control mechanism above the total charge q_{ads} is increased. The most important observation in Fig. 5.4a is that the lattice incorporation model consistently describes a small but finite current at longer times – e.g. 5 – 10 μA·cm^{-2} at t=20 s. Only in this way the continuous increase of the surface coverage as observed in the STM images with time (see bellow) can be explained. As it can be seen from Fig. 5.4a, the agreement between the model and experiment is poor at short times in comparison with Fig. 5.4. This may indicate that the adsorption term (Eq. 5.4) does not describe the short time behaviour properly. Unfortunately a further analysis of experimental results is hindered by the absence of the proper theoretical model at the moment.

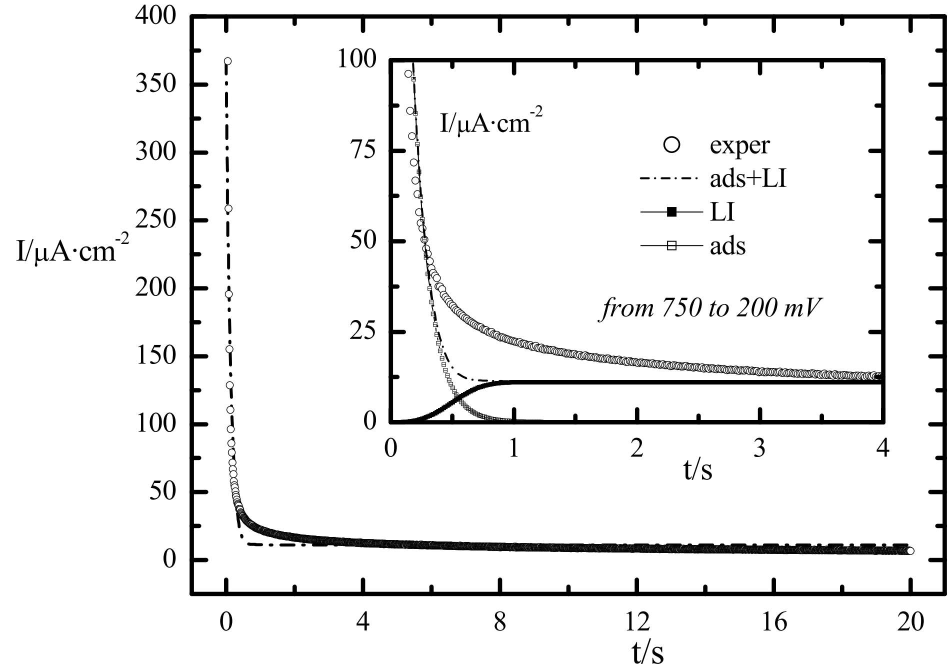

Fig. 5.4a Comparison between experimental and theoretical transients for zinc UPD, with a potential step from 750 to 200 mV. The theoretical model is a sum of two process – adsorption and lattice incorporation, Eq. 5.5a. In the inset experimental and theoretical curves, with different contributions, for the short time range are shown.

With regard to the shape, the current transient curve which is the result of the potential step from 750 to -400 mV, see Fig. 4.3b, exhibits a different deposition mechanism than considered above. In other words, the second term in Eq. 5.6 (related to the hemispherical diffusion) has to be replaced. A pronounce increase of the current after a drop at the initial times is typical for the 3D growth with the lattice incorporation rate determining step [Southampton 1990]. The mathematical description of such a situation for the instantaneous growth can be given as [Armstrong 1966]:

$$I^{inst}_{3D-LI} = nFk^{\uparrow}_{3D}\left\{1-\exp\left(-\frac{\pi M^2 N_0 (k^{\rightarrow}_{3D})^2 t^2}{\rho^2}\right)\right\}. \tag{5.7}$$

In the frame of this model, the shape of the growing islands is assumed to be right circular cones. In such a way, the new model should be expressed as following

$$I_{total} = I_{ads} + I^{inst}_{3D-LI}. \tag{5.8}$$

The theoretical fit by Eq. 5.8 with k_{ads}=3 s^{-1}, q_{ads} = 620 µC/cm^2 and $k_{3D}^{\uparrow}$ = 3.8·10^{-9}mol·$cm^{-2}s^{-1}$, $N_0\cdot\left(k_{3D}^{\rightarrow}\right)^2$ =3.8·10^{-4} $mol^2cm^{-6}s^{-2}$ nicely corresponds to the experimental current transients, what is demonstrated in Fig. 5.5.

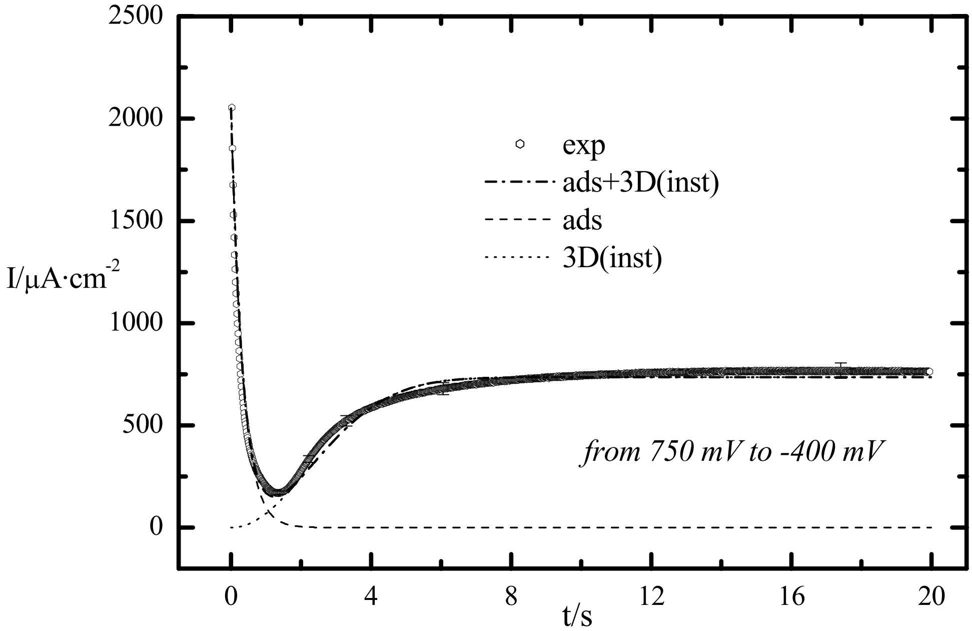

Fig. 5.5 *Comparison between experimental (open diamonds) and theoretical (dash-doted line) curve, the latter one consists of two contributions – adsorption (dashed line) and 3D instantaneous growth (dotted line), see Eq. 5.8.*

The value of k_{ads} follows the trend of the rate constants found during the previous fit, see Tab. 5.1. The adsorption charge q_{ads} is higher in the latter case, what is reasonable for an increase in the amount of the deposited material. As for the two other parameters, they are difficult to analyze. First, they are not available in the literature for the present experimental conditions. Secondly, this type of fit does not allow to separate $k_{3D}^{\rightarrow}$ and N_0.

Summarizing this section, it was shown that the kinetics of zinc deposition can be described by two contributions. The first is attributed to adsorption or/and double layer charging. For the second two models have been tested: hemispherical diffusion and alternatively lattice incorporation under only the latter is consistent with STM observations. This latter model is applied until the aluminum bulk deposition begins. In this case the 3D growth controlled by lattice incorporation becomes significant.

5.4 Spinodal decomposition and 2D phase formation

5.4.1 Spinodal decomposition

From a general point of view, spinodal decomposition is the process through which a thermodynamically unstable system decomposes into two phases. They can be either two phases of the same chemical species (liquid and gas) or phases of different composition (liquid-liquid demixing within a miscibility gap). The spinodal decomposition is different from a nucleation process. In the latter case, for growing of a new phase, thermal fluctuations must overcome some free energy barrier. The creation of a new phase occurs at few randomly distributed nucleation centers. During spinodal decomposition the new phase forms by a continuous process [Cahn 1968]. The initiation of this process can occur at each point of the system [Metiu 1978]. Several seminal works on theoretical understanding of the spinodal decomposition were written by Cahn and Hilliard [Cahn 1958, 1959, 1965]. The theory of spinodal decomposition and phase separation is based on the diffusion equation modified by thermodynamic requirements and all parameters can be measured or estimated by an independent method [Cahn 1968].

Consider a two-component system. The molar free energy, *f(c)*, of such a system at a constant temperature as a function of composition has the following general dependence, see Fig. 5.6.

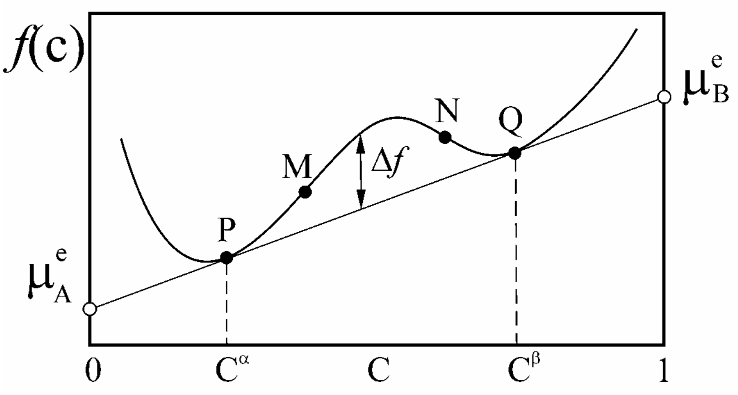

***Regions of phase stability*:**

- P-M and N-Q: *metastable*, $\left(\frac{\partial^2 f}{\partial c^2}\right) > 0$
- M-N: *unstable*, $\left(\frac{\partial^2 f}{\partial c^2}\right) < 0$

Fig. 5.6 *Free energy of a two-component system as a function of composition. Points "P" and "Q" have common tangent, "M" and "N" are inflection points, as a function of temperature they generate the spinodal curve.*

From stability considerations the spinodal decomposition can exist only if on the curve of the free energy there is a region with negative curvature. The common tangent, Fig. 5.6, implies, that the phases of composition c^α and c^β have the same values of chemical potentials and phases α, β are in equilibrium. Any mixture in the region between P and Q will separate into two phases with the compositions c^α and c^β. To bring the system from the metastable to unstable region a finite fluctuation ("nucleus" in Cahn´s theory) is required [Cahn 1965]. At the spinodal the work of forming such nucleus approaches zero [Cahn 1959]. The boundary between instability and metastability regions is defined by the following condition ($\partial^2 f/\partial c^2$)=0 (inflection points M and N in Fig. 5.6).

For understanding of spinodal decomposition, the energy difference ΔF between homogeneous and inhomogeneous solutions is of interest: expanding *f(c)* of the homogeneous solution to second order, we get:

$$\Delta f = \int \left[\frac{1}{2} \left(\frac{\partial^2 f}{\partial c^2} \right) (c - c_0)^2 + k(\nabla c)^2 \right] dV , \qquad (5.9)$$

where V is the volume of the homogeneous solution with composition c, c_0 is the average composition and $k(\nabla c)^2$ is an additional contribution to the free energy due to a compositional gradient [Cahn 1965].

One of the interesting predictions of the Cahn and Hilliard theory is that the resulting picture, in Fig. 5.7 the cross section of corresponding singularities is shown, appearing during the initial stage of the decomposition process will be connective structures dispersed with some equal distance, λ, or fluctuations of density with a wave number, β_m, Eq. 5.10.

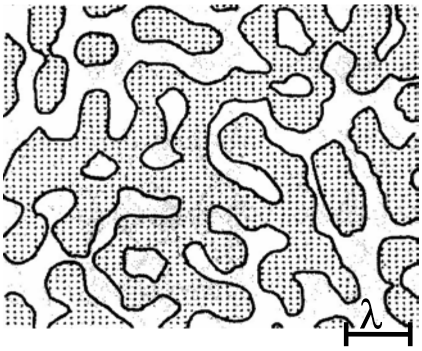

$$\beta_m = \frac{1}{2} \left(-\frac{\partial^2 f}{\partial c^2} \cdot \frac{1}{k} \right)^{1/2} \qquad (5.10)$$

***Fig. 5.7** Cross section view of two-phase morphology during decomposition according to Cahn and Hilliard calculations [Cahn 1971]. The obtained structure has high degree of connectivity with a wave length $\lambda = 2\pi/\beta_m$.*

The value of the wavelength λ depends only on the bulk thermodynamic properties of the system. The cross section shown in Fig. 5.7 is usually called the *labyrinth* or *wormlike* structure and, as it was pointed out by Cahn, is a strong indication that a spinodal mechanism is involved [Cahn 1965].

5.4.2 2D phase formation of zinc

The STM study of this work of the electrochemical phase formation of zinc on gold from the room temperature molten salt has shown that for the underpotential deposition the formation of the wormlike structure is involved (Chapter 4.3). Several independent measurements have been performed to investigate this process in detail. At the beginning the gold substrate was always held for some minutes at 750 mV. Then the potential was at once changed to 200 mV. The surface structure formation was monitored by *in-situ* STM and its development was followed as a function of time. In Fig. 5.8a and b the typical results of such experiments are shown.

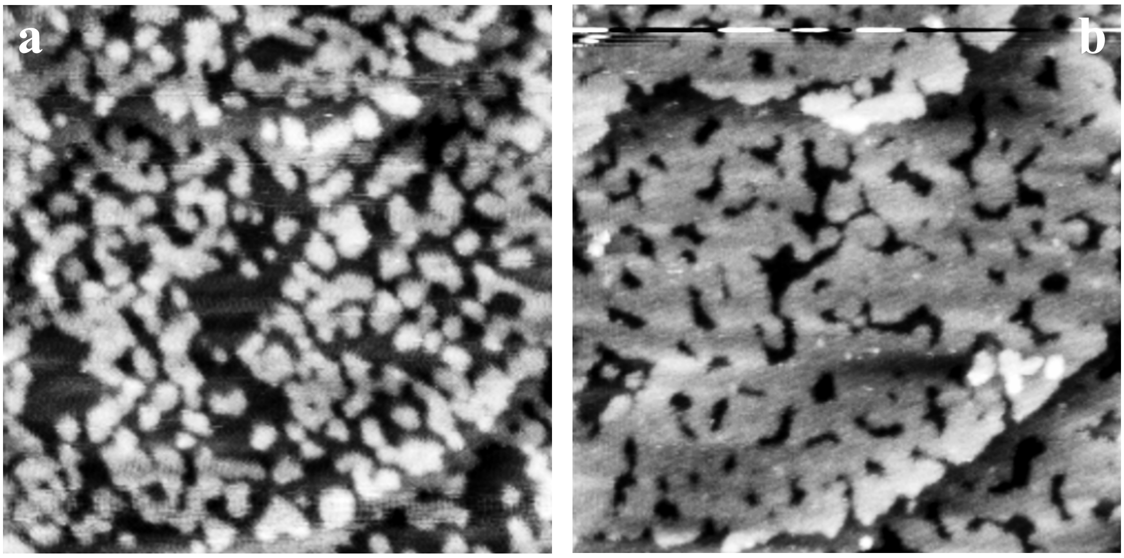

Fig. 5.8 *Electrochemical formation of wormlike structures during deposition* ***a)*** *8 min. and* ***b)*** *81 min. after the potential was changed from 750 to 200 mV, image size is 50×50 nm.*

Similar measurements on the deposition have been performed for several different final potentials – 180, 160, 110, 90 and 80 mV. During the dissolution the surface structure has the similar characteristic morphology. This is demonstrated in more detail in Section 4.3.3, where an example of dissolution of several zinc layers in Fig. 5.9a-b is shown and development of the labyrinth morphology can be followed during the first several minutes.

The close resemblance of the surface morphology observed during Zn phase formation with the structures predicted by the Cahn and Hilliard theory can be immediately seen comparing Fig. 5.7 with 5.8 and 5.9.

To analyze the obtained structure quantitatively, the STM images were treated with the help of a program to determine the *power spectral density* (PSD). The power spectrum analysis, which is offered in DI Nanoscope 4.23 off-line software, is very helpful in characterizing the surface structure, if some periodicity seems to be present. The power spectral density provides a graphical representation of the dominant Fourier components of the surface structure. In principle, the PSD can be understood as standard deviation of the squared surface roughness.

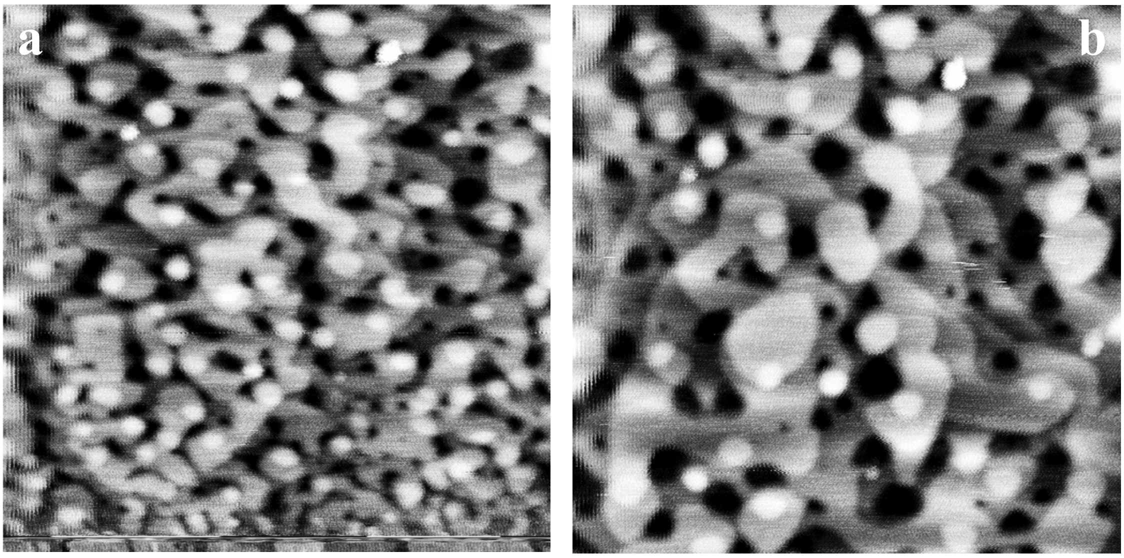

Fig. 5.9 *Electrochemical formation of wormlike structures during dissolution of zinc.* ***a)*** *First 3 min and* ***b)*** *6 min. after the potential was changed from -50 mV to 750 mV, image size is 129×129 nm (detailed description of this experiment is given in Section 4.3.3).*

Mathematically it can be approximated as wave number distribution, q, for a digitized profile of a length L [DI 4.20]:

$$PSD(q) = \frac{d_0}{N} \sum_{j=1}^{N} \left| z_j e^{\frac{-i2\pi(j-1)d_0}{Nd_0}} \right|^2 . \tag{5.11}$$

L consists of N points, which are sampled at intervals d_0 and q ranges from $\frac{1}{L}$ to $\frac{N/2}{L}$.

Analyzing the STM image with the help of the power spectral density it is necessary to remember, that the resulting graph will contain all features of the surface [DI 4.20]. This means, not only just the structure of immediate interest will be evaluated, but all others as well (such as a noise, for example).

For quantitative analysis of the wormlike structure, the only part of the surface, which did not contain features like steps of the Au(111) substrate, was selected. The selection was performed so, that the final surface morphology consisted only of two components – the “worms” and the vacancies between them. For simplicity only images corresponding to the potential step from 750 to 200 mV at two temperatures will be discussed in the following. Similar results have been obtained for other potentials. The evaluation of a spectrum was performed from several STM images, which reveal the development of the labyrinth structure as a function of time. For consistency with model calculations of spinodal decomposition, which will be introduce later in this chapter, the power spectral density in each particular case should be normalized to the area of surface (of STM image) used for the analysis. This was done by multiplying the PSD by $S = A/d^4$, where A is the surface area and d is the diameter of zinc atoms (2.74 Å). The resulting $S_q = \mathrm{PSD}\cdot S$ is dimensionless and has the meaning of a structure factor. The experimentally obtained S_q as a function of wave length, $\lambda = 2\pi/q$, is shown in Fig. 5.10. For the reader's convenience the values of the wave length in Fig. 5.10 are shown on the logarithmic scale.

The main observations of the results in Fig. 5.10 can be summarized as follows. At zero time no structure is visible as is expected for the pure gold surface. At the same time this demonstrates the consistency of the PSD evaluation. Starting with the room temperature structure factors, a binodal distribution with characteristic wavelength at ~3 and 5 nm is indicated. At longer times the structure at 5 nm seems to prevail. At about 30 min this structure is clearly reduced corresponding to an almost complete monolayer with a low concentration of wormlike defects, see e.g. Fig. 5.8b. At the elevated temperature of 50 °C a similar pattern is observed, however, the kinetics is faster and the width of the structure factor is clearly smaller. The structure near 3 nm is only weakly indicated.

5.4.3 Experimental observations of spinodal decomposition in some other systems

So far only a few examples of surface or interface spinodal decomposition studies have been reported in literature. Therefore, it is relevant to give a small literature review. Difference and similarities with the present work will be emphasized.

Evidence of spinodal decomposition for two-dimensional nanocrystal self-assembly by Ge and Brus [Ge 2000] was observed. By means of AFM, nanocrystal aggregation pattern and 2D kinetics on HOPG was studied. After drying the thin nanocrystal solution different results, depending on coverage, on the film surface structure were obtained. The drying process acted as a quench of reduced temperature, thus the system was forced to proceed into unstable spinodal region below the critical temperature. For coverage of particles of 20-30 %, very regular and highly interconnected patterns were observed in this work, while at low coverage, if the process was stopped at very early times, the images revealed randomly distributed nuclei only. These results were treated as the fluid-fluid spinodal phase separation on its different stages. The AFM images of the labyrinth structure revealed that the wave length should be of the order of several tens of angstroms.

The spinodal decomposition morphology is normally difficult to observe in the case of metal deposition. Nevertheless, some representative works can be found in literature.

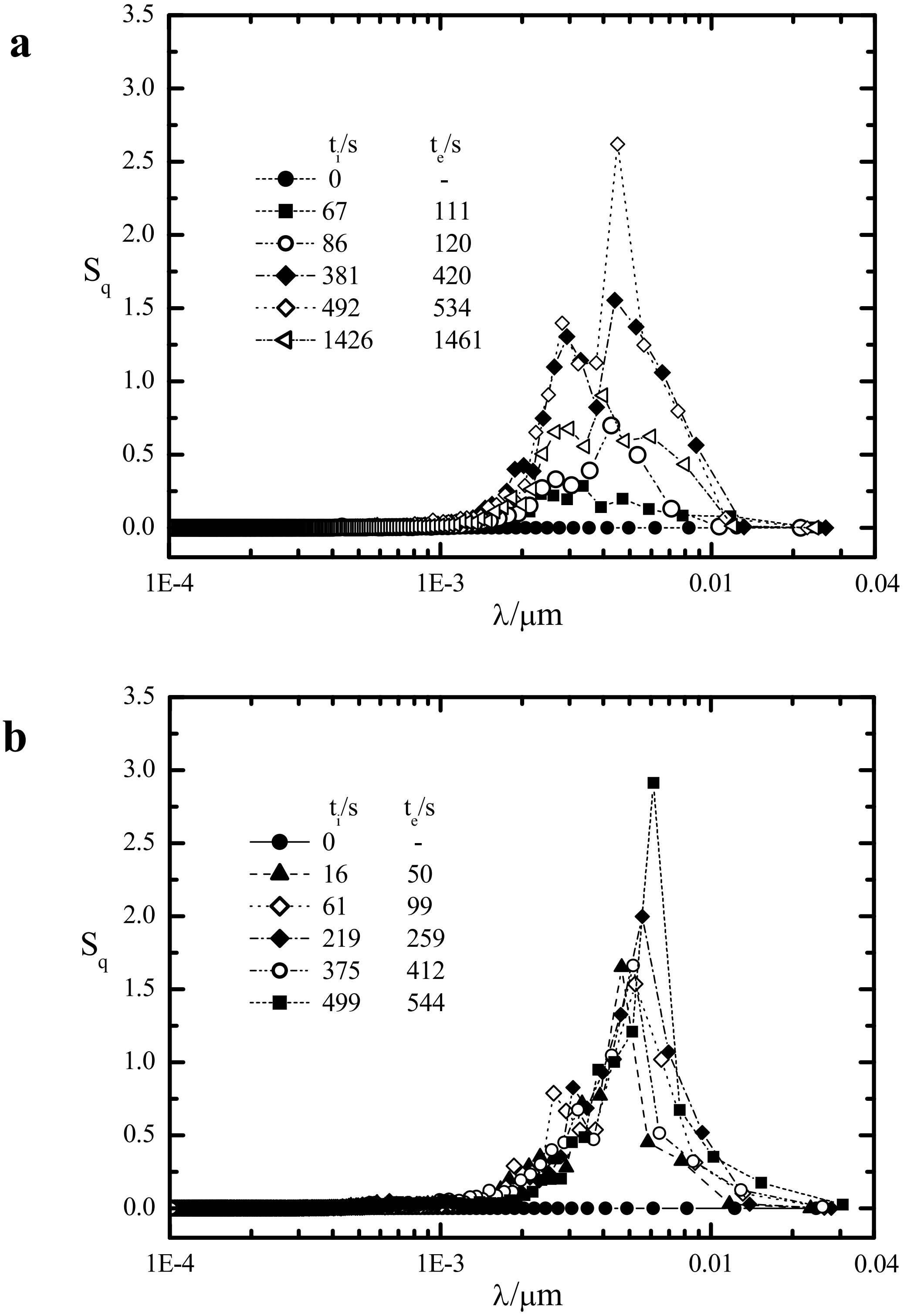

Fig. 5.10 *Time evolution of structure factor S_q vs. wave length λ; S_q, has been determined from STM image sections, showing coherent wormlike structures of 2D Zn deposition recorded at 200 mV and at* ***a)*** *room temperature and* ***b)*** *50 °C. The STM image sections were scanned in the time intervals $t_i \leq t \leq t_e$ after pulsing the potential from 750 to 200 mV.*

The formation of a labyrinth structure was detected, for example, during homoepitaxial growth of Ag under UHV conditions [Pai 2001], [Cadilhe 2000]. The obtained surface morphology was explained in terms of nucleation and growth, where periphery diffusion plays the crucial role. Interesting moment is, that in both cases the labyrinth structure of vacancies was observed only when surface coverage had exceeded a certain value. The typical wavelength of the surface structure could be estimated to lie in the range of 25-30 nm.

The observation of the spinodal decomposition in two-dimensions was presented also by Ernst et al. [Ernst 1992]. The deposition of Cu on Cu(100) was done at low temperatures and the corresponding surface morphology was inferred from the helium atom beam scattering results. Unfortunately the real space of surface structure was not possible to resolve in this experimental work.

Several reports can be found in the literature on the spinodal decomposition in alloys. Wei and coworkers studied the decomposition in Cu-Ti alloy by means of TEM and the wavelength of 5.7 nm was reported [Wei 1997].

An *in-situ* STM study of the spinodal decomposition of the Au adatom gas on the Au surface was performed by Schuster et al. [Schuster 2003]. In their work an electrochemical dissolution of gold in 2M KCl solution was used to induce phase separation. This was performed by applying a microsecond voltage pulse to the STM tip. In such a way the gold atoms were dissolved from the uppermost surface layer. Subsequent evolution of the surface morphology was monitored by STM. The experiment was performed with several time intervals of the voltage pulse and in this way different regimes of a surface coverage were obtained. By analyzing the STM images with the help of a linewise density autocorrelation function, Schuster and coworkers were able to estimate the typical wavelength of the wormlike structure. For a broad coverage range, which was possible to induce in their work, the length was about 4 nm [Schuster 2003].

During the electrochemical phase formation, the structure typical for spinodal decomposition was observed in the work of Endres and Schrodt [Endres 2000]. In this investigation *in-situ* STM study of Ge electrodeposition on Au(111) in a molten salt was performed. During the deposition a wormlike structure with “typical island diameter“ of 2 nm was detected. Although, the authors did not discuss the obtained structure in detail, it is rather probable, that the spinodal mechanism is responsible for the appearance of such a characteristic surface morphology.

5.4.4 Theoretical model for Zn 2D phase formation

The underpotential deposition of Zn and/or Zn-Au alloying as it was demonstrated in Chapter 4.3, involves the formation of wormlike structure, which strongly indicates, that spinodal decomposition is present. As it was already mentioned above the experiment similar to the one conducted in this work was performed by Schuster et al. [Schuster 2003]. In the course of their work a model of the spinodal decomposition was offered, which is very close to the Cahn and Hilliard considerations [Cahn 1958, 1959, 1965]. In spite of the similarity between the work of Schuster et al. for Au dissolution and present work on zinc phase formation, the Cahn-Hilliard model can not be applied directly for 2D phase formation of Zn. The main difference is that there is a constant adsorption of Zn onto the substrate. This can be clearly seen in Fig. 5.11, where the plot of coverage *vs.* time, which was evaluated from the STM images, is shown.

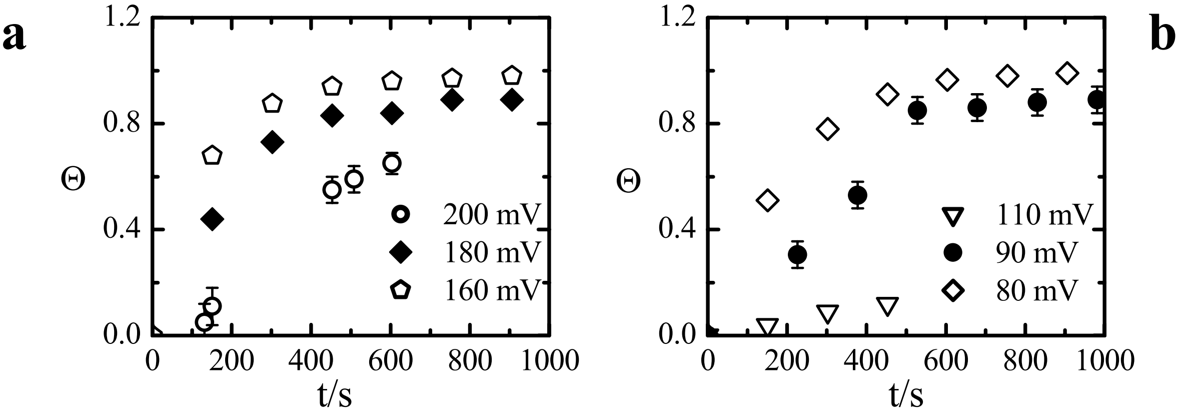

Fig. 5.11 *Dependence on time of surface coverage Θ during Zn deposition in the potential ranges for **a)** first and **b)** second monolayer formation. The data points were obtained by evaluation of the corresponding STM images. For convenience the representative error bars are shown only for one experimental set for each monolayer growth.*

As it can be easily noticed there is always a flow of adsorbed species to the gold surface. Only after ~ 400 s in the case of the first monolayer (≤ 180 mV) and ~ 500 s for the second monolayer (≤ 90 mV), the coverage reaches a constant value and stays almost unchanged, Fig. 5.11a and b respectively. At the same time, for the deposition process at 200 mV it seems to take longer until Θ becomes constant, Fig. 5.11a, also at 110 mV in Fig. 5.11b. A similar behaviour is found for the measurements at 50 °C, which were performed at the potential of 200 mV (Chapter 4.4). These experimental observations will be discussed later in comparison with the theoretical model calculations.

Such an additional adsorption of metal onto the surface was not stimulated in the work of Schuster et al. [Schuster 2003] and hence their model can not be applied here. So, a new approach of spinodal decomposition during electrochemical phase formation must be offered, which would take into account the adsorption process. For this propose the procedure given by Cahn and Hilliard in their work was modified for the case of 2D phase formation and a new model has been developed. The details of this model can be found in [Tsekov 2004]. In the following only a brief description will be given.

The whole system is considered as an incompressible fluid and using the Navier-Stokes equations one can write the following expressions for 2D hydrodynamics of the Zn atoms adsorbed on the gold surface:

$$\partial_t \Gamma + \nabla_r \cdot (\Gamma \mathbf{v}_r) = j_z , \qquad \text{(a)}$$

$$\Gamma \nabla_r \mu_s = \nabla_r \cdot (\eta_s \nabla_r \mathbf{v}_r) + \nabla_r (\zeta_s \nabla_r \cdot \mathbf{v}_r) + \eta(\partial_z \mathbf{v}_r + \nabla_r v_z) - \beta_s \Gamma \mathbf{v}_r , \qquad \text{(b)} \qquad (5.12)$$

where Γ is the number of Zn atoms per unit area (in analogous with fluid density, ρ, in general case), j_z is the normal flux of Zn atoms from the bulk, μ_s is the chemical potential of Zn in the adsorbed layer, v_r and v_s are the radial and normal components of the hydrodynamic velocity, respectively, η_s and ζ_s are the interfacial shear and dilatational viscosities, η is the shear viscosity of the liquid above the layer, β_s is the friction coefficient of the Zn atoms. The equation 5.12b is not equal to zero, and thus the permanent adsorption of zinc is taken into account. The first two terms on the right part of the Eq. 5.12b describe the internal fluid friction between the zinc atoms, the third term takes into account the friction between zinc atoms and the solution and the last term considers a friction between Zn atoms and Au surface.

The solution of the problem is rather difficult and complex. The details are given in [Tsekov 2004]. The basic aspects of the solution were connected with the linearization of the system of Eq. 5.12. Besides that, necessary condition was to couple together momentum transport on the surface and relevant processes in the bulk liquid, including the zinc atoms stationary diffusion in the frames of the linear theory. Last, but not least appropriate boundary conditions were applied to solve the problem. The structure factor predicted on the basis of this theoretical model is given by [Tsekov 2004]:

$$S_q(q,t) = 2k_B T \int_0^t M_q(t_1) \exp\left(-2\int_{t_1}^t M_q(t_2) Q_q(t_2) dt_2 \right) dt_1 , \qquad (5.13)$$

$$\text{where } M_q = \frac{\overline{\Theta}(1-\overline{\Theta})D_s q^2}{k_B T(1-\overline{\Theta}+aq^2)} \tag{5.14}$$

$$\text{and } Q_q = k_B T / \overline{\Theta}(1-\overline{\Theta}) - w(1-aq^2/2)\,. \tag{5.15}$$

M_q is the surface mobility (always positive) and Q_q is the susceptibility of the chemical potential on coverage. Both these parameters are time dependent, since they contain average coverage of the surface $\overline{\Theta}$, which is given by

$$\overline{\Theta} = 1 - \exp(-k_a t)\,. \tag{5.16}$$

D_s is the surface diffusion of the zinc atoms, a is the area of one zinc atom, estimated on the basis of simple geometrical considerations as 7.5 Å^2, w is the interaction energy between zinc atoms, k_B and T are Boltzman constant and temperature, respectively. It should be mentioned, that Q_q can change its sign and for large q it is positive, for small q – negative. The first condition corresponds to stable fluctuations or adsorption and the second one to spinodal decomposition of the adsorbed zinc fluid.

In order to compare the experimental results with theoretical predictions three parameters k_a, D_s and w should be found or estimated. The adsorption rate constant k_a can be obtained from the dependence of the surface coverage on the time, which is shown in Fig. 5.12.

These results were received by evaluation of the STM images, recorded after pulsing the potential from 750 to 200 mV at room temperature and at 50 °C. In accordance with Eq. 5.16, the adsorption rate constants are $(1.6\pm0.2)\cdot10^{-3}$ s^{-1} for room temperature and $(2.3\pm0.2)\cdot10^{-3}$ s^{-1} for 50 °C. The respective activation energy, estimated from the Arrhenius plot $k_a(T)$, is about 0.1 eV. The other parameters (D_s and w), required for theoretical model calculations, were chosen in order to represent a good agreement with the experimental observations. The results for the model evaluation of structure factor for two temperatures are shown in Fig. 5.13. The following values were found to give a best fit with the experiment: $k_a = 1.6\cdot10^{-3}$ s^{-1}, $w =$ 0.17 eV, $D_s = 1.1\cdot10^{-21}$ m^2/s at $T = 25$ °C and $k_a = 2.3\cdot10^{-3}$ s^{-1}, $w =$ 0.14 eV, $D_s = 2.8\cdot10^{-21}$ m^2/s at $T = 50$ °C. As it can be seen, in both cases a good fit of the experimental spectral density is obtained, Fig. 5.10. The structure factor exhibits a maximum, which reveals the spinodal decomposition on the surface. Also, as in the experimental observations, S_q first grows and then decreases with time, compare Fig. 5.10 with 5.13. This is due to the fact that $\overline{\Theta}$ is time dependent, Eq. 5.16, and hence after a maximum the susceptibility changes its sign from negative to positive values and the structure factor decreases.

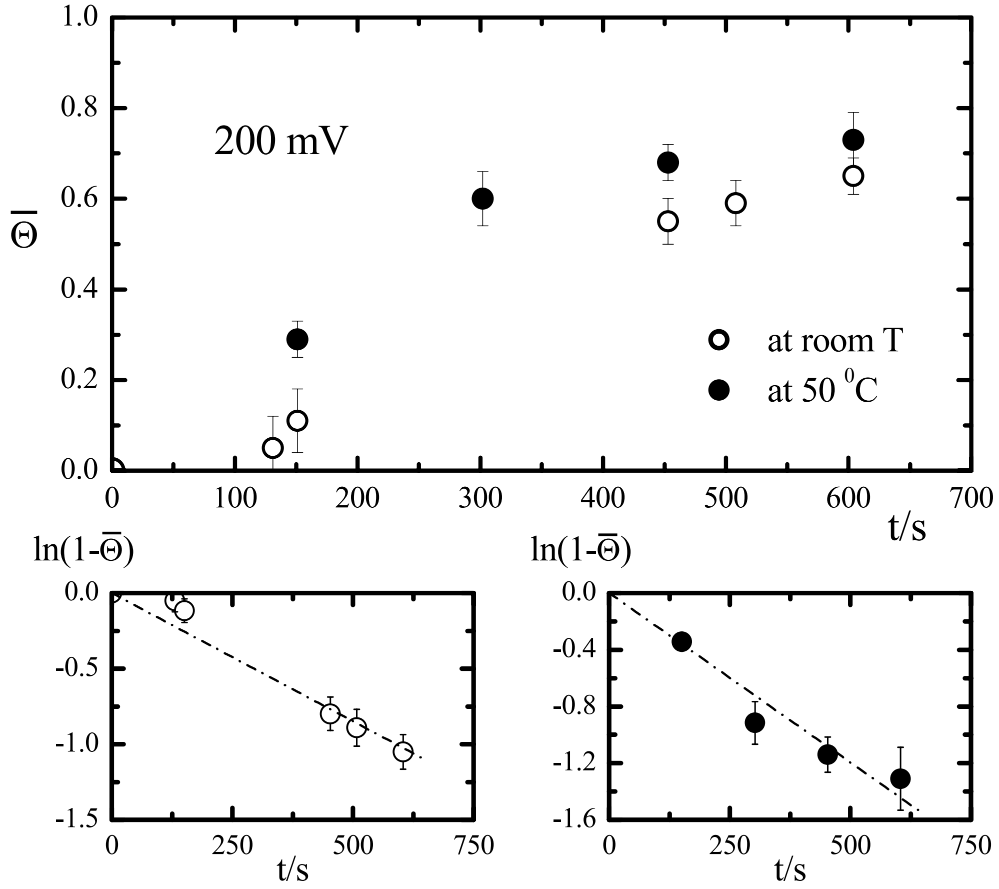

Fig. 5.12 *Upper part: Dependence of the zinc coverage on time at 200 mV for different temperatures. Bottom: a plot of ln(1-Θ) vs. time, from which adsorption rate constants are estimated; left refers to the room temperature measurements and right to 50 °C.*

With increasing the temperature the structure formation accelerates, as it can be see in Fig. 5.13b.Unfortunately, we could not find from the literature data the surface diffusion coefficient of zinc on gold in order to compare it with that one obtained from the fit. A quantitative comparison with the diffusion coefficient of other metals is rather difficult. First, because most of the studies on surface diffusion were done under vacuum conditions. For example, from the work of Pai et al. it follows that the diffusion coefficients for Cu and Ag lie in the range of $(3\div6)\cdot10^{-21}$ m^2/s [Pai 1997]. A good review of D_s of different metals is given in [Barth 2000]. It can be noticed, that the surface diffusion coefficient varies from 10^{-15} to 10^{-23} m^2/s depending on the metal system.

However, diffusion of metals on the electrolyte/substrate interface can be different in comparison with that on vacuum/substrate interfaces. Several investigations performed in aqueous solutions can be found. An evaluation of surface diffusion coefficients of Au and Pt at different electrochemical interface was performed by Alonso et al. [Alonso 1990].

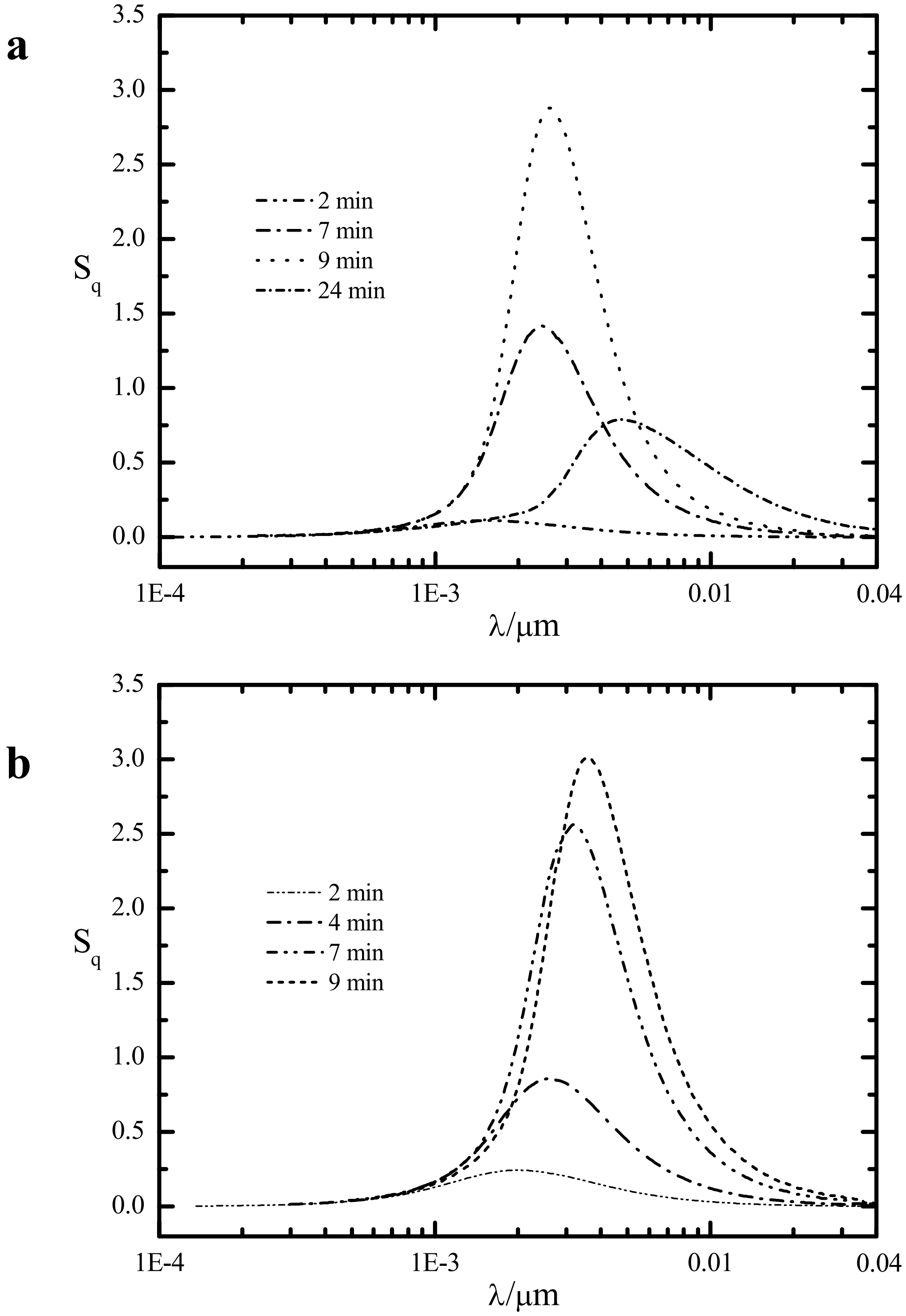

Fig. 5.13 *The power spectral density obtained from the theoretical model of spinodal decomposition during zinc phase formation, see text.* ***a)*** $T = 25$ *°C and* $k_a = 1.6\cdot10^{-3}\ s^{-1}$, $w = 0.17\ eV$, $D_s = 1.1\cdot10^{-21}\ m^2/s$. ***b)*** $T = 50$ *°C and* $k_a = 2.3\cdot10^{-3}\ s^{-1}$, $w = 0.14\ eV$, $D_s = 2.8\cdot10^{-21}\ m^2/s$.

They reported that in contact with electrolytes diffusion of surface atoms becomes higher than in vacuum. At the same time the surface diffusion coefficients for Au and Pt from this work differ from each other relative strongly – $\sim 3\cdot 10^{-17}$ and $\sim 9\cdot 10^{-21}$ m^2/s, respectively. Hence, even in the same solution but for two different metals, the order of magnitude for D_s changes significantly and can not be determined readily. With modification of a solution (by addition of some components, for example) the diffusion coefficient will vary, as it was shown by Vara and coworkers [Vara 1990]. Besides that, considering a molten salt one can imagine that the diffusion will be reduced in comparison with aqueous solutions due to the higher viscosity in former case.

The second main problem with the estimation of the zinc diffusion coefficient on gold is, as it was demonstrated by in-situ STM measurements of this work, that these two metals form surface alloying. The theoretical calculations would require including some additional parameters, which should take into account this effect and thus the calculations would become even more complex.

The increase of the diffusion constant with increasing the temperature, obtained from the theoretical model of this work, corresponds to activation energy of ~0.31 eV, which seems to be quite reasonable.

Concerning the decrease of macroscopic interaction energy w, this could be an indication either of some structure changes or relatively high microscopic interaction potential energy between zinc atoms. The last is more plausible, since considering a hexagonal structure of zinc the binding energy per bond will be approximately $0.2 \div 0.3$ eV, which is order of magnitude higher than k_BT. This is in a good agreement with the value for two dimensional Zn clusters [Wang 2003].

Manufacturer list

⟨Advanced Ceramics⟩	**Advanced Ceramics Research, Inc.** 3292 E. Hemisphere Loop, Tucson, Arizona 85706, www.acrtucson.com
⟨Advent⟩	**Advent Research Materials Ltd.** Eynsham Oxford, England OX29 4JA, www.advent-rm.com
⟨Alfa⟩	**Alfa Johnson Matthey Company** Postfach 110765, D-76057 Karlsruhe, www.alfa.com
⟨Alwin Hoefert⟩	**Alwin Höfert** Ferdinand-Harten-Strasse 15, 22949 Ammersbek, www.hoefert.de
⟨Arrandee⟩	**Arrandee™** Schlossstrasse 94, D-33824 Werther, Germany, www.arrandee.com
⟨Bank⟩	**Bank Elektronik-Intelligent Controls GmbH** Freiberger Strasse 1, D-38678 Clausthal-Zellerfeld, www.bank-ic.de
⟨BASF⟩	**BASF AG** Carl-Bosch-Straße 38, 67056 Ludwigshafen, www.basf.de
⟨DI⟩	**Veeco Instruments GmbH** Janderstrasse 9, D-68199 Mannheim, www.veeco-europe.com
⟨Eurotherm⟩	**Eurotherm Regler GmbH (Controls)** Ottostrasse 1, D-65549, Limburg, www.eurotherm-deutschland.de
⟨Fluka⟩	**Sigma-Aldrich Chemie GmbH** Munich, Germany, www.sigmaaldrich.com
⟨Frank-Magnete⟩	**Frank Magnete GmbH** Rethelstrasse 123, 40237 Düsseldorf
⟨Hilgenberg⟩	**Company Hilgenberg GmbH** D-34323 Malsfeld, www.hilgenberg-gmbh.de
⟨IDE⟩	**Integrated Dynamics Engineering GmbH** Karl-Liebknechtstrasse, D-65479, Raunheim
⟨Merck⟩	**Merck KGaA** Frankfurter Str. 250, D-64293 Darmstadt, Germany, www.merck.de
⟨MEWASA⟩	**MEWASA AG** CH-8887 Mels, Switzerland, www.mewasa.ch
⟨New Focus Inc.⟩	**New Focus Inc**. St. Clara, Californien, USA, www.newfocus.com
⟨Oriental Motors⟩	**Oriental Motor (Europa) GmbH** Schiess-Strasse 74, 40549 Dusseldorf, www.orientalmotor.com
⟨PI Ceramic⟩	**PI Ceramic GmbH** Lindenstrasse, D-07589 Lederhose, www.piceramic.de

References

[Adamson 1990] A. W. Adamson, *Physical Chemistry of Surfaces*, 5th Ed., Willey (1990), see p. 385

[Alonso 1990] C. Alonso, R.C. Salvarezza, J. M. Vara, A. J. Arvia, L. Vazquez, A. Bartolome, A. M. Baro, *J. Electrochem. Soc.*, **137(7)**, 2161 (1990)

[Aramata 1992] A. Aramata, Md. A. Quaiyyum, W. A. Balais, T. Atoguchi, M. Enyo, *J. Electroanal. Chem*, **338**, 367 (1992)

[Aramata 1994] S. Moniwa and A. Aramata, *J. Electroanal. Chem*, **376**, 203 (1994)

[Aramata 1996] A. Aramata, S. Terui, S. Taguchi, T. Kawaguchi, K. Shimazu, *Electrochem. Acta*, **41(5)**, 761 (1996)

[Aramata 1998] A. Aramata, S. Taguchi, T. Fukuda, M. Nakamura, G. Horányi, *Electrochim. Acta*, **44**, 999 (1998)

[Armstrong 1966] R. D. Armstrong, M. Fleischmann, H. R. Thirsk, *J. Electroanal. Chem.*, **119**, 187 (1966)

[Avrami 1940] M. Avrami, *J. Chem. Phys.*, **8**, 212 (1940)

[Atkins 2000] P. W. Atkins, *Physical Chemistry*, 6th edition, Oxford University Press (2000)

[Bai 1992] C. Bai, *Scanning Tunneling Microscopy and its Application*, Springer-Verlag, Berlin Heidelberg (1995)

[Bard 1986] H.-Y. Liu, F.-R. F. Fan, C. W. Lin and A. J. Bard, *J. Am. Chem. Soc.*, **108**, 3838 (1986)

[Bard 2001] A. J. Bard and L. F. Faulkner *"Electrochemical Methods"*, 2001

[Bardeen 1961] J. Bardeen, *Phys. Rev. Lett. B*, **6(2)**, 57 (1961)

[Barradas 1985] R. G. Barradas, E. Bosco, *J. Electroanal. Chem.*, **193**, 23 (1985)

[Barth 2000] J. V. Barth, H. Brune, B. Fischer, J. Weckesser, K. Kern, *Phys. Rev. Lett.*, **84(8)**, 1732 (2000)

[Batina 1992] N. Batina, T. Will, D. M. Kolb, *Faraday Discuss. Chem. Soc.*, **94**, 93 (1992)

[Binnig 1982] G. Binnig, H. Rohrer, C. Gerber, E. Weibel, *Phys. Rev. Lett.*, **49**, 57 (1982)

[Binnig 1983] G. Binnig, H. Rohrer, C. Gerber, E. Weibel, *Phys. Rev. Lett.*, **50**, 120 (1983)

[Boer 1988] F. R. de Boer, R. Boom, W. C. M. Mattens, A. R. Miedema, A. K. Niessen, *Cohesion in Metals: Transition Metal Alloys.*, Amsterdam (1988)

[Bonnell 2001] D. Bonnell, *Basic Principles of Scanning Tunneling Microscopy, in: Scanning Probe Microscopy and Spectroscopy, Theory, Techniques, and Applications* , Wiley-VCH, 2nd ed. D. Bonnell (2001) p. 7

[Bort 1983] H. Bort, K. Jüttner, W. J. Lorenz, G. Staikov, *Electrochimica Acta*, **28(7),** 993 (1983)

[Bosco 1982] E. Bosco and S. K. Rangarajan, *J. Electroanal. Chem.*, **134**, 213 (1982)

[Budevski 1996] E. Budevski, G. Staikov, W. J. Lorenz, *Electrochemical Phase Formation and Growth, An Introduction to the Initial Stages of Metal Deposition*, VCH, Weinheim (1996)

[Budevski 2000] E. Budevski, G. Staikov, W. J. Lorenz, *Electrochim. Acta*, **45**, 2559 (2000)

[Cadilhe 2000] A. M. Cadilhe, C. R. Stoldt, C. J. Jenks, P. A. Thiel and J. W. Evans, *Phys. Rev. B*, **61(7)**, 4910 (2000)

[Cahn 1958] John W. Cahn and John E. Hilliard, *J. Chem. Phys.*, **28(2)**, 258 (1958)

[Cahn 1959] John W. Cahn and John E. Hilliard, *J. Chem. Phys.*, **31(3)**, 688 (1959)

[Cahn 1965] John W. Cahn, *J. Chem. Phys.*, **42(1)**, 93 (1965)

[Cahn 1968] John W. Cahn, *Transactions of the metallurgical society of AIME*, **242**, 166 (1968)

[Cahn 1971] John W. Cahn, *Metastability, instability and the dynamics of unmixing in binary sritical systems,* in *Crit. Phenomena Alloys, Magnets, Supercond., Battelle Inst. Mater. Sci. Colloq.*, 5th, 41-65 (1971)

[Carlin 1994] R. T. Carlin and J. S. Wilkers, *Chemistry and Specification in Room-Temperature Chloroaluminate Molten Salts, in:*

Chemistry of Nonaqueous Solutions, ed. by G. Mamontov and A. I. Popov, VCH, p. 277 (1994)

[Chan 1992] C. T. Chan, K. P. Bohnen, K. M. Ho, *Phys. Rev. Lett.*, **69(11)**, 1672 (1992)

[Chen 1999] P.-Y. Chen, Y.-F. Lin, I-W. Sun, *J. Electrochem. Soc.*, **146(9)**, 3290 (1999)

[Chen 2000] P.-Y. Chen, M.-C. Lin, I-W. Sun, *J. Electrochem. Soc.*, **147(9)**, 3350 (2000)

[Chen 2001] P.-Y. Chen and M.-C. Lin, *Electrochim. Acta*, **46**, 1169 (2001)

[Christensen 1997] A. Christensen, A. V. Ruban, P. Stoltze, K. W. Jacobsen, H. L. Skriver, J. K. Nørskov, F. Besenbacher, *Phys. Rev. B*, **56(10)**, 5822 (1997)

[Chu 1981] M. G. Chu, J. McBreen, G. Adzic, *J. Electrochem. Soc.*, **128(11)**, 2281 (1981)

[Corbel 1999] S. Corbel. J. Cerdá, P. Sautet, *Phys. Rev. B*, **60(3)**, 1989 (1999)

[CRC 1991] *CRC Handbook of Chemistry and Physics*, ed. D. R. Lide, CRC Press, Boca Raton (1991)

[Dent 1990] A. J. Dent, K. R. Seddon, T. Welton, *J. Chem. Soc., Chem. Commun.*, **4**, 315 (1990)

[Despic 1982] A. R. Despic and M. G. Pavlovic, *Electrochem. Acta*, **27(11)**, 1539 (1982)

[DI 4.20] *Nanoscope, Command Reference Manual,* Digital Instruments, Inc., Version 4.20 (1996)

[Drakova 2001] D. Drakova, *Rep. Prog. Phys*. **64**, 205-290 (2001)

[Endres 2000] F. Endres and C. Schrodt, *Phys. Chem. Chem. Phys.*, **2**, 5517 (2000)

[Ernst 1992] H.-J- Ernst, F. Fabre, J. Lapujoulade, *Phys. Rev, Lett.*, **69(3)**, 458 (1992)

[Fannin 1984] A. A. Fannin, Jr., D. A. Floreani, L. A. King, J. S. Landers, B. J. Piersma, D. J. Stech, R. L. Vaughn, J. S. Wilkes and J. L. Williams, *J. Phys. Chem.*, **88**, 2614 (1984)

[Freyland 2001] W. Freyland, in: *Proceedings of NATO Advanced Study Institute on „Molten Salts: From Fundamentals to Applications".* Kas, Turkey, 4.-14. May 2001, ed. Gaune-Escard. Kluwer Academic Publ (2001)

[Freyland 2003] W. Freyland, C. A. Zell, S. Zein El Abedin, F. Endres, *Electrochim. Acta*, **48**, 3053 (2003)

[Garcia 1998] S. Garcia, D. Salinas, C. Mayer, E. Schmidt, G. Staikov, W. J. Lorenz, *Electrochim. Acta,* **43(19-20)**, 3007 (1998)

[Ge 2000] G. Ge and L. Brus, *J. Phys. Chem. B*, **104(41)**, 9573 (2000)

[Halbritter 1995] J. Halbritter, G. Repphun, S. Vinzelberg, G. Staikov and W. J. Lorenz, *Electrochim. Acta*, **40**, 1385 (1995)

[Halbritter 1998] J. Halbritter, *Appl. Phys. A*, **66**, S181 (1998)

[Hamers 2001] R. J. Hamers and D. F. Padowitz, *Methods of Tunneling Spectroscopy with the STM, in: Scanning Probe Microscopy and Spectroscopy, Theory, Techniques, and Applications* , Wiley-VCH, 2nd ed. D. Bonnell (2001) p. 59

[Heben 1988] M. J. Heben, M. M. Dovek, N. S. Lewis, R. M. Penner, C. F. Quate, *Journal of Microscopy*, **152(3)**, 651 (1988)

[Horányi 1997] G. Horányi , A. Aramata, *J. Electroanal. Chem.*, **434**, 201 (1997)

[Horányi 1997a] G. Horányi , A. Aramata, *J. Electroanal. Chem.*, **437**, 259 (1997)

[Hölzle 1994] M. H. Hölzle, U. Retter, D. M. Kolb, *J. Electroanal Chem.*, **371**, 101 (1994)

[Hölzle 1994a] M. H. Hölzle, D. M. Kolb, *J. Electroanal Chem.*, **371**, 101 (1994)

[Hümann 2003] S. Hümann, J. Hommrich, K. Wandelt, *Thin Solid Films*, **428**, 76 (2003)

[Hussey 1991] C. L. Hussey and X. Xu, *J. Electrochem. Soc.*, **138(7)**, 1886 (1991)

[Hussey 1994] C. L. Hussey, *The Electrochemistry of Room-Temperature Haloaluminate Molten Salts, in: Chemistry of Nonaqueous Solutions*, ed. by G. Mamontov and A. I. Popov, VCH, p. 227 (1994)

[Hyde 2003] M. E. Hyde, R. Compton, *J. Electroanal. Chem.*, **549**, 1 (2003)

[Jüttner 1980] K. Jüttner, W. J. Lorenz, *Z. Phys. Chem.N.F.*, **122**, 163 (1980)

[Klitsner 1990] T. Klitsner, R. Becker, J. Vickers, *Phys. Rev. B*, **41(6)**, 3837 (1990)

[Kolb 1978] D. M. Kolb, *Physical and Electrochemical Properties of Metal Monolayers on Metallic Substrate, in: Advances in Electrochemistry and Electrochemical Engineering,* ed. by H. Gerischer and C. W. Tobias, Willey, New York, Vol. 11, (1978),

[Koslowski 2001] The Program created by Th. Koslowski

[Lin 1993] Yu-Po Lin, J. R. Selman, *J. Electrochem. Soc.*, **140(5)**, 1304 (1993)

[Lin 2001] M.-C. Lin, P.-Y. Chen, I-W. Sun, *J. Electrochem. Soc.*, **148(10)**, C653 (2001)

[Lüth 2001] H. Lüth, *Solid Surfaces, Interfaces and Thin Films*, 4th ed., Springer, Heidelberg (2001)

[Massalski 1990] *Binary Alloy Phase Diagrams*, ed. by T. B. Massalski, ASM International, Materials Park, Ohio (1990) Vol. 1, p. 457.

[McBreen 1978] J. McBreen, E. J. Cairns, *The Zinc Electrode, in: Advances in Electrochemistry and Electrochemical Engineering,* ed. by H. Gerischer and C. W. Tobias, Willey, New York, Vol. 11, p. 288, 289 (1978),

[Metiu 1978] Horia Metiu, *J. Chem. Phys.*, **68(4)**, 1538 (1978)

[Moffat 1999] T. P. Moffat, *J. Electroanal. Chem.*, **21**, 211-316 (1999)

[Möller 1997] F. A. Möller, J. Kintrup, A. Lachenwitzer, O. M. Magnussen, R. J. Behm, *Phys. Rev. B*, **56(19)**, 12506 (1997)

[Möller 1999] F. A. Möller, O. M. Magnussen, R. J. Behm, *Z. Phys. Chem.*, **208**, 57 (1999)

[Naohara 1998] Hideo Naohara, Shen Ye, Kohei Uosaki, *J. Phys. Chem. B*, **102**, 4366 (1998)

[Nielsen 1993] L. P. Nielsen, F. Besenbacher, I. Stensgaard, E. Lægsgaard, C. Engdahl, P. Stoltze, K. W. Jacobsen, J. K. Nørskov, *Phys. Rev. Lett.*, **71(5)**, 754 (1993)

[Ohtsuka 1995] T. Ohtsuka, E. Kuwamura, A. Komori, T. Uchida, *ISIJ International*, **35(7)**, 892 (1995)

[Ohtsuka 1998]. T. Ohtsuka, A. Komori, *Electrochimica Acta*, **43**, 3269 (1998)

[Pai 1997] W. W. Pai, A. K. Swan, Z. Zhang, J. F. Wendelken, *Phys. Rev. Lett.*, **79(17)**, 3210 (1997)

[Pai 2001] Woei Wu Pai, John F. Wendelken, C. R. Stoldt, P. A. Thiel, J. W. Evans, Da-Jiang Liu, *Phys. Rev. Lett.*, **86(14)**, 3088 (2001)

[Palomar-Pardavé 1998] M. Palomar-Pardavé, M. Miranda-Hernández, I. González, N. Batina, *Surf. Sci.*, **399**, 80 (1998)

[Palomar-Pardavé 2000] M. Palomar-Pardavé, I. González, N. Batina, *J. Phys. Chem. B*, **104**, 3545 (2000)

[Pangarov 1983] N. Pangarov, *Electrochimica Acta,* **28(6)**, 763 (1983)

[Pitner 1996] W. R. Pitner, C. L. Hussey, G. R. Stafford, *J. Electrochem. Soc.*, **143(1),** 130 (1996)

[Pitner 1997] W. R. Pitner and C. L. Hussey, *J. Electrochem. Soc.*, **144(9),** 3095 (1997)

[Pletcher 1990] D. Pletcher and F. C. Walsh, *Industrial Electrochemistry*, Chapman and Hall, London (1990)

[Randler 1999] R. Randler, M. Dietterle, D. M. Kolb, *Z. Phys. Chem.*, **208**, 43 (1999)

[Repphun 1995] G. Repphun, J. Halbritter, *J. Vac. Sci. Technol. A*, **13(3)**, 1693 (1995)

[Rousset 1992] S. Rousset, S. Chiang, D. E. Fowler and D. D. Chambliss, *Phys. Rev. Lett.*, **69(2)**, 3200 (1992)

[Röder 1993] H. Röder, R. Schuster, H. Brune, K. Kern, *Phys. Rev. Lett.*, **71(13)**, 2086 (1993)

[Scharifker 1983] B. R. Scharifker and G. J. Hills, *Electrochim. Acta*, **28**, 879 (1983)

[Scharifker 1999] B. R. Scharifker, J. Mostany, M. Palomar-Pardavé, I. Gonzàlez, *J. Electrochem. Soc.*, **146(3)**, 1005 (1999)

[Schlößer 2000] D. C. Schlößer, K. Morgenstern, L. K. Verheij, G. Rosenfeld, F. Besenbacher, G. Comsa, *Surf. Sci.,* **465**, 19, (2000)

[Schuster 2003] R. Schuster, D. Thron, M. Binetti, X. Xia, G. Ertl, *Phys. Rev. Lett.*, **91(6)**, 066101 (2003)

[Shkurankov 2002] A. Shkurankov, F. Enders, W. Freyland, *Rev. Sci. Instrum.*,

73(1), 102 (2002)

[Southampton 1990] Southampton Electrochemistry Group, *Instrumental Methods in Electrochemistry*, Ellis Horwood Series in Physical Chemistry (1990)

[Staikov 1998] J. Sackmann, A. Bunk, R. T. Pötzschke, G. Staikov and W. J. Lorenz, *Electrochimica Acta*, **43**, 2863 (1998)

[Taguchi 1995] S. Taguchi, A. Aramata, *J. Electroanal. Chem.*, **396**, 131 (1995)

[Takahashi 2002] S. Takahashi, A. Aramata, M. Nafamura, K. Hasebe, M. Tanaguchi, S. Taguchi, A. Yamagishi, *Surf. Sci.*, **512**, 37 (2002)

[Tersoff 1983] J. Tersoff, D. R. Hamann, *Phys. Rev. Let.*, **50(25)**, 1998 (1983)

[Tersoff 1985] J. Tersoff, D. R. Hamann, *Phys. Rev. B*, **31(2)**, 805 (1985)

[Tersoff 1995] J. Tersoff, *Phys. Rev. Lett.*, **74(3)**, 434 (1995)

[Tersoff 2001] J. Tersoff, *Theory of Scanning Tunneling Microscopy*, *in: Scanning Probe Microscopy and Spectroscopy, Theory, Techniques, and Applications* , Wiley-VCH, 2nd ed. D. Bonnell (2001) p. 43

[Tromp 1992] R. M. Tromp, A. W. Denier van der Gon, M. C. Reuter, *Phys. Rev. Lett.*, **68(15)**, 2313 (1992)

[Tromp 1993] R. M. Tromp, *Phys. Rev. B*, **647(12)**, 7125 (1993)

[Trulove 1992] P. C. Trulove, R. A. Osteryoung, *Inorg. Chem.*, **31**, 3980 (1992)

[Tsekov 2004] *private communication*

[Vara 1990] C. Alonso, R. C. Salvarezza, J. M. Vara and A. J. Arvia, *Electrochimica Acta*, **35(9)**, 1331 (1990)

[Varela 1992] F. E. Varela, L. M. Grassa, J. R. Vilche, *Electrochim. Acta*, **37**, 1119 (1992)

[Venables 2000] J.A. Venables, *Introduction to Surface and Thin Film Processes*, Cambridge University Press, Cambridge (2000)

[Vinzelberg 1997] The Program created by S. Vinzelberg

[Wang 2003] J. Wang, G. Wang, J. Zhao, *Phys. Rev. A*, **68**, 013201-1 (2003)

[Wei 1997] Y. Wei, L. Hu, Y. Huang, X. Wang, *Jinshu Rechuli Xuebao*,

18(2), 9 (1997), abstract in english

[Welland 1990] M. E. Welland and M. E. Taylor, *Scanning Tunneling Microscopy, in: Modern Microscopies, Techniques and Applications*, ed. by P. J. Duke and A. G. Michette, Plenium Press, New York (1990) p. 231

[Welton 1999] T. Welton, *Chem. Rev.*, **99**, 2071 (1999)

[Wen 1994] J.-M. Wen, S.-L. Chang, J. W. Burnett, J. W. Evans and P. A. Thiel, *Phys. Rev. Lett.*, **73(19)**, 2591 (1994)

[Wilkes 1982] J. S. Wilkes, J. A. Levisky, R. A. Wilson, C. L. Hussey, *Inorg. Chem.* **21**, 1263 (1982)

[Will 1993] T. Will, M. Dietterle, D. M. Kolb, in: *Proceedings of NATO Advanced Study Institute of "Nanoscale Probes of the Solid/Liquid Interface"*, Sophia Antipolis, France, 10-20. July 1993, ed. A. A. Gewirth and H. Siegenthalter, Kluwer Academic Publ, p.137 (1995)

[Zawodzinski 1990] T. A. Zawodzinski, R. A. Osteryoung, *Inorg. Chem.*, **26**, 2842 (1990)

[Zell 1999] C. A. Zell, F. Endres and W. Freyland, *Phys. Chem. Chem. Phys.*, **1**, 697 (1999)

[Zell 2001] C. A. Zell, W. Freyland, *Chemical Physics Letters*, **337**, 293 (2001)

[Zell 2002] C. A. Zell, PhD thesis (2002)

Curriculum Vitae

Personal data

Name: Dogel Jana A.
Data and place of birth: 8th April 1977 Troizk, Russia
Marital status: married, no children

Secondary education:

1984-1994 Secondary school, Troizk, Russia

Tertiary education:

1994-1998 *Moscow State Steel and Alloys University*, Moscow, Russia

July 1998 Bachelor, Dep. of Phys. Chem., *Title: "****Methods of calculations of temperature of the beginning of metal oxides reduction****".*

1994-2000

June 2000 Master of Science, Dep. of Phys. Chem., *Title: "****Equilibria in Fe-C-O and Fe-H-O systems****".*

Ph.D. project

Jan. 2001 – Jun. 2004 Member of research group of Prof. Dr. W. Freyland, University Karlsruhe (TH), Department of Condensed Matter, Germany

Acknowledgement

PhD project always comes to fruition only with the assistance of many people. Here I would like to thank all who contributed directly (and indirectly) to the quality of this work:

- Prof. Dr. W. Freyland for the very interesting topic and efficient supervision on all stages of my thesis,
- Prof. Dr. M. Olzmann for the reading of my work as a co-referee,
- Dr. Christine Zell who introduced the *tunneling techniques* to me and always helped with many “tips and tricks” of DI-controller and not only,
- to all people of mechanical workshop of the University, to Herrn D. Waltz and Herrn H. Ernesti in particular, who were very patient to realized all my “tiny” technical ideas, whatever material was, starting from Teflon or µm-gold foil to quartz and even sapphire,
- Herrn K. Jacob from the electrical workshop for cleaning and reanimating the scanner and Herrn C. Heck, especially, for his help with the “thermocouples problem”,
- Herrn G. Rotter for fine manipulations with glass and quartz,
- Herrn J. Szepessy for professional help with any PC troubles, “well-timed” updates and impenetrable protection from any viruses,
- Jens Dubielzig for the careful and patient preparation of the molten salt, etching STM tips in dangerous acids, an unceasing interest to results of the experiments and the constant support with questions like: “Tja, schon die zehnte Messung in einer Reihe ist gescheitert...“,
- all members of the STM-division for the fruitful discussions, what ever a subject was and letting me keep my experimental work in a good form,
- the whole PCI-group for the friendly and communicative atmosphere, above all Priv.-Doz. Dr. Detlef Nattland and Gudrun Ritter, who were always ready to give me a small lecture about right German and local dialect, respectively.

The very special thanks is addressed to my husband Stas for his support, understanding, believe and everything else.